Raman Spectroscopy of GaAs Nanowires: Doping Mechanisms and Fundamental Properties

THÈSE N° 5211 (2011)

PRÉSENTÉE LE 9 DÉCEMBRE 2011
À LA FACULTÉ SCIENCES ET TECHNIQUES DE L'INGÉNIEUR
LABORATOIRE DES MATÉRIAUX SEMICONDUCTEURS
PROGRAMME DOCTORAL EN SCIENCE ET GÉNIE DES MATÉRIAUX

ÉCOLE POLYTECHNIQUE FÉDÉRALE DE LAUSANNE

POUR L'OBTENTION DU GRADE DE DOCTEUR ÈS SCIENCES

PAR

Bernt KETTERER

acceptée sur proposition du jury:

Prof. F. Stellacci, président du jury
Prof. A. Fontcuberta i Morral, directrice de thèse
Prof. A. Kis, rapporteur
Dr H. Riel, rapporteur
Prof. C. Schüller, rapporteur

Abstract

Semiconductor nanowires offer a wide range of opportunities for new generations of nanoscale electronic and optic devices. For these applications to become reality, deeper understanding of the fundamental properties of the nanowires is required. In this thesis, Raman spectroscopy has been applied to examine the characteristics of GaAs nanowires facing the following challenges in current nanowire research: (i) understanding of the doping mechanisms in catalyst-free GaAs nanowires grown by MBE, (ii) examination of the electronic band structure of the wurtzite polytype of GaAs, and (iii) probing the properties of free carrier systems in nanowire based quantum-heterostructures.

The Si-doping of GaAs nanowires was studied in the first part of the thesis. The investigation of the local vibrational modes of the silicon dopants in the GaAs host lattice allowed to identify the incorporation pathways the dopants take during the nanowire growth and to determine the limitations of the doping process due to compensation effects. Important information on the concentration and mobility of the free carriers in the doped material has been obtained by analyzing the coupled longitudinal optical phonon-plasmon modes.

The second part of the thesis focused on the electronic band structure in wurtzite GaAs. Here, resonant Raman scattering from first and second order longitudinal optical phonons was used in oder to determine the band-gap, the position of the light-hole band as well as the temperature dependence of the crystal-field split-off band. As important parameters the spin-orbit coupling and crystal-field splitting have been obtained.

The photoexcited electron-hole plasma and the confined optical phonons in nanowire-based GaAs/AlAs multi-quantum-well structures were studied in the last part of the thesis. Structural parameters could be deduced from the position of the confined phonon modes. The coupling of the plasmon to the phonon gives important information on the system of photogenerated carriers within the quantum structure.

Keywords: GaAs nanowires, resonant Raman spectroscopy, doping mechanisms, dopant compensation, LO-phonon-plasmon coupling, wurtzite GaAs, electronic band structure, nanowire heterostructures, phonon confinement, photoexcited plasma

Zusammenfassung

Halbleiter-Nanodrähte eröffnen ein weites Feld an Möglichkeiten zur Entwicklung neuer Generationen elektronischer und optischer Bauelemente. Die erfolgreiche Umsetzung in neuartige Anwendungen setzt jedoch fundierte Kenntnisse der Eigenschaften dieser Nanostrukturen voraus. Mit Hilfe der Raman-Spektroskopie wurden in dieser Arbeit GaAs Nanodrähte unter folgenden Gesichtspunkten aktueller Forschung untersucht: (i) Erlangen eines tieferen Verständnisses der Dotierungsprozesse beim Nanodraht-Wachstum, (ii) Bestimmung der elektronischen Bandstruktur in der Wurtzit Phase von GaAs und (iii) Erforschung der Eigenschaften freier Ladungsträger in nanodrahtbasierten Heterostrukturen.

Im ersten Teil der Arbeit wurden die grundlegenden Prozesse bei der Silizium-Dotierung von GaAs Nanodrähten untersucht. Basierend auf einer Analyse lokaler Schwingungsmoden der Dotieratome im GaAs Wirtsgitter konnten die Inkorporationspfade der Dotieratome während des Wachstums sowie die durch Kompensationseffekte bedingten Grenzen der Dotierfähigkeit bestimmt werden. Anhand einer Analyse der Plasmon-Phonon Kopplung im dotierten Material wurde die Konzentration und Mobilität der freier Ladungsträger ermittelt.

Schwerpunkt des zweiten Teils der Arbeit war die Untersuchung der elektronischen Bandstruktur von Wurtzit GaAs. Eine Analyse der resonanten Raman-Streuung longitudinal-optischer Phononen erster und zweiter Ordnung erlaubte die Bestimmung der Bandlücke, der Position des leichten Loch Valenzbandes sowie der Temperaturabhängigkeit des durch das Kristallfeld abgespaltenen Split-Off-Valenzbandes. Daraus konnten wichtige Bandparameter wie die Spin-Bahn-Kopplung und die Kristallfeld-Aufspaltung abgeleitet werden.

Die Eigenschaften photogenerierter Ladungsträger und quantisierter optischer Phononen in nanodrahtbasierten GaAs/AlAs Multi-Quantum-Well Strukturen wurden im letzten Teil der Arbeit untersucht. Anhand der Position der quantisierten Gitterschwingungen konnte die Breite der Quantentöpfe bestimmt werden. Wichtige Informationen über die Eigenschaften der freien Ladungsträger in der Quantenstruktur konnten aus einer Analyse der Kopplung quantisierter longitudinal optischer Phononen an das Plasma gewonnen werden.

Schlüsselwörter: GaAs Nanodrähte, resonante Ramanspektroskopie, Dotiermechanismen,

Kompensation, LO-Phonon-Plasmon Kopplung, Wurtzit GaAs, elektronische Bandstruktur, Nanodraht-basierte Heterostrukturen, Phonon-Confinement, photogeneriertes Plasma

Contents

Contents

1 Introduction

A bird's eye view of the content of the thesis is provided in this first chapter. The motive forces behind the work with semiconductor nanowires are the fundamental new physical phenomena emerging on the nanometer scale and the excellent perspectives for nanowires to act as the building blocks of future nanoscale devices. In light of this motivation, the objectives of the thesis are stated against the major challenges in this field of science. Finally, an overview of the individual chapters is given.

1.1   Semicoductor Nanowires - Perspectives and Challenges

In recent years, semiconductor nanowires have stimulated a new enthusiasm in the emerging field of nanotechnology [1, 2, 3, 4, 5]. Nanowires are single-crystalline, filamentary and highly anisotropic crystals with diameters between around 10 and 200 nm that result from rapid growth along one direction. The great interest in these structures is based on manifold reasons. First of all, these one-dimensional semiconductor nanostructures enable extraordinary progress in applications such as functional nanoelectronic devices [1], high mobility field effect transistors [6], single molecule sensing [7], batteries [8], solar cells [9], and thermoelectric devices [10]. Additionally, in fundamental mesoscopic physics they act as a playground for the study of fascinating phenomena in the submicron regime [11, 12].

At the nanometer scale, crystalline particles, tubes and wires exhibit a variety of optical, electrical and mechanical properties that depend explicitly on the specific size, shape and aspect ratio [13, 14, 15]. Understanding these novel properties promises to be able to tune the functionality of materials and manipulate ultimately new nanostructures into complex functional structures and nanodevices. For instance, one of the most unique characteristics of nanowires is their effective strain relaxation at heterojunction interfaces. With the ability to grow for example GaAs nanowires on silicon substrates, radically new pathways are opened for a next generation of computers that integrate phontonic and electronic components on a single platform [16, 17].

In the following, the major challenges in semiconductor nanowire research that are faced in this thesis are briefly discussed.

1.1.1   Nanowire Doping

Gallium arsenide (GaAs) has a long tradition in the history of mesoscopic physics. In retrospect, the immense importance of GaAs as a semiconductor was mainly due to the high level of technical control over the doping in this material. This applies in particular to the practical applications where doping - the intentional incorporation of atomic impurities - is essential in order to manipulate and to design the optical, electrical and magnetic properties of semiconductor materials. The task of growing high purity crystals with well defined doping levels and doping distributions was first achieved by the technique of molecular beam epitaxy (MBE) [18]. However, the doping mechanisms in binary compound semiconductors such as GaAs turned out to be highly complex. For example, silicon acts as an amphoteric dopant that
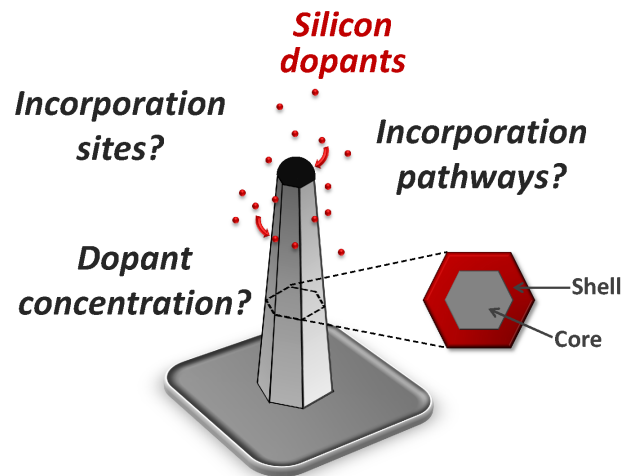
Figure 1.1: Schematics showing the open questions concerning the silicon doping process during the gallium-selfcatalyzed MBE growth of GaAs nanowires.

can occupy substitutional cation (Si_{Ga}) as well as anion sites (Si_{As}), but it can also form simple complexes like nearest-neighbor donor acceptor pairs (Si_{Ga}-Si_{As}), and even clustering and dopant precipitation may occur at the highest doping levels [19].

Due to the importance of doping for the realization of devices, doping of semiconducting nanowires is increasingly attracting scientific interest in the last few years [20]. A technologically important fact is that the incorporation of dopants during the growth of a semiconductor strongly depends on the nature of the growth method. For example, in thin films grown by organometallic vapor-phase epitaxy doping incorporation is dominated by the chemistry and thermodynamics of the doping and growth process, whereas in MBE-grown films dopant incorporation is mainly controlled by kinetics such as impurity arrival rate, reevaporation rate etc. The most generally accepted method for nanowire growth is the vapor-liquid-solid (VLS) process [21, 22]. The essential feature of the concept is forming a catalytic metallic droplet which can rapidly adsorb a vapor to supersaturation levels. Once the vapor phase constituent has been reached beyond the equilibrium concentration crystal growth of one-dimensional nanowires can subsequently occur from nucleated seeds at the liquid-solid interface.

Until now, the processes shown in Fig. 1.1 that rule the dopant incorporation during the growth of nanowires by molecular beam epitaxy via the vapor-liquid-solid method are not understood very well. Elucidating the mechanisms and the limitations of dopant incorporation is therefore a major prerequisite for the achievement of controlled doping and well defined dopant profiles. With regards to the process of doping and doping mechanisms, and depending on the growth

conditions, the following are the currently still unanswered questions:

- Which dopant concentrations can be achieved?

- What is the maximum free carrier concentration obtainable with each dopant?

- Which are the limiting factors for the doping efficiency?

- What is the mobility of electrons or holes in semiconductor nanowires?

- What are the incorporation-pathways that dopants take during the VLS-growth: incorporation from the side facets of the nanowire by direct deposition or incorporation into the core of the nanowire by dissolving the dopants in the catalyst and subsequent transport across the liquid-solid interface?

- What are the incorporation sites the dopant atoms take within the crystalline lattice of GaAs?

1.1.2   Band Gap Engineering in Polytypic Nanowire Devices

Recently, a new degree of freedom in the formation of nanowire heterostructures has appeared. The new type of heterostructure concerns the variation of the crystal phase along the nanowire instead of the material composition. Important semiconductors such as GaAs, GaP, InAs, InP, AlAs, AlP, GaSb, InSb or Si are stable in the zinc-blende structure (ZB). They may crystallize in the wurtzite (WZ) lattice when they are grown in the nanowire form [23, 24]. The change in the crystal symmetry from cubic to hexagonal implies a modification of the electronic band structure as schematically shown in Fig. 1.2.

The coexistence of WZ and ZB phases within a single nanowire opens unprecedented possibilities for band structure engineering and advanced nanowire devices. For example, due to the staggered band alignment between WZ and ZB GaAs, a quantum dot formed by an island of WZ (ZB) in a ZB (WZ) matrix would enable the longtime storage of holes (electrons). Alternatively, the formation of polytypic superlattices in silicon could eventually lead to the transformation in a direct bandgap material [25, 26]. For the design of these novel structures, it is essential to have a clear picture of the band structure of the polytypes. In the group of III-V compounds for example, gallium arsenide with zinc-blende crystal structure ranks among the best understood semiconductors in terms of its electronic structure. In contrary,
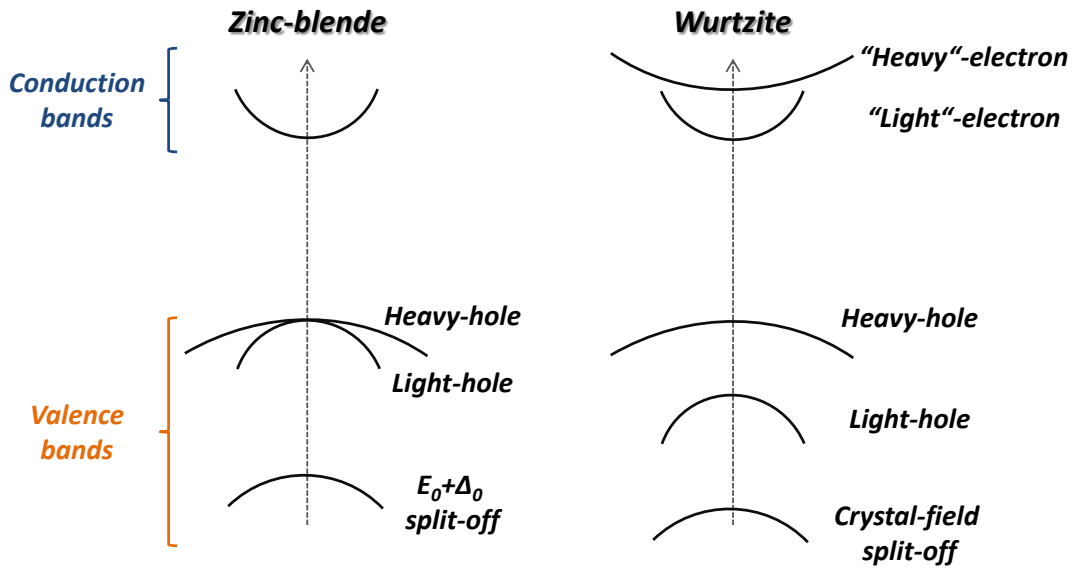
Figure 1.2: Comparison of the electronic band structure of semiconductors with zinc-blende and wurtzite crystal structure.

only little is known about the wurtzite polytype of GaAs, and the band structure of this novel semiconductor material remains unexplored.

1.1.3 Semiconductor Nanowire Heterostructures

In the past, layered semiconductor heterostructures with for example ultra-thin layers of alternating materials and/or doping enabled technological breakthroughs in electronics and optoelectronics. The ability to create a two dimensional electron gas at the heterojunction had a strong impact in science and technology. It allowed the development of high mobility transistors and the detailed study of fundamental physics in low-dimensional correlated electron systems like the integer and fractional quantum hall effect [27]. Nanowire core/shell heterojunctions provide a unique platform to study the electro-optic properties of heterojunction electron gases at nanoscale dimensions. Here, optical spectroscopy is a meaningful probe to investigate these properties in a non-desctructive way (see Fig. 1.3). Compared to layered systems, nanowire heterostructures are much more complex because of the large parameter space that determines the nanowire properties. Not only the bandgaps and band-offsets, the size, the material compostition, the doping influence the electronic properties, but also the cross-sectional geometry of the nanowire emerges as a new parameter. Two-dimensional electron gases wrapped around the nanowire core with circular, triangular, or hexagonal
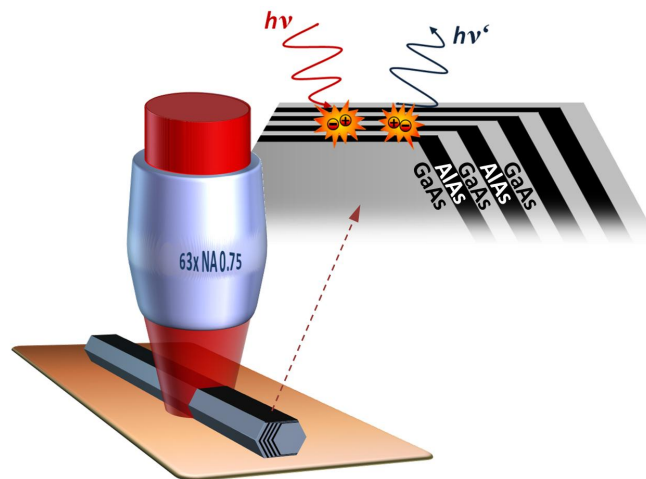
Figure 1.3: Optical spectroscopy on nanowire-based multi-quantum-well heterostructures.

cross-section may lead to novel electron localization effects, for example in the corners of a hexagonal nanowire heterostructure, with major impacts on the electronic transport and optical properties.

1.2 Scope and Objectives of the Thesis

The objectives of the thesis are grouped into the three main categories. The first part of the thesis work mainly concerns about the installation of an optical laboratory for low temperature micro-Raman and micro-photoluminescence experiments on single nanostructures. Afterwards, the main focus is put on the characterization of the doping in GaAs nanowires by Raman spectroscopy in order to gain a deeper understanding of the dopant incorporation mechanisms during the vapor-liquid-solid growth. In the last part of the thesis work, the attention is turned towards fundamental studies on the electronic properties of novel semiconductor materials such as WZ GaAs and on the characteristics of free electron systems in nanowire based heterostructures. For this purpose, advanced resonant Raman techniques are applied.

The thesis is organized in the following way. In the second chapter the theoretical and practical background for this work is reviewed with a special attention for Raman spectroscopy on semiconductor nanomaterials. The third chapter is dedicated to the experimental setup for low-temperature optical spectroscopy that has been installed during the first year of the thesis work. chapter 4 focuses on the doping mechanisms in MBE grown GaAs nanowires. The

incorporation pathways of Si-dopants during the growth of GaAs nanowires are identified and limitations of dopant incorporation are discussed. Direct assessment of the carrier concentration and the mobility by transmission Raman spectroscopy is demonstrated. An insight into the electronic band structure of wurtzite GaAs is given in chapter 5. By means of resonant Raman spectroscopy, the temperature dependence of the crystal-field split of band in the wurtzite phase is examined. A complete picture of the electronic band structure and the arrangement of the bands is given. Resonant Raman scattering in nanowire based heterostructures is the main topic in chapter 6. Here, the formation of a photoexcited plasma is studied in closely spaced AlAs/GaAs multi-quantum wells grown on the side facets of a GaAs nanowire. A final overview of the major results is given in chapter 7.

2 General Background

The current state of research of GaAs nanowire growth is reviewed. The general lattice dynamics in GaAs are briefly discussed. Raman spectroscopy is introduced as a powerful tool in the characterization of semiconductor nanowires. Special attention is given to the electron-phonon interaction in the scattering process and the relevant Raman selection rules for zinc-blende and wurtzite materials.

2.1 Growth and Properties of GaAs Nanowires

2.1.1 Self-Catalyzed Growth of GaAs Nanowires

The GaAs nanowires investigated in this thesis are synthesized by a Ga-assisted vapor-liquid-solid growth process using MBE. The schematics of the growth mechanism are shown in Fig. 2.1. Gallium nanodroplets form by diffusion of Ga adatoms on the surface of a SiO_2-coated GaAs substrate. By gathering As from the vapor phase these droplets act as the seeds of the GaAs nanowire nucleation and growth. The axial growth rate of the wires can be controlled by the partial pressure of the incoming As_4. Additionally, the growth on the facets is found to be much slower, leading to a large aspect ratio of the wires (up to 400:1) [28]. The diameter of the nanowires ranges from 20 to 200 nm and depends on the particular growth conditions.
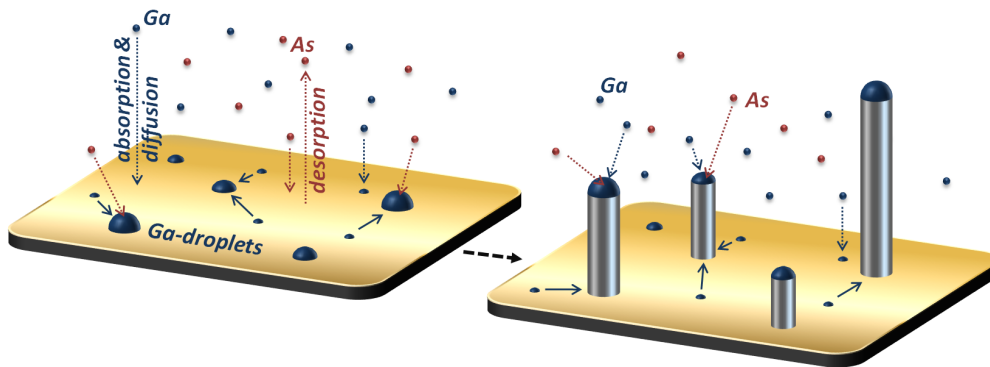
Figure 2.1: Schematics of the gallium-assisted VLS growth of GaAs nanowires.

The crystal orientation of the nanowire follows the direction of the underlying substrate [29]. The wires have a hexagonal cross section with side facets belonging to the {110} crystal family [30]. A high crystalline quality has been proved by transmission electron microscopy, with the presence of imperfections like rotational twins and polytypism between wurtzite and and zinc-blende structures along the axial direction [31]. Recently, III-V nanowires have been successfully integrated on group IV substrates. In the case of GaAs, nanowires have been grown directly on the native oxide of an undoped Si (111) wafer. In this case, the nucleation occurs in a pinhole in the silicon substrate with an epitaxial relation between the substrate and the wire seed.

2.2 Raman Characterization of Semiconducting Materials

Due to its non destructive nature and its high spatial resolution Raman spectroscopy is an important tool for the characterization of semiconductors. Raman scattering by intrinsic phonon modes, which are sensitive to internal and external perturbations, provides information on the composition, phase, crystallinity, or crystal orientation of semiconductors. Moreover, inelastic light scattering gives further insight into the properties of electron or hole gases present in doped materials. Furthermore, Raman scattering by electronic or vibronic excitations is used as a quantitative technique for the assessment of impurity and dopant incorporation [32].

2.2.1 Lattice Dynamics in GaAs

As a semiconductor with zinc-blende crystal structure GaAs crystallizes in a cubic lattice with T_d^2 ($F\bar{4}3m$) symmetry. The zinc-blende structure is composed of two cubic close packed sublattices of anion and cation atoms in a way that atoms of one sublattice occupy tetrahedral interstitial sites of the second sublattice. The underlying Bravais lattice is face-centered cubic with a two-atom basis. The phonon dispersion of ZB GaAs is shown in Fig. 2.2 a. With two atoms per unit cell six phonon branches exist that are divided into three acoustic and three optical branches. The optical phonons at the Γ point consist of two degenerate transverse optical (TO) modes and one longitudinal optical (LO) mode. The long range electric fields associated with long-wave LO are responsible for the phenomenon of LO-TO splitting which results in a slightly higher energy of the LO mode [33].

Table 2.1: Raman active optical phonon modes in ZB and WZ GaAs

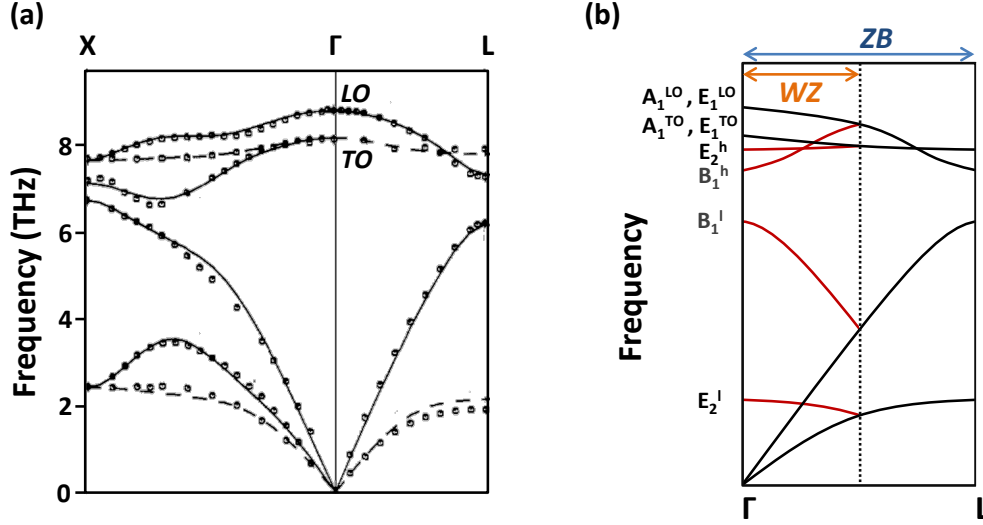| Structure	Mode	Position (cm^{-1})
zinc-blende	TO	267
	LO	291
wurtzite	A_1 (TO)	267
	A_1 (LO)	291
	E_1 (TO)	267
	E_1 (LO)	291
	E_2^h	259
	E_2^l	unknown

Figure 2.2: (a) Phonon dispersion at the Brillouin zone center of ZB GaAs (adapted from [34]). (b) Schematic representation of the phonon dispersion of WZ GaAs as a result of the zone folding of the ZB dispersion relation along $\Gamma \rightarrow L$.

In the nanowire form, GaAs may also crystallize in the hexagonal wurtzite lattice with C_{6v}^4 ($P6_3mc$) symmetry with all atoms occupying C_{3v} sites. With four atoms per unit cell the WZ compounds exhibit nine optical modes. Group theory predicts the following phonons [35]: an A_1 mode polarized in the z direction (the z direction corresponds to the hexagonal c-axis), an E_1 branch with the phonon polarized in the xy plane, two E_2 branches called E_2^l (l for low) and E_2^h (h for high), and two silent B_1 modes. Among these, the polar A_1 and E_1 modes as well as the unpolar E_2 modes are the first-order Raman-active modes. Again, the polar A_1 and E_1 modes split into transverse and longitudinal optical components. Consequently, the polar modes of the WZ crystal exhibit both an LO-TO splitting and an A_1-E_1 splitting due to the anisotropic short-range oder of the hexagonal structure. However, the A_1-E_1 splitting has been shown to be negligible in the case of WZ GaAs [36]. The extent of the Brillouin zone in the WZ phase along the [0001] direction is only half of that in the ZB phase in [111] direction. This leads to the folding of the ZB dispersion relation along $\Gamma \rightarrow L$ with the result that the L-point in ZB appears at the Γ point in WZ [37].

2.2.2 First Order Raman Scattering

Raman scattering corresponds to an inelastic scattering of light, meaning that as a consequence of a scattering event the light is frequency shifted to lower energies (Stokes shift) or

higher energies (anti-Stokes shift) with respect to the incident light, and a quasi-particle like for example a phonon, plasmon, or magnon is created or annihilated, respectively. Within this scattering event both the energy and the momentum are conserved:

$$\omega_s = \omega_i \pm \omega_p \quad and \quad \vec{k}_s = \vec{k}_i \pm \vec{q}_p \tag{2.1}$$

Here, $\omega_{s,i}$ and $\vec{k}_{s,i}$ are the frequencies and wave vectors of the scattered and incident light, and ω_p and $\vec{q}_{s,i}$ is the frequency and wave vector of the quasi-particle. However, as the momentum of light in the visible range is rather small with respect to the size of the Brillouin zone, scattering mainly occurs close to the center of the Brillouin zone, and the phonons participating in the scattering process are long wavelength phonons with $q \simeq 0$.
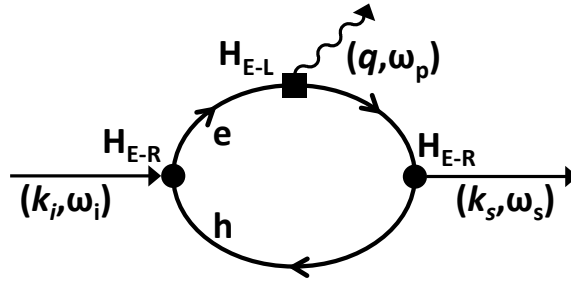
Figure 2.3: Feynman diagram for a first-order Raman scattering process.

In a classical picture, Raman scattering occurs due to the change of the polarizability of a molecular vibration resulting in a radiatory dipole emission of light with a frequency different from the frequency of the incident light [33]. In a quantum mechanical description, first order Raman scattering is explained as a third-order perturbation process: (i) a photon impinging on a semiconductor crystal created first an electron-hole pair, (ii) the electron is scattered by one phonon and loses part of its energy to the phonon, and (iii) the electron recombines and a Raman scattered photon is emitted. The Feynman diagram in Fig. 2.3 illustrates the process [38].

The Raman scattering probability is then given according to Fermi's golden rule [39]:

$$W_{FI} = \frac{2\pi}{\hbar} |\sum_{\alpha\beta} \frac{\langle F|\hat{H}_{E-R}|\beta\rangle \langle \beta|\hat{H}_{E-L}|\alpha\rangle \langle \alpha|\hat{H}_{E-R}|I\rangle}{(\hbar\omega_l - E_\beta + i\Gamma_\beta)(\hbar\omega_s - E_\alpha + i\Gamma_\alpha)} + C|^2 \times \delta(\hbar\omega_l - \hbar\omega_s - \hbar\omega_p) \tag{2.2}$$

13

where F and I denote the final and initial states, and α and β are the intermediate states of the scattering process. The Hamiltonians $\hat{H}_{E-R}$ and $\hat{H}_{E-L}$ represent the electron-photon (radiation) and electron-lattice interaction, respectively. $\Gamma_{\alpha,\beta}$ are the damping constants. From the denominators of equation 2.2 one notices that resonances in the Raman scattering occur when the frequency of the incident laser light ω_l is in the vicinity of E_β (*"incoming"* resonance) or $E_\alpha + \hbar\omega_p$ (*"outgoing"* resonance).

2.2.3   Electron-Phonon Interaction in the Raman Scattering Process

The first-order Raman scattering from a polar III-V compound material implies two types of electron-optical phonon interaction. A long-wavelength optical phonon results in a microscopic distortion in the crystal due to the relative displacement of atoms to each other within the unit cell. Such microscopic distortions may modify the electronic energies resulting in the short range *deformation potential* interaction between electrons and phonons. As explained above, a long-wavelength LO phonon in a polar crystal generates a macroscopic electric field that also interacts with electronic states. This long-range electron-LO phonon interaction is called *Fröhlich interaction* [33]. Two mechanisms contribute to the Fröhlich scattering from LO phonons. They are referred to 'allowed' or 'forbidden' mechanisms according to whether or not they follow the selection rules imposed on the Raman tensor by the symmetry of the long-wavelength phonons. 'Allowed' Fröhlich scattering, also called electro-optic scattering or interband scattering, follows the same selection rules as the deformation potential scattering from LO phonons. 'Forbidden' scattering is due to the Fröhlich intraband interaction. In resonant conditions, i.e. when the incident or scattered photon energies are close to an optical transition, the forbidden scattering can make important contributions to the observed Raman scattering [40, 41]. In addition to the 'intrinsic' forbidden Fröhlich interaction impurities ('extrinsic' defects) can also contribute to the resonant scattering process. In the defect induced process the quasi-momentum conservation is relaxed, and thus phonons with larger q-vectors from the entire Brillouin zone can participate in the Raman scattering. These larger q-vectors greatly enhance the intraband Fröhlich contribution giving rise to intense LO resonant Raman scattered peaks [42, 43].

2.2.4   Raman Selection Rules

The intensity of the Raman scattered radiation scales with the polarization induced by a phonon (or a similar fluctuation) in the crystal. Therefore, in order to calculate the Raman

intensity, fluctuations in the susceptibility tensor χ_{ij} due to atomic vibrations have to be evaluated. The susceptibility can be expanded with respect to the normal coordinates Q_k [33]:

$$\chi_{ij} = (\chi_{ij})_0 + \sum_q (\frac{\partial \chi_{ij}}{\partial Q_q})_0 \times Q_q + \sum_{q,m} (\frac{\partial^2 \chi_{ij}}{\partial Q_q \partial Q_m})_0 \times Q_q Q_m + ... \tag{2.3}$$

Here, i and j extend over the coordinates 1-3 and q runs over the $3N-3$ normal coordinates of the vibrations (N is the number of atoms in the unit cell). The component $\partial \chi_{ij}/\partial Q_q$ of the derived polarizability tensor is known as the Raman tensor $\boldsymbol{R}$. This second-rank tensor has been introduced in order to evaluate the intensity of the scattered radiation and the symmetry of the scattered phonon. The Raman scattered intensity is proportional to

$$I_s \propto |\hat{e}_i \cdot \boldsymbol{R} \cdot \hat{e}_s|^2 \tag{2.4}$$

where $\hat{e}_{i,s}$ is referred to the polarization direction of the incident and scattered light.

For zinc-blende GaAs with T_d symmetry the Raman tensors for the Γ_{15} phonons are given by [38]:

$$\boldsymbol{R}(X) = \begin{pmatrix} 0 & 0 & 0 \\ 0 & 0 & d_1 \\ 0 & d_1 & 0 \end{pmatrix}, \quad \boldsymbol{R}(Y) = \begin{pmatrix} 0 & 0 & d_1 \\ 0 & 0 & 0 \\ d_1 & 0 & 0 \end{pmatrix}, \quad \boldsymbol{R}(Z) = \begin{pmatrix} 0 & d_1 & 0 \\ d_1 & 0 & 0 \\ 0 & 0 & 0 \end{pmatrix} \tag{2.5}$$

The crystal coordinates X,Y, and Z are defined as [100],[010], and [001], respectively. These tensors apply for the deformation potential scattering and the allowed Fröhlich scattering. In the case of the forbidden intraband Fröhlich interaction, the Raman scattering obeys new

selection rules according to the diagonal Raman tensor [41]:

$$\boldsymbol{R}_{forbidden-Fröhlich} = \begin{pmatrix} d_2 & 0 & 0 \\ 0 & d_2 & 0 \\ 0 & 0 & d_2 \end{pmatrix} \tag{2.6}$$

and scattering only occurs only for parallel polarization of the incident and scattered light $(\hat{e}_i \parallel \hat{e}_s)$.

For wurtzite GaAs with C_{6v}^4 symmetry the Raman tensors are given by [35]:

$$\boldsymbol{A_1}(z) = \begin{pmatrix} a & 0 & 0 \\ 0 & a & 0 \\ 0 & 0 & b \end{pmatrix}, \quad \boldsymbol{E_1}(x) = \begin{pmatrix} 0 & 0 & c \\ 0 & 0 & 0 \\ c & 0 & 0 \end{pmatrix}, \quad \boldsymbol{E_1}(y) = \begin{pmatrix} 0 & 0 & 0 \\ 0 & 0 & c \\ 0 & c & 0 \end{pmatrix}, \quad \boldsymbol{E_2} = \begin{pmatrix} d & d & 0 \\ d & -d & 0 \\ 0 & 0 & 0 \end{pmatrix}$$
$$\tag{2.7}$$

Structure	Configuration	Allowed modes
zinc-blende	$x(-,-)\bar{x}$	TO
wurtzite	$x(y,y)\bar{x}$	E_2, A_1 (TO)
	$x(y,z)\bar{x}$	E_1 (TO)
	$x(z,z)\bar{x}$	A_1 (TO)
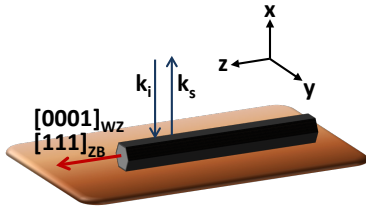
Figure 2.4: Geometry for backscattering from nanowires.

Table 2.2: Allowed phonon modes for backscattering from ZB and WZ GaAs nanowires.

The allowed modes for the typical backscattering experiment shown in Fig. 2.4 on WZ or ZB GaAs nanowires are given in table 2.2. The Porto notation $\hat{k}_i(\hat{e}_i, \hat{e}_s)\hat{k}_s$ is used to describe the scattering geometry. Here $\hat{k}_{i,s}$ are the directions and $\hat{e}_{i,s}$ the polarizations of the incident and scattered photons. While in ZB backscattering from the {110} nanowire facets is only allowed for TO phonons, the E_2^h, A_1 (TO), and E_1 (TO) modes are observable in the WZ phase [37].

3 Installation of the Experimental Setup

During the first year of the PhD work, a non-commercial optical setup for Raman spectroscopy with the option to serve also as photoluminescence spectroscopy setup has been built. It allows micro-Raman and micro-photoluminescence experiments on single nanowires with a diffraction limited resolution of a few 100 nm. Measurements can be performed in a wide temperature range from 4.2 - 340 K. Various excitation lasers covering the visible and near-infrared range are available for resonant Raman experiments or photoluminescence excitation spectroscopy.

3.1 Introduction

In retrospect, the original experiment implemented by Sir Chandrasekhara Venkat Raman in 1928 was remarkably simple. With only the bright Indian sunlight serving as a sufficiently powerful light source and the bare human eye as a 'detector', Raman was able to observe the inelastic light scattering process for the first time within a liquid benzene sample.

Figure 3.1: Sir Chandrasekhara Venkata Raman in front of his historic experimental setup (from Ref. [44]).

Today, the development of intense and monochromatic lasers and more sensitive detectors rendered the possibility to perform micro-Raman spectroscopy on even single nanostructures with a diffraction limited spatial resolution of several 100 nm [45].

3.2 Installation of a Micro-Raman Setup

The schematic of the experimental setup is shown in Fig. 3.2. The core of the setup is a TriVista 555 triple spectrometer that provides the necessary dispersion to separate the weak Raman scattering from the intense Rayleigh scattered light. It is equipped with a thermoelectrically cooled charge-coupled device (CCD) detector. Various laser sources are available for different applications. An Argon/Krypton laser offers ten discrete wavelength between 476 nm and 676 nm, an additional HeNe gas laser emits at 632.8 nm. For resonant Raman experiments, a continuous wave titanium-sapphire laser can be tuned from 700 nm to 970 nm. Furthermore, a supercontinuum white light laser is available which serves as a continuous light source for photoluminescence excitation experiments.

The basic optical ray diagram of the spectroscopy system is shown in Fig. 3.3. At first, the parallel laser beam passes a dispersive grating and a subsequent aperture, with the objective to attenuate the background plasma and secondary emission of the laser source. Neutral
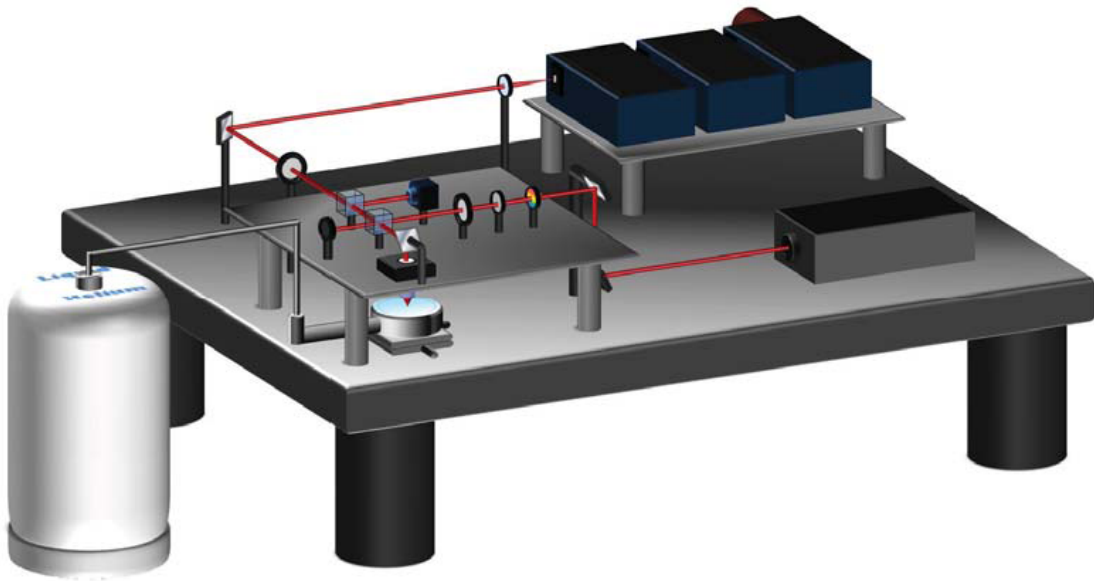
Figure 3.2: Schematic of the setup for low-temperature micro-Raman and photoluminescence spectroscopy.

density filters diminish the laser power. The laser beam is then deflected by a beam splitter and focused on the sample with a 100x objective with numerical aperture (NA) 0.95. Polarizing optics can be placed before. The sample itself is positioned on a XYZ piezo-stage with a closed-loop displacement range of 80 μm in the three spatial directions. A LabView routine has been implemented to automatically scan the surface with a precision of 2 nm. This allows two-dimensional Raman imaging and photoluminescence mapping of the sample surface. After the interaction with the sample, the scattered light that comprises both the Raman and Rayleigh scattered light is collected by the same objective lens and directed towards the spectrometer for analysis. Polarization analysis of the collected Raman light can be achieved by placing a linear polarizer before the spectrometer. A high quality achromatic lens is used to focus the light onto the entrance slit of the spectrometer. Gratings with groove densities from 900– 1800 grooves/mm can be selected for varying spectral resolutions and are suitable for different applications and exciting wavelengths. A temperature-controlled liquid helium flow cryostat has been installed that enables experiments within a temperature range between 4.2 and 350 K. In combination with the cryostat a cover-glass corrected 67x objective with NA 0.75 is used in order to minimize image distortions due to the cryostat window.
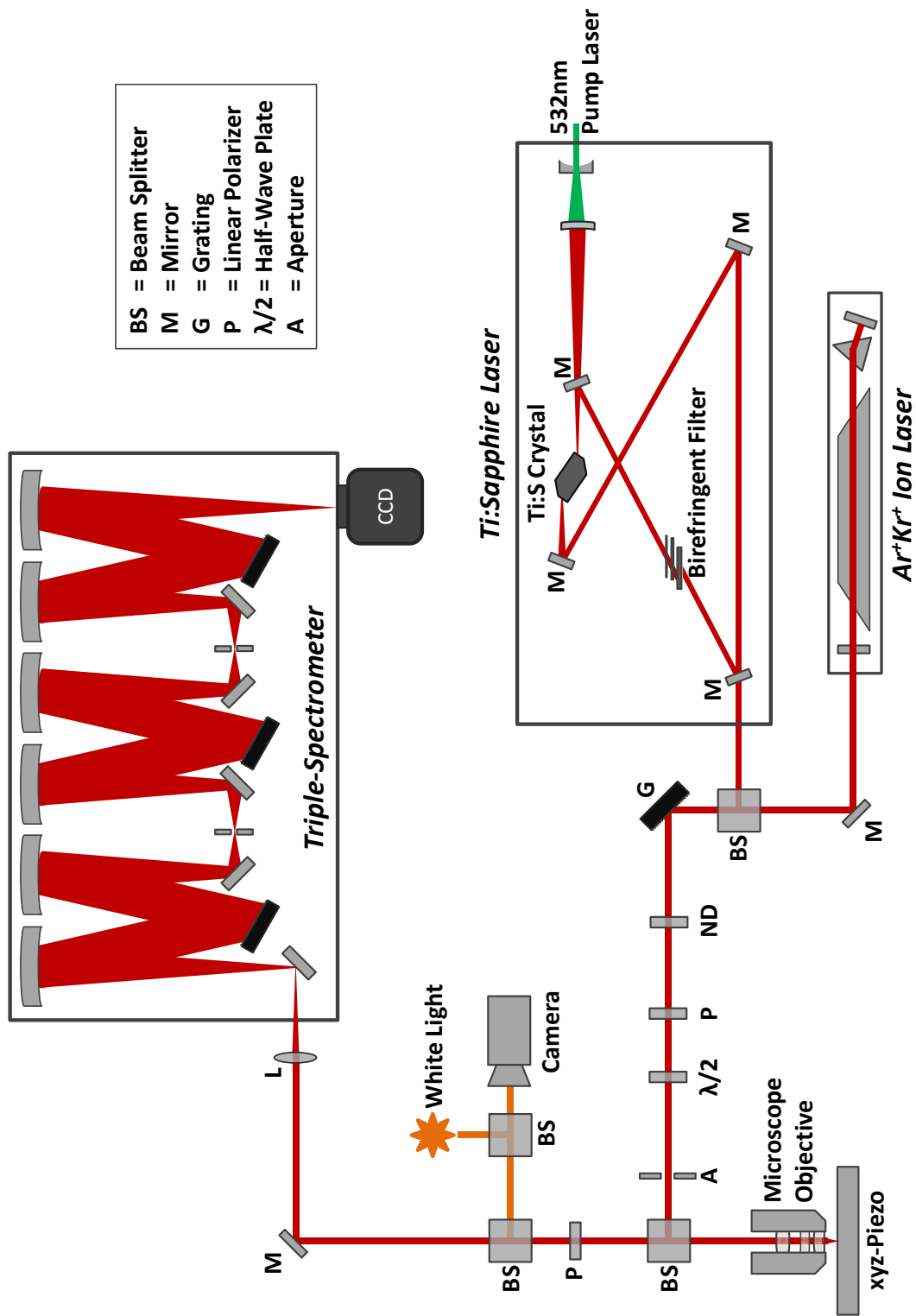
Figure 3.3: Optical ray diagram.

4 Doping of GaAs Nanowires

The doping of GaAs nanowires with silicon is studied in this chapter. Along with theoretical considerations, the doping mechanisms in catalyst-free GaAs nanowires grown by MBE are revealed. Two competing mechanisms are important: dopant incorporation from the side facets during the radial growth and from the gallium droplet during the axial growth. Doping compensation plays an important role as a limiting factor of doping in compound semiconductor nanowires. For Si-concentrations up to 1.4 $x10^{18}$ cm^{-3}, silicon incorporates mainly in arsenic sites. For higher concentrations, the formation of neutral silicon pairs is observed. This can be related to the Coulomb interaction between charged defects during growth. It may result in an electrical deactivation of more than 85% of the silicon acceptors. Direct assessment of the carrier concentration and the mobility has been achieved by Raman scattering from coupled LO-phonon plasmon modes in forward scattering geometry.

4.1 Background

4.1.1 Doping of Semiconductor Nanowires

Understanding the nanowire growth in the presence of impurities and the mechanism of dopant incorporation is critical for a rational synthesis. Both p-type and n-type doping behavior has been demonstrated in nanowires [46, 1]. Doping of III-V semiconductor nanowires has been shown for example in the case of inclusion of magnetic impurities [47], by including zinc in the growth process [48], or by silicon and beryllium incorporation during the growth of GaAs nanowires [49].

The doping mechanisms have been investigated in the case of vapor-liquid-solid growth of silicon nanowires by chemical vapor deposition (CVD). Here, it has to be taken into account that the nanowire not only grows along the axial direction via the VLS mechanism, but also the nanowire diameter increases constantly with time due to a radial overgrowth at the vapor-solid (VS) interface. Indeed, it has been shown that the dopant incorporation occurs simultaneously from the side facets during the radial growth of the nanowire and through the liquid catalyst during the axial nanowire growth. The differences in the precursor decomposition rates between the solid nanowire surface and the liquid catalyst lead to the formation of a doped shell and a much lower doped core [50, 51].Consequently, a non-uniform doping profile exists the wire axis as shown in Fig. 4.1.
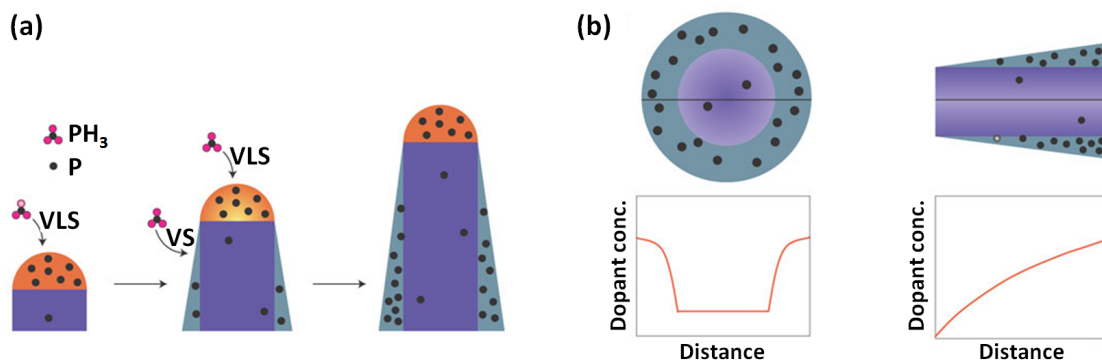
8

Figure 4.1: (a) Phosphorus (grey) from a PH_3 precursor is incorporated into Ge nanowires from the sides through the vapor-solid interface (VS) or through the catalyst by the VLS mechanism. These two incorporation pathways proceed at different rates, leading to a heavily doped shell and a lower doped core. (b) Radial (left) and longitudinal (right) view of the dopant distribution (adapted from Ref. [20]).

Evidence of this surface doping has been seen for example by atom probe tomography [50], by electrical characterization [52], as well as by Raman spectroscopy [53]. Recently, uniform longitudinal and radial dopant concentration profiles have been observed in phosphorus doped silicon nanowires by means of scanning photocurrent microscopy and Kelvin probe force microscopy. This was achieved by a thermal annealing step following the growth [54]. However, the lessons learnt in studies of nanowires grown by CVD based methods cannot be directly applied to the case of III-V nanowires grown by MBE. The reason for that is that growth mechanisms differ to a large extent and the surface chemistry phenomena such as precursor decomposition are significantly less thermally activated [55, 56, 28].

4.1.2 Doping Processes in GaAs Compared for Different Growth Techniques

As it has been mentioned here above, the doping characteristics strongly depend on the nature of the applied growth technique. For gallium-assisted MBE growth of nanowires, doping can be either incorporated through the gallium droplet and/or directly on the facets. Liquid-phase epitaxy (LPE) is a model system, indicative for the incorporation pathway through the catalyst droplet, while MBE thin film growth can serve as a reference for the overgrowth of doped layers on the (110) side facets of the GaAs nanowires (compare Fig. 4.1).

In LPE dopants are incorporated through the liquid-solid interface. For single donors and acceptors in GaAs a linear relationship between the impurity concentration in the semiconductor and in the concentration in the liquid phase has been found, even if the resulting carrier concentrations is well above 10^{19} cm^{-3} [57]. Si-doped LPE GaAs is always compensated, which means that there are concentrations of Si$_{Ga}$ donors and Si$_{As}$ acceptors present at the same time [19]. However, it has been shown that growth conditions such as temperature can influence that p or n doping prevails. At higher doping levels, Si$_{Ga}$-Si$_{As}$ pairs are also observable [58]. A maximum hole concentration for Si doped p-type GaAs of 6 x 10^{18} cm^{-3} has been reported [59].

Silicon is most commonly used as n-type dopant in MBE grown (100) oriented GaAs thin films leading to carrier concentrations of up to 5 x 10^{18} cm^{-3}. A great majority of Si atoms being incorporated as Si$_{Ga}$ donors [60, 61]. In contrast, n-type (110) films show 30-40% lower free-electron concentrations than their (100) counterparts. Mobilities of n-type (110) films are indicative of high compensation because of the co-incorporation of silicon-related acceptor centers like Si$_{As}$ shallow acceptors. By lowering the As$_4$/Ga flux ratio and increasing the growth

temperature the site occupancy preference of incident silicon atoms changes from Ga to As sites. Thus, the growth of p-type GaAs on (110) oriented GaAs substrates becomes possible [62]. The strongly amphoteric behavior of silicon dopants and the resulting autocompensation of silicon donors and acceptors is a challenge and should be taken into account for the epitaxial growth on (110) oriented GaAs surfaces.

4.1.3   Raman Scattering from Local Vibrational Modes of Silicon Dopants in GaAs

Important information about impurity lattice sites can be obtained from local vibrational mode (LVM) spectroscopy. For example, Si occupying a lattice site in GaAs is lighter than the atoms of the host lattice giving raise to spatially localized vibrational modes with frequencies higher than the ones of the GaAs modes [60]. These LVMs can be detected by Raman spectroscopy or infrared absorption techniques. A typical Raman spectrum of the local vibrational modes is shown in Fig. 4.2.
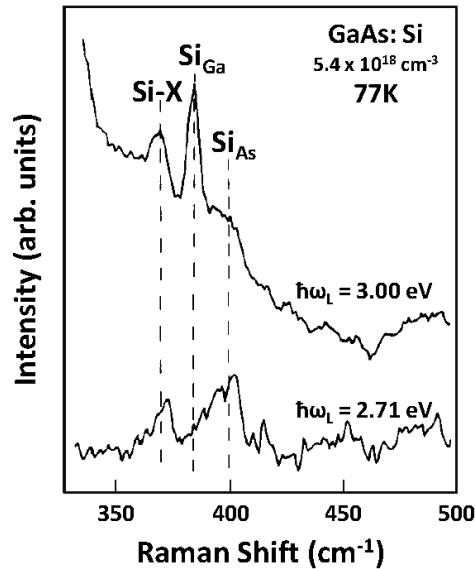
Figure 4.2: Low temperature (77 K) Raman spectra of MBE grown Si doped GaAs excited with two different photon energies of 3.00 eV and 2.71 eV (adapted from Ref. [63]).

For example, Si_{Ga} donors having four As neighbors give rise to a sharp LVM in the Raman spectrum at 384 cm^{-1}. The LVM of compensating Si_{As} acceptors is found at 399 cm^{-1} in case that the n-type behavior prevails in the GaAs sample. In contrast, in p-type GaAs the Si_{As} acceptor is down-shifted from its usual frequency to around 396 cm^{-1} due to a Fano resonance effect in the hole-phonon interaction. When both Si_{As} acceptors and Si_{Ga} donors are present

Table 4.1: Vibrational frequencies of Si complexes in GaAs [60].

Defect	ν cm^{-1}	Comment
Si$_{Ga}$	384	
Si$_{As}$	399	for overall n-doping
Si$_{As}$	396	for overall p-doping
Si$_{Ga}$-Si$_{As}$	393, 464	

in important concentrations, nearest-neighbor Si$_{Ga}$-Si$_{As}$ pairs may form with LVMs at 393 cm^{-1} and 464 cm^{-1}. Other defects like for example the so called Si-X center at 369 cm^{-1} that is related to a Si$_{As}$-Ga vacancy (V$_{Ga}$) complex may also be detected in the Raman spectrum. A summary of the relevant LVM frequencies is given in table 4.1 [60].

As shown in Fig. 4.2, resonance effects play an important role in Raman scattering from LVMs. In the special case of Si dopants in GaAs, the resonance enhancement of the LVM has been extensively studied by Ramansteiner et al. [64]. Interestingly, a different resonance behavior has been found for scattering from Si donors on Ga sites and for Si acceptors on As sites. On the one hand, the Si$_{Ga}$ shows a very narrow resonance at the E$_1$ energy gap of GaAs. This means that the Si$_{Ga}$ LVM is only observable in the Raman spectrum if the laser energy is very close to 3.0 eV (e.g. the 413.1 nm line of a Kr$^+$ ion laser). In resonance, a detection limit of around 10^{18} cm^{-3} Si$_{Ga}$ donors can be achieved. On the other hand, the resonance of the Si$_{As}$ LVM at the E$_1$ gap is much broader, meaning that the mode is observable over a much larger energy range from about 2 to 3 eV.

4.1.4 Raman Scattering from Coupled LO-Phonon-Plasmon Modes

In semiconductors, the activated free-carrier concentration and mobility is traditionally determined by magnetoelectronic measurements based on the Hall effect. In polar materials, such as GaAs, Raman scattering has also proven to be able to determine these physical properties [65]. Here, a coupling between the longitudinal optical phonons and the longitudinal plasma oscillations of the free carriers occurs, moderated by the macroscopic field created by both types of excitations. The coupled modes that result from this interaction were first observed in the Raman spectra of n-type GaAs by Mooradian and Wright in 1966 [66]. In n-type III-V semiconductors with a sufficiently high carrier mobility, such as in epitaxially grown n-GaAs, two coupled phonon LO phonon-plasmon modes appear in the spectrum with frequencies ω^+ and ω^-. This effect is illustrated in the spectra of Fig. 4.3 a. In a semiclassical dielectric

theory within the long wavelength approximation, the frequencies of these coupled modes can be described by the zeros of the dielectric response function that is written as the sum of a Drude term for the free carriers and a Lorentzian term for the phonons [67]:

$$\epsilon(0,\omega) = \epsilon_\infty + \frac{\epsilon_0 - \epsilon_\infty}{1 - \omega^2/\omega_{TO}^2} - \frac{\omega_p^2 \epsilon_\infty}{\omega^2} \tag{4.1}$$

ϵ_0 is the vacuum dielectric constant, ϵ_∞ the high frequency dielectric constant, ω_{TO} the frequency of the TO mode, and ω_p the plasma frequency. The frequencies of the coupled modes only depend on the plasma frequency:

$$\omega_p^2 = \frac{ne^2}{\epsilon_0 \epsilon_\infty m_e^*} \tag{4.2}$$

Consequently, the free electron concentration n can be deduced from the position of the modes in the experimental spectra (m_e^* denotes the effective electron mass). This dependence of the coupled mode position on the plasma frequency is shown in the inset of Fig. 4.3 a. A more detailed theoretical discussion of the plasmon-phonon coupling in n-type semiconductors taking into account the contributions from the allowed deformation potential and interband Fröhlich interaction, the forbidden intraband Föhlich interaction, and scattering due to charge-density fluctuations can be found in Ref. [68].

The situation is different in p-type GaAs. Here, not only the carrier mobility is much lower, but also heavy and light holes contribute to the free carrier plasma. As a consequence of the large carrier damping related to the low mobility and high effective hole mass, only one coupled LO-phonon-plasmon mode is observed in the spectra with a position between the LO and TO peak of GaAs, while the second mode is damped out. This behavior has been found for Raman scattering in p-type GaAs doped with Zn [70], Be [71, 72, 73, 74], C [75], and Si [76] for a broad range of carrier concentrations. Experimental Raman spectra for carrier concentrations between 9.1 x 10^{17} and 2.9 x 10^{19} are show in Fig. 4.3 b. With increasing carrier concentration a decrease in the LO intensity and a broadening of the LO mode is observed. At high doping concentrations, the coupled mode shifts from the position of the original LO mode towards the TO position. Fig. 4.3 b also shows that the unscreened LO phonon mode can be still visible
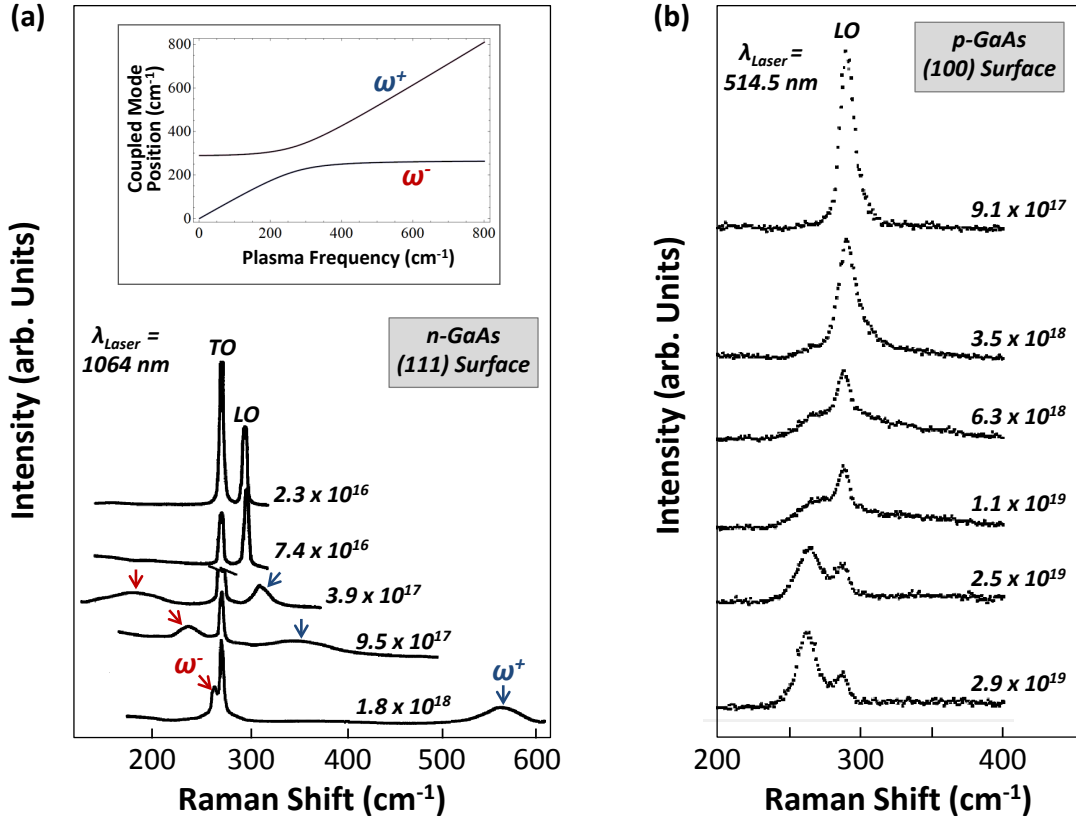
Figure 4.3: (a) Room temperature Raman spectra of n-type GaAs for different free carrier concentrations (adapted from Ref. [66]). The positions of the coupled modes ω^+ and ω^- are indicated by arrows. The inset shows the calculated coupled mode position as a function of the plasma frequency. (b) Typical room temperature Raman spectra of p-type GaAs samples with varying free carrier concentration (adapted from Ref. [69]). With increasing carrier concentration the LO mode broadens and shifts towards the position of the TO mode due to the interaction with the strongly damped hole plasma.

in the Raman spectrum due to the presence of a depletion layer at the surface. Therefore, the intensity of this unscreened LO mode also contains information on the width of the depletion layer that is related to the doping level in the bulk [77].

The interaction between a strongly damped hole plasma and the damped LO phonon can be described by introducing phenomenological damping terms into the dielectric function of the coupled mode system [72]:

$$\epsilon(0, \omega) = \epsilon_\infty + \frac{\omega_{LO}^2 - \omega_{TO}^2}{\omega_{TO}^2 - \omega^2 - i\gamma\omega} - \frac{\omega_p^2}{\omega^2 + i\Gamma_p\omega} \tag{4.3}$$

Here, Γ_p and γ are the damping constants of the LO phonon and the hole plasma, respectively. Taking into account both the allowed deformation potential and interband Fröhlich interactions, the Raman scattering intensity by the coupled LO-phonon-plasmon mode is given by [72]:

$$I(\omega) = A(n_\omega + 1) \frac{[\omega_{TO}^2(1 + C) - \omega^2]^2}{(\omega_{TO}^2 - \omega^2)^2} \times Im[-1/\epsilon(0, \omega)] \qquad (4.4)$$

where A is a constant factor, n_ω the Bose-Einstein distribution, and C the Faust-Henry coefficient. The theory of scattering by coupled LO-phonon-plasmons in p-type GaAs has been described in detail by Irmer et al. [78].

Finally, the plasma damping constant Γ_p is related to the relaxation time τ of the free carriers and their mobility μ by the term:

$$\Gamma_p = \frac{1}{\tau} = \frac{e}{\mu m_h^*} \qquad (4.5)$$

In GaAs, the average effective hole mass is typically estimated by $m_h^* = (m_{lh}^{*3/2} + m_{hh}^{*3/2})/(m_{lh}^{*1/2} + m_{hh}^{*1/2}) \approx 0.38 m_0$ using the corresponding values for the light and heavy hole mass [79]. Consequently, the hole mobility can be extracted from a lineshape-analysis of the Raman spectra [80].

4.2 P-Doping Mechanisms in Gallium Arsenide Nanowires

4.2.1 Introduction

Controlling the p-type doping in GaAs nanowires is not only an important technological step for making efficient devices, but it also provides a basis for advanced fundamental experiments in the quantum transport regime. For example, p-doped GaAs nanowires may be extremely suitable for the realization of electrostatically defined quantum dots with few electrons in the spin blockade regime and for the studies of the carrier-carrier interactions [81, 82]. Recently, a radial nanowire solar cell composed by an external n-type layer followed by an intrinsic and p-type layer toward the center of the nanowire has been demonstrated by our group [9]. This shows that both p- and n-type doping can be achieved using silicon as a dopant. One has to note that n-type doping was only observed in case of the intentional overgrowth of an external doped shell using lower growth temperatures and higher Ga-fluxes as in the VLS growth. However, the doping mechanisms in the GaAs nanowires still rises several questions. Especially, it is not known which incorporation pathways the silicon dopants take: through the liquid-catalyst droplet during the axial nanowire growth or from the side facets as a result of the radial overgrowth in the MBE.

Therefore, in order to understand the p-doping mechanisms in catalyst-free gallium assisted grown GaAs nanowires, Raman spectroscopy and multicontact transport experiments are combined on the same nanowire[1]. A schematic of the measurement principle is shown in Fig. 4.4. The two techniques provide complementary information on the doping process: transport experiments give information on the electronic properties and doping activity of the incorporated impurities, while Raman spectroscopy reports on the incorporation sites of impurities and lends understanding to their distribution within the sample.

4.2.2 Experimental

The p type GaAs nanowires were obtained by molecular beam epitaxy in a Gen II MBE system [28]. The nanowire growth was carried out at a nominal Ga growth rate of 0.25 Å/s, As_4 partial pressure of 2.7 x 10^{-6} mbar, corresponding to Ga rich conditions, at a temperature of 630 °C and with 7 rpm rotation. Silicon was added to the growth process at the beginning of the growth process. A flux of 1.62 x 10^{12} at. Si/(cm^2 s) was obtained by heating the Si cell

---

[1]the transport experiments have been performed by Joseph Dufouleur, Carlo Colombo, and Tonko Garma
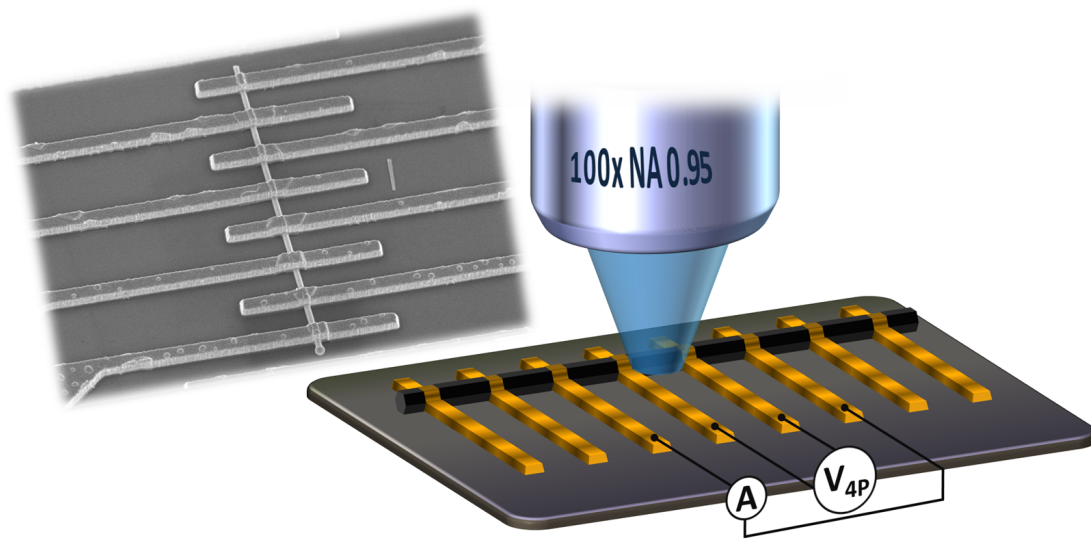
Figure 4.4: Schematics of the experimental set up in which both Raman spectroscopy and electrical transport in 4 point configuration is measured on the same point of the nanowire The inset shows a scanning electron micrograph of a GaAs nanowire with the fabricated multicontacts.

with 13 A. In our MBE system, this typically leads to a concentration of about 6 x 10^{18} cm^{-3} in thin films obtained for a growth rate of 2.8 Å/s. The nanowire growth rate under these conditions is 5.5 μm/h (15 Å /s). The nanowires were grown for 4 h, leading to nanowires 22 μm long and with a diameter ranging between 180 and 70-90 nm (from the bottom to the tip). As mentioned before, silicon is an amphoteric impurity in GaAs, which means that the incorporation of silicon can lead to n or p type doping, depending on whether it is incorporated in As or Ga sites [83, 84]. One should note that the type of incorporation depends on the growth facet and temperature. For {001} facets, n-type doping is mostly achieved, whereas for {111} and {110} facets, both types of doping can occur [60]. The structure has been analyzed by high resolution transmission electron microscopy. No difference in the structure between nanowires grown with and without silicon was observed. The structure corresponds to 100% zinc-blende with single twins spaced between 30 and 500 nm. Multiple electric contacts were fabricated regularly spaced along the entire nanowire. For this, the nanowires were transferred on an oxidized Si wafer. The contacts were defined by a typical process of positive electron beam lithography [85]. After the development of the resist, the samples were exposed to a short O$_2$ plasma cleaning, the oxide at the surface of the nanowires was removed by dipping the sample in a 1:2 HF solution for about 2 s. Immediately after, the metal layer consisting of Ti/Pd/Ti/ Au (10/65/65/50 nm) was evaporated. The width of the contacts was varied between

250 and 1000 nm, for different samples. In order to enable a simultaneous measurement of the regions between contacts with Raman spectroscopy, the distance between two contacts was kept larger than the size of the illumination spot of approximately 800 nm. They were spaced between 0.8 and 1.3 μm. We did not observe any abnormal contact resistance increase by reducing the contact size, even for the thinnest contact of 150 nm.

The nanowire resistance was measured both in two and four point configurations, denoted as R_{2p} and R_{4p}, respectively. The four point configuration has the advantage of avoiding the parasitic effect of the contact resistance. In contrast, the values of the nanowire resistance obtained by measuring in two point configuration generally constitute an overestimation of the real value. All of the transport measurements were performed at room temperature using a needle probe station equipped with a source meter unit used as a DC-polarization voltage source and DC-current meter and a high impedance voltage meter. The electrical contact scheme in R_{4p} configuration is shown in Fig. 4.4: the polarization voltage was applied between the exterior contacts, while the voltage drop was measured with the high impedance multimeter between the two central contacts.

The Raman measurements were realized in backscattering geometry using the 488 nm line of an Ar^+Kr^+ laser for excitation. The laser was focused on the nanowire with a 100x objective (0.95 NA). The power of the incident light was 500 μW (equivalent to 25 kW/cm^2). Special care was taken to ensure that the nanowires were not heated. Prior to the measurements, the contacted nanowires were located by imaging the surface through the microscope objective with a CCD.

4.2.3 Results and Discussion

A typical Raman spectrum of a doped GaAs nanowire is shown in Fig. 4.5. The peaks at 265 and 288 cm^{-1} correspond to the transverse optical (TO) and longitudinal (LO) phonon modes of GaAs. At wavenumbers around 395 cm^{-1}, a peak with lower intensity is present. It corresponds to the local vibrational mode (LVM) of the silicon in GaAs. In particular, this mode corresponds to the presence of substitutional silicon in arsenic sites in p-doped GaAs [60]. This implies that silicon acts as a p type dopant in the GaAs nanowires. The presence of Si in Ga sites would be detected in 384 cm^{-1} [86]. In this measurement configuration, the intensity of the TO mode is proportional to the volume probed. The intensity ratio between the LVM and the TO mode (I_{LVM}/I_{TO}) should be proportional to the concentration of silicon incorporated in the volume
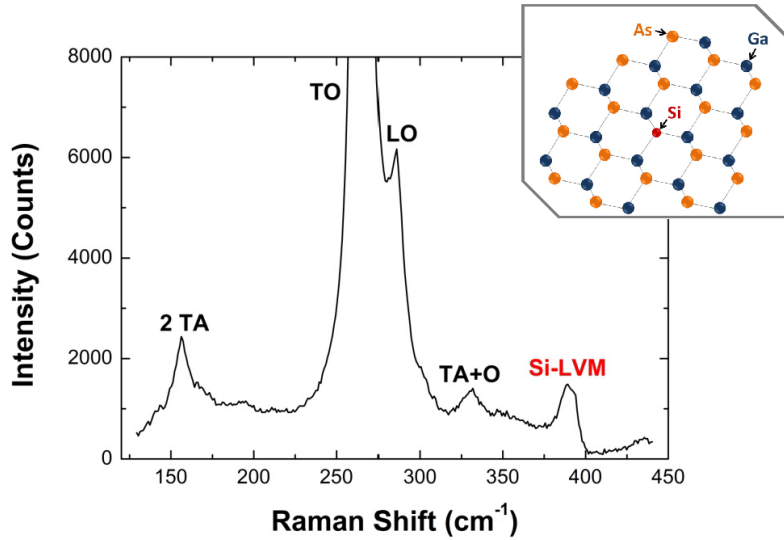
Figure 4.5: Raman spectrum of a single GaAs nanowire doped with silicon. The local vibrational mode (LVM) at 393 cm^{-1} corresponds to the incorporation of silicon in arsenic sites as schematically shown in the inset.

probed by the laser beam. One should note here that the Raman information depth at the excitation wavelength is approximately 40 nm, meaning that Raman strictly reports on the relatively external shell [87].

To gain information on the existence and relative concentration in of the Si dopants, Raman spectra have been measured along the nanowire between each electrical contact pair as shown in Fig. 4.4. The evolution of the I_{LVM}/I_{TO} ratio along the nanowire is plotted in Fig. 4.6 a. The Raman spectra have been measured in between the contacts of the nanowire shown in the inset of Fig. 4.6. The silicon concentration increases along the nanowire from top to bottom.

In order to gain further understanding, a complementary investigation with alternative characterization techniques is needed. R_{4p} was measured along the wire, with the exception of the first and last point, which for geometrical reasons cannot be realized in a R_{4p} configuration. At the extremes of the nanowire, the resistivity is extracted from the measurement of R_{2p} at high bias voltage. The results of a representative nanowire are shown in Fig. 4.6 b. The resistivity decreases along the nanowire from the nanowire tip to the bottom. This variation of the resistivity can be as high as one order of magnitude from one side to the other for a 20 μm long nanowire. The resistance per length can be as low as 2 x 10^{10} Ω.m^{-1} for a diameter of about 200 nm, demonstrating the possibility of efficient doping in GaAs nanowires. The decrease in resistivity correlates with the increase in the silicon concentration measured by
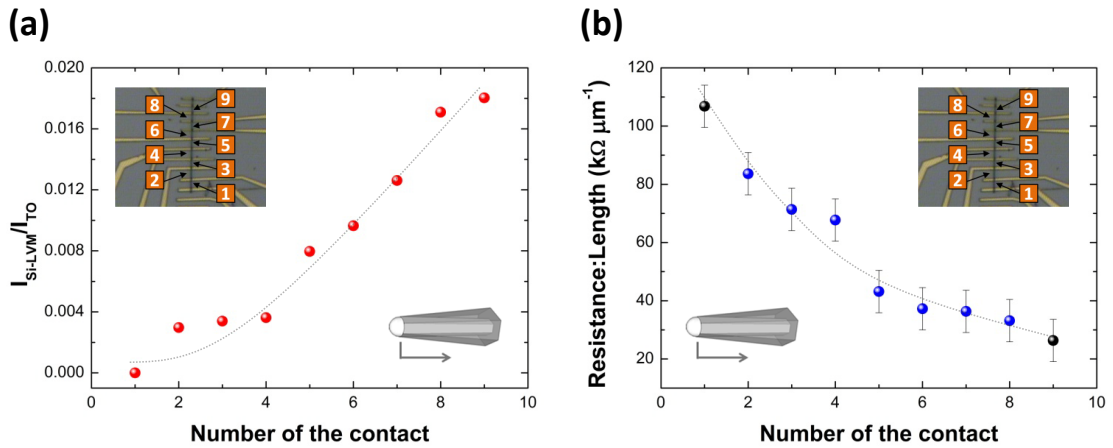
(a)

(b)

Figure 4.6: (a) Intensity of the Si LVM as obtained by Raman spectroscopy. (b) Resistance per length extracted from four points measurements (blue) and two points measurements at high bias (black). The numbers in the optical image of the contacted nanowire indicate the points where measurement have been performed.

Raman spectroscopy. The variation in resistance of a semiconductor can be due both to a variation in doping and/or to a change in the carrier mobility. At room temperature, the mobility of GaAs is dominated by the optical phonon scattering and the crystalline quality, the effect of doping concentration remaining extremely small [84]. As structural inhomogeneity have not been observed in the nanowires, a variation in carrier mobility can in principle be excluded. The most plausible cause for the spatial dependence of the resistivity seems to be a non-homogeneous doping along the nanowire.

Now, the question that arises is whether the incorporation is limited to an external shell or also extended to the nanowire core. Such a question is directly related to the growth mechanisms and preferential dopant incorporation paths of the nanowires. The physical mechanisms leading to the dopant incorporation in the nanowire may be a combination of two extreme cases, which are schematically represented in Fig. 4.7. The first incorporation pathway is the nanowire facets. This is especially relevant in the case where the dopants are not soluble in the droplet and/or where radial growth is non-negligible. Indeed, even for a slight radial growth, the silicon atoms impinging on the nanowire facets can be gradually incorporated during the nanowire growth. If doping should be a consequence of the nanowire radial growth, one would expect a higher number of dopants at the nanowire base and it should decrease monotonically when approaching the nanowire tip. The second incorporation pathway is the Ga droplet at the nanowire tip. In this case, the amount of dopants incorporated in the
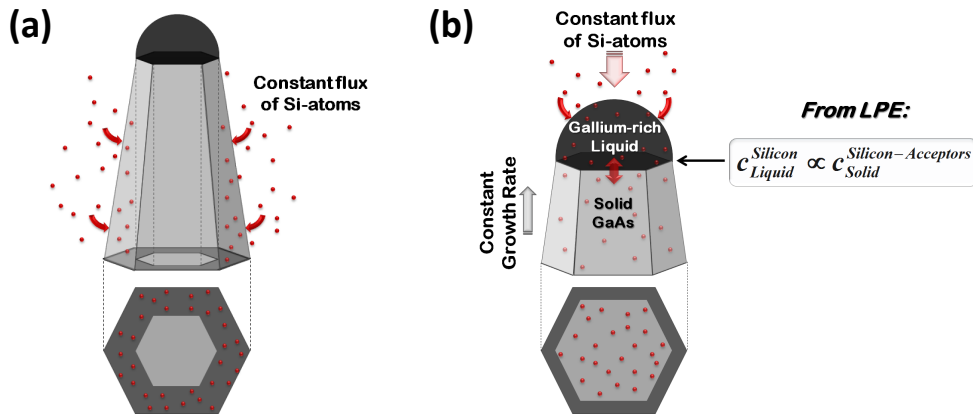
Figure 4.7: Schematics of two extreme doping mechanisms in nanowires: (a) through side facet deposition and (b) through the droplet.

nanowire should be proportional to the concentration in the droplet [50, 88]. The doping concentration in the nanowire should be nearly negligible at the nanowire base and then increase monotonically toward the nanowire tip until the droplet achieves the equilibrium concentration. At first, the possibility of dopant incorporation through the side facets will be considered. The incorporation of silicon through the facets could be the natural consequence of the nonzero radial growth of the nanowires. In the case of gallium-assisted MBE growth of nanowires, the radial growth rate is about a factor of 1000 smaller than the axial [28]. For a 20μm long nanowire, the radial shell exhibits a thickness varying from 50 to 0 nm from the base to the nanowire tip. By taking into account geometrical factors of the flux toward the nanowire facets, the concentration in the shell should be 6 x 10^{19} cm^{-3}. Such doping concentration is consistent with the resistances measured.

For the second dopant incorporation pathway, through the Ga droplet, the Si-Ga phase diagram and liquid phase epitaxy (LPE) data must be taken into account. In an LPE process, growth precursors are incorporated through a liquid-solid interface. Gallium-assisted growth of GaAs nanowires corresponds to an LPE process at the nanoscale. For single donors and acceptors in GaAs, the impurity concentrations in the semiconductor and in the liquid phase are proportional. Carrier concentrations well above 10^{19} cm^{-3} have been obtained [57]. Following the phase diagram, the solubility of Si in Ga is about 1% at 630 °C [89]. Two elements determine if the droplet can be a significant pathway of incorporation, with respect to the side facet deposition: i) the steady state concentration at the droplet, given the growth conditions of silicon flux and nanowire growth rate, and ii) the incubation time for this process. The

incubation time would correspond to the time necessary for the liquid droplet to achieve the steady state concentration of silicon. In a simplified model, the steady state concentration in the nanowire can be calculated taking into account the conditions

$$\frac{dc_{Si}}{dt} = \Gamma_{g \to l} - \Gamma_{l \to s}(c_{Si(l)}) = 0 \tag{4.6}$$

where c_{Si} corresponds to the silicon concentration in the droplet and $\Gamma_{l \to s}(c_{Si(l)})$ and $\Gamma_{g \to l}$ are, respectively, the silicon flux from the gas phase to the droplet and from the droplet to the nanowire. In this equation, the incorporation of silicon by diffusion through the nanowire walls and the desorption of silicon from the droplet is neglected. The silicon concentration in the liquid gallium and in the GaAs nanowire are related via the distribution coefficient k, in the form: $k = c_{Si(s)}/c_{Si(l)}$. The values are well known for the Si-Ga(l)/GaAs(s) system. The distribution coefficient of silicon in the GaAs solid/liquid system at 630 °C is 0.1 for silicon incorporated as an acceptor, and 0.06 as a donor [90]. As a result of simultaneous incorporation of silicon as acceptor and donor, compensation will exist. At 630 °C, the incorporation of Si occurs preferentially in As sites (p-type doping) in a ratio 5:3, given by the different values of k for acceptors and donors [48]. For nanowires growing at 5.5 μm/h and under the silicon flow used in this study, $c_{Si(s)}$ is equal to 1.06 x 10^{18} Si at. cm^{-3}, and $c_{Si(l)}$ = 0.015% in the droplet. The incubation time will correspond to the time necessary for the droplet to achieve $c_{Si(l)}$ = 0.015%, about 3 min for the given conditions. As a consequence, already after 3 min of growth the silicon concentration in the droplet would be high enough to result in a non-negligible precipitation into the nanowire. Given the total growth time of 4 h, this is a nearly negligible nucleation time. The point here is that due to the high compensation, the effective doping should be of 2.6 x 10^{17} cm^{-3}. One should note here that the calculated doping concentration in the core corresponds to an upper boundary and that it is 2 orders of magnitude lower, with respect to what is expected in the most external part of the nanowire. As a consequence, the doping throughout the shell dominates the total conductivity under the+se conditions. Additionally, one should also note that the predominance of shell vs core doping will also depend on the growth rate of the nanowire. The steady increase of resistivity toward the tip of the nanowire is in good agreement with the hypothesis that dopants are mainly effective incorporated on the side facets. Also from the theoretical considerations, elevated effective doping incorporation through the gallium droplet seems extremely unlikely for nanowires grown at the growth rate of 5.5 μm/h, for the given silicon flows.
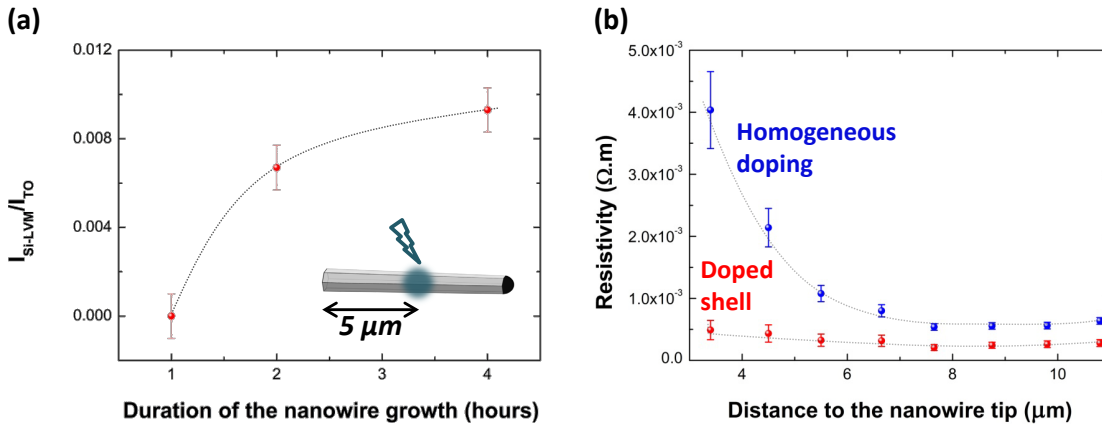
(a)

(b)

Figure 4.8: (a) Change in the Si$_{As}$ concentration with growth time. Measurements have been taken at a distance of 5 μm from the nanowire base. (b) Spatial dependence of the resistivities assuming a homogeneous doping through the entire diameter and in the nanowire shell.

To confirm the picture of having a highly doped shell around a low doped core, a series of nanowires has been grown for one, two and four hours using the same flux of silicon dopants during the growth. Raman spectra have been taken with the probing laser spot positioned at a fixed distance of 5 μm to the base of the nanowires. In Fig. 4.8 (a) the intensity the normalized Si$_{As}$ LMV is plotted as a function of the growth duration. The strong increase in the doping concentration with time clearly indicates the overgrowth of a doped shell on the core with time. The saturation after around four hours may occur when Raman information depth becomes similar to the thickness of the doped shell. In order to find one more element of consistency, the resistance of the nanowire has been scaled with two different geometrical factors: (i) the total nanowire section and (ii) the shell thickness, which can be approximately determined from the diameter tapering along the nanowire axis. In Fig. 4.8 (b), the spatial dependence of the resistivity of a typical nanowire is plotted. On the same graph, the resistivity scaled assuming the two extreme models is plotted. The resistivity is calculated by taking the whole the section of the shell and of the entire nanowire. By assuming that silicon is mainly incorporated in the shell, one obtains a quasi-constant resistivity along the nanowire. The same trend was obtained from all the nanowires measured. In conclusion, for relatively high growth rates, the model of doping through the facets is predominant.

For the sake of completeness, it is important to consider the possibility of doping through the gallium seed in more detail. For this, nanowires have been grown under the same conditions but with a reduced nanowire growth rate. For example, for growth rates of 1 μm/h, the c$_{Si(l)}$ would be 0.083%, leading to a silicon and effective doping concentration to the nanowire
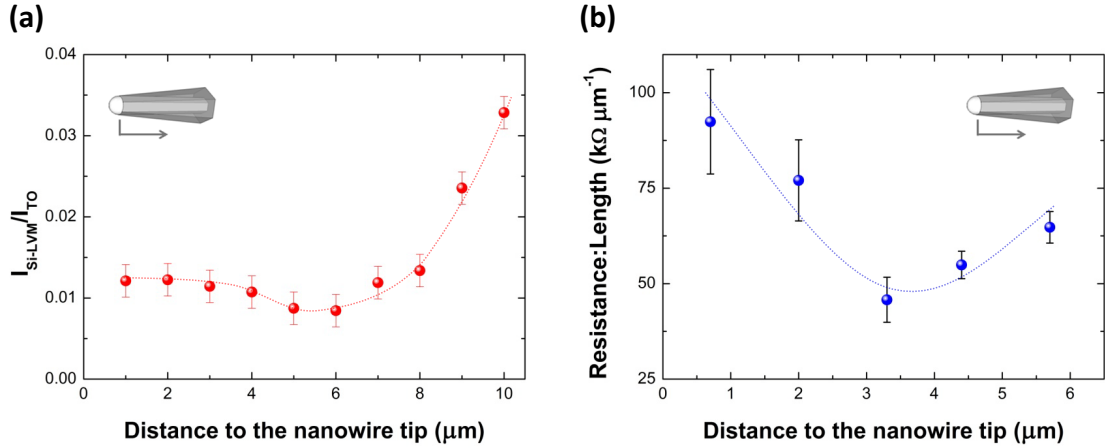
Figure 4.9: (a) Spatial dependence of the intensity ratio between the LVM and TO modes along a typical nanowire grown at 1 μm/h and (b) Resistance per unit length of a nanowire grown under the same conditions.

respectively of 5.8 x 10^{18} and 1.46 x 10^{18} cm^{-3}. This effective doping concentration is just about one order of magnitude below the doping concentration expected in the shell, meaning that it will have a stronger influence in the spatial dependence of the conductivity. Such nanowires should exhibit a different surface doping and resistivity dependence along the nanowire, as dopant incorporation through the droplet should be higher. Nanowires have been grown under identical conditions for a growth time of 8 h, and lowering the nanowire growth rate by a factor of 5.5. The lower growth rate is obtained by lowering the As$_4$ pressure by the same factor. One should note here that lowering the axial growth rate by a factor 5.5 does not result in a lowering of the radial growth rate [28]. Results on the Raman and resistivity mappings are presented in Fig. 4.9. Within the error bars, a much more homogeneous resistivity along the whole nanowire length is observed than in the case of the nanowires grown at 5.5 μm/h. Additionally, the silicon concentration at the nanowire shell as measured by Raman spectroscopy shows a diminution of a factor 3 from the base to the nanowire tip. As Raman spectroscopy of GaAs at 488 nm is only sensitive to the first 40 nm, the Raman measurements indicate the gradient in the thickness of the doped shell along the nanowire and not on the nanowire bulk concentration. In this sense, the Raman spectroscopy measurements are consistent with the existence of shell doping (through epitaxial growth on the facets). However, the spatial dependence of the resistivity is contradictory with a model that only considers incorporation of dopants through the nanowire facets. Indeed, if the resistivity is approximately constant along the nanowire, the only solution is that dopants are also getting incorporated in the nanowire core in the part closer to the tip. More detailed studies of the conductivity and

silicon concentration as a function of growth conditions are necessary for obtaining more details in the doping mechanisms and are currently in progress. In particular, one should find a method to measure the material grown in the last stages (e.g., for the first type of nanowires 1 h of growth corresponds to 5.5 μm, while for the second this is just 1 μm which is not possible to measure either electrical contacting or by Raman spectroscopy). Moreover, the microstructure of the nanowire should be taken into consideration to account for the small spatial variation of the resistivity. Finally, one has to point out the importance of the concept of distribution coefficient in the case of gallium-assisted growth of GaAs nanowires. Indeed, the different temperature dependence of k for p and n type incorporation of silicon could potentially be used in the future for controllably fabricating doped junctions in nanowires with one single type of dopant. In particular, k is higher for n type than for p type at high temperatures like 750 °C and smaller at temperatures lower than 650 °C. This means that one could potentially obtain an axial p-n and/or a gradient junction by just changing the operating temperature during the growth [83, 91].

4.3 Compensation Mechanism in Silicon-Doped Gallium Arsenide Nanowires

4.3.1 Introduction

In the previous chapter it was found that the silicon acceptor incorporation occurs predominantly through the nanowire side facets. This leads to the formation of a highly p-doped shell on the nanowire core. In the following, the existence of compensation in the shell is demonstrated and the corresponding mechanisms are investigated.

When both Si_{Ga} and Si_{As} are present in the GaAs host lattice, an autocompensation of the free electrons and free holes occurs which effectively reduces the free carrier concentration in the semiconductor. Depending on whether the concentration of Si_{Ga} or Si_{As} prevails in the structure, the overall doping behavior is then n-type or p-type, respectively. The ratio between Si_{Ga} and Si_{As} sites is generally controlled by the growth parameters. For example, when the As_4/Ga flux ratio is reduced and the growth temperature is increased, Si incorporates preferentially in the As sites, giving rise to p-type doping [62, 92, 93]. Also the orientation of the GaAs surface on which the MBE overgrowth occurs is critical for the resulting autocompensation. For example, the autocompensation is much more pronounced when growing n-type thin films on a GaAs (110) surface than in (100) oriented films [62]. However, autocompensation of Si_{Ga} donors and Si_{As} acceptors alone cannot explain the electrical deactivation of up to 93% of the donors observed in n-type films [94]. Therefore, additional factors contributing to the electrical deactivation have to be considered. This might be attributed to the formation of neutral Si-Si next neighbor pairs, Si clusters, or other native defects such as Si-vacancy complexes [95, 19]. In the following, the dopant incorporation is monitored by measuring the local vibrational modes associated with the impurities. From the information on the type and concentration of the dopant impurities the compensation mechanisms and the limitations of p-doping by silicon in GaAs nanowires are elucidated.

4.3.2 Experimental

Catalyst-free p-type GaAs nanowires were prepared by MBE in a Gen II system under the conditions described in the previous chapter. In order to study both the influence of the silicon flux and the arsenic flux on the doping of the nanowires, two sets of samples were prepared with an As_4 partial pressure of 2.7 x 10^{-6} mbar ('high beam flux') and 8.1 x 10^{-7} mbar

('low beam flux'). For each As-flux, samples were grown with a silicon flux of 5.6 x 10^9, 2.2 x 10^{10}, 5.6 x 10^{10}, and 1.6 x 10^{11} at Si/(cm^2 s). Taking into account the nanowire geometry and radial growth rate, this corresponds to a silicon concentration in the shell of 1.4 x 10^{18}, 5.5 x 10^{18}, 1.4 x 10^{19}, and 4 x 10^{19} cm^{-3}. Raman spectra were recorded in backscattering geometry at 90 K using the 488 nm line of an Ar$^+$Kr$^+$ laser for excitation. The laser was focused on the nanowire with a cover glass corrected objective (0.75 NA) with the incident polarization parallel to the nanowire axis. The power of the incident light was 500 μW.

4.3.3   Results and Discussion

Typical Raman spectra of the GaAs nanowires grown with the various silicon fluxes at two different As partial pressures are shown in Fig. 4.10. All the measurements have been taken with the laser spot positioned at a distance of 1 μm from the base. At that point, the doped shell is about 60 nm thick. As the Raman information depth at 488 nm is about 40 nm, the Raman spectra report only about the doping mechanisms in the nanowire shell and not from the core. In all Raman spectra, one can observe a Si$_{As}$ LVM at 396 cm^{-1} that can be attributed to the incorporation of Si into As lattice sites. This mode is a characteristic for the p-type doping [86]. For nanowires grown with a Si-flux larger than 5.6 x 10^9 Si (cm^2 s), an additional mode arises at 393 cm^{-1} that can be assigned to the formation of neutral Si$_{Ga}$-Si$_{As}$ pairs [61]. The intensity of this peak increases as the silicon flux is increased. For the nanowires obtained with the maximum silicon flux, the two peaks associated with the sites Si$_{As}$ and Si$_{Ga}$-Si$_{As}$ have a similar intensity. For a given scattering volume and scattering cross section per impurity, the measured LVM intensity is directly proportional to the impurity concentration [96]. Thus, Raman scattering allows the relative quantitative characterization of the dopant incorporation.

In Fig. 4.11 a, the integrated intensity of the Si$_{As}$ LVM is plotted versus the incident Si-flux during the growth. For a fair comparison of the data, the intensity of the Si$_{As}$ LVM has been normalized to the intensity of the transverse optical GaAs mode, whose intensity is proportional to the volume probed. Interestingly, the Si$_{As}$ LVM intensity increases sub-linear with respect to the total incoming Si-flux. This behavior is a signature of the existence of dopant compensation at higher doping levels. When the availability of arsenic atoms during the growth decreases, the probability for the incorporation of a Si atom on an As site increases. Accordingly, a higher concentration of Si$_{As}$ acceptors is observed for nanowires grown with low As-flux. Now, the increase in the incorporation of Si in As sites and the formation of Si-pairs will be compared. The intensity ratio between the LVM of Si$_{As}$-Si$_{Ga}$ and Si$_{As}$ as a function of
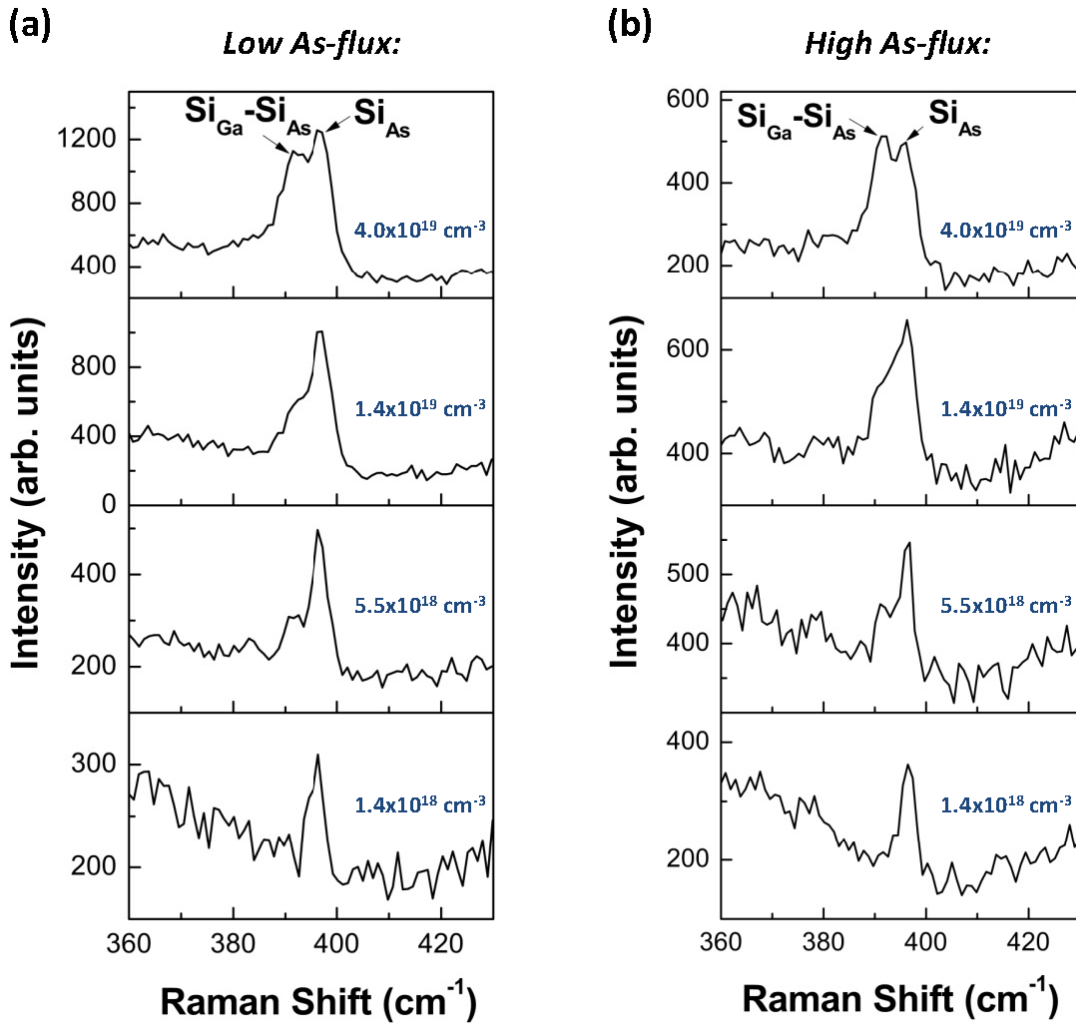
Figure 4.10: Local vibrational mode Raman spectra of the Si-doped GaAs nanowires for different Si concentrations in the shell for nanowires grown with an As-partial pressure of (a) 8.1×10^{-7} mbar (low As-flux) and (b) 2.7×10^{-6} mbar (high As-flux).

the silicon flux is shown in Fig. 4.11 b. In this case, the increase of the mode related to the silicon pairs is quite abrupt and tends to saturate at the highest doping. This is a signature that the compensation occurs in a nonrandom way. The main source of compensation in p-type GaAs:Si is Si atoms incorporated in Ga lattice sites (Si_{Ga}) acting as donors. A reduced screening of the Coulomb interaction between the charged defects has been proposed as the driving mechanism for the formation of the neutral Si-pairs [95].

In the following, an experimental proof of this hypothesis will be given. The main idea of this model is schematically presented in 4.12. Assuming that Si only takes As sites in the GaAs
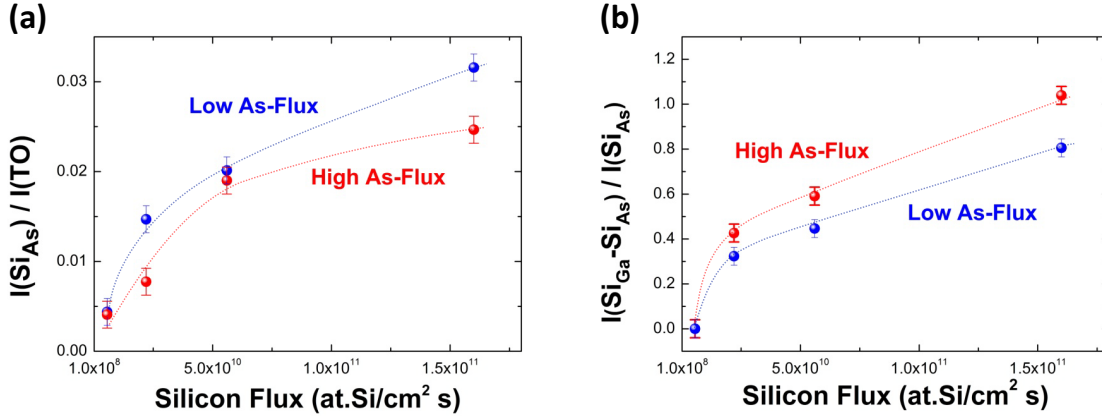
(a)

(b)

Figure 4.11: (a) Schematic drawing of the incorporation of silicon in the nanowire: on the side facets through radial growth and in the core through the droplet. (b) Raman spectra of the Si-doped GaAs nanowires for different Si concentrations in the shell.

lattice, meaning that it exclusively acts as an acceptor, the number of free holes is equal to the number of charged acceptors and the free hole gas perfectly screens the charges centers. As a consequence of the consecutive compensation of Si_{As} acceptors by Si_{Ga} donors, the effective free carrier concentration decreases. Thus, the efficiency of the screening of the electric fields originating from charged atoms is reduced. When the average distance between two Si atoms in the host lattice becomes similar or smaller than the screening length, the Coulomb interaction between the negatively charged Si acceptors and positively charged Si donors leads to the formation of neutral Si-pairs. Such a pair formation occurs during the growth process. For a non-degenerate semiconductor, the characteristic length scale for Coulomb interaction is given by the Debye screening length λ_D:

$$\lambda_D = (\frac{\epsilon_0 \cdot \epsilon \cdot k_B \cdot T}{e^2 \cdot p^*})^{1/2} \tag{4.7}$$

where $\epsilon = 13.1$ is the permittivity of GaAs and p^* is the effective screening density of free carriers. The Debye length as a function of the effective carrier concentration in GaAs at 630 °C is displayed in Fig. 4.13. In the same graph, the average Si-Si distance for the concentrations of the nanowires presented in this work is plotted, in the case where the distribution of dopants is completely random. By comparing the average Si-Si distance with λ_D for the corresponding free carrier concentration, it is possible to deduce if Coulomb interaction between charged

1) No compensation: the hole gas perfectly screens the charged acceptors

2) Compensation: free holes are compensated by free electrons

3) Reduced Debye Screening: screening of the ions by the hole gas less efficient

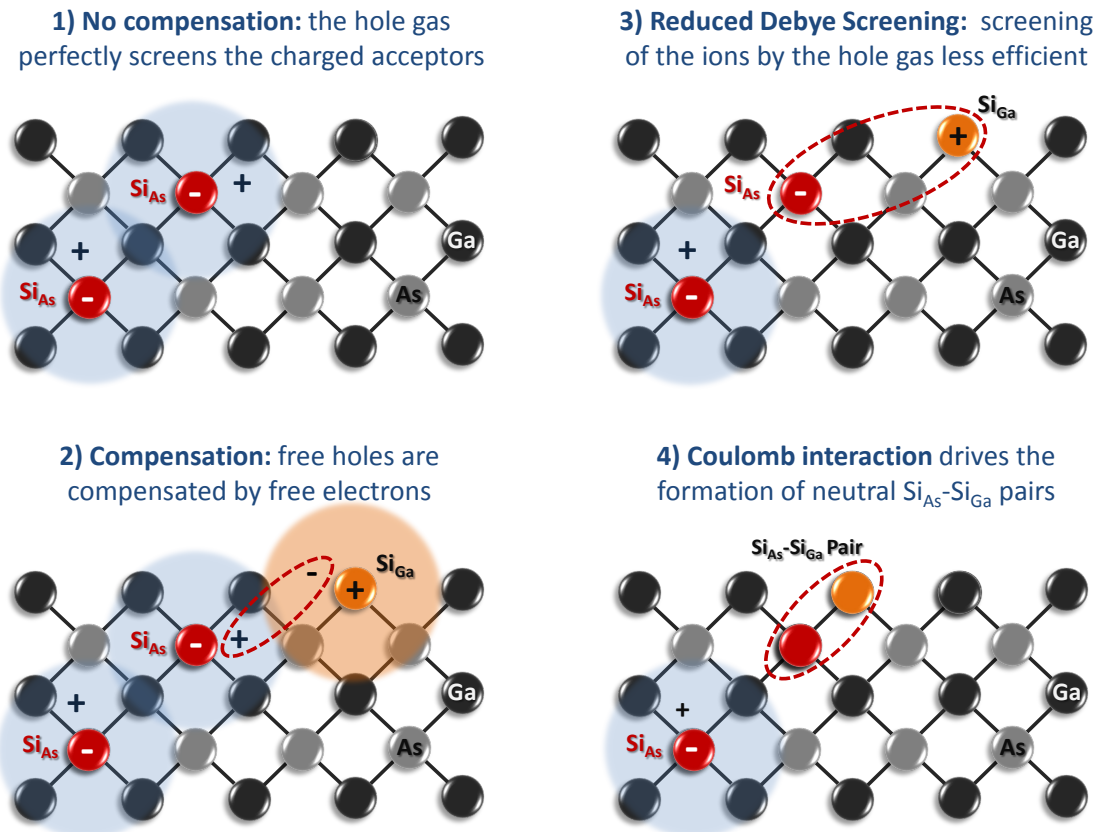**4) Coulomb interaction** drives the formation of neutral Si_{As}-Si_{Ga} pairs

Figure 4.12: The formation of neutral Si-Si pairs at the growing GaAs surface as a consequence of the reduced screening of the Coulomb interaction at high compensation levels is shown schematically.

defects can drive the formation of Si-pairs. Additionally, it is possible to deduce the lower bound of compensation. The average distance between two silicon atoms supposing a random distribution of the dopants for silicon concentrations of 4×10^{19}, 1.4×10^{19}, 5.5×10^{18}, and 1.4×10^{18} cm^{-3} is respectively 2.9, 4.1, 5.7, and 8.9 nm.

Now, looking back at the experimental data in Fig. 4.10, it is clear that a certain threshold value for the Si-pair formation exists that is overstepped when the total Si-concentration is increased from 1.4×10^{18} to 5.5×10^{18} cm^{-3}. At this threshold concentration, the corresponding Si–Si distance crosses over the Debye length λ_D. For a Si-concentration below the threshold, as for the lowest Si-concentration of 1.4×10^{18} cm^{-3}, there is no experimental evidence for Si–Si pair formation. Consequently, λ_D has to be smaller than the average Si–Si distance of 8.9 nm. As one can see in Fig. 4.13, the difference between the total Si-concentration and the effective free carrier concentration corresponding to this upper bound of $\lambda_D =8.9$ nm is
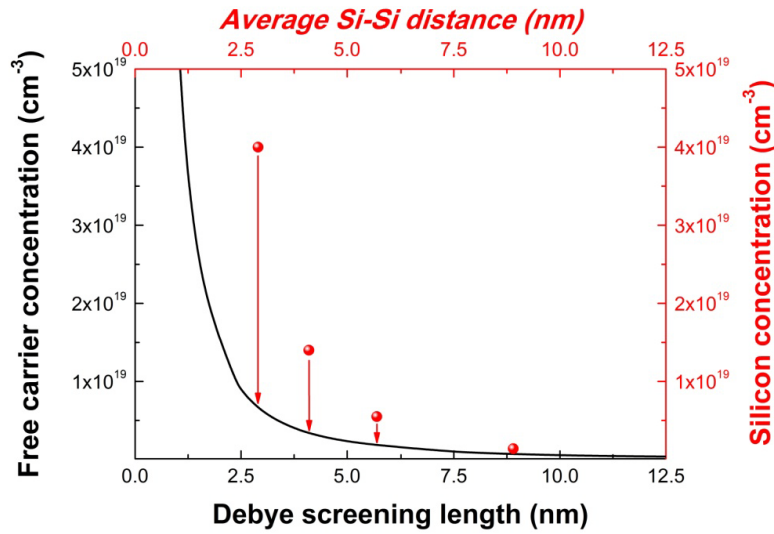
Figure 4.13: The Debye screening length is plotted as a function of the free carrier concentration. In addition, the average distance between Si atoms in the GaAs lattice calculated for the experimentally given total Si concentration in the nanowire shell is shown. The compensation, given by the difference between the total Si concentration and the effective free carrier concentration, is indicated by the arrows.

negligible. Therefore, in excellent accordance with the model of screened Coulomb interaction, compensation effects can be neglected for nanowires grown with the lowest Si-flux. At the same time, one can give an estimate for a free carrier concentration of 1.4 x 10^{18} cm^{-3} in this sample (the contribution of the intrinsic carrier concentration to the total free carrier concentration in GaAs is still negligible at the growth temperature of 903 K). On the other hand, for Si concentrations above the critical threshold value, it is known from the experimental observation of Si-pairs that the screening length is effectively larger than the Si-Si distance. For example, for the sample grown with the highest Si-concentration of 4 x 10^{19} cm^{-3}, the Debye length has to be larger than the Si-Si distance of 2.9 nm. Fig. 4.13 shows that for λ_D 2.9 nm, the effective free carrier concentration is smaller than 6 x 10^{18} cm^{-3}. Therefore, the difference between the total Si-concentration and the effective free carrier concentration is at least 3.4 x 10^{19} cm^{-3} (this difference is denoted by an arrow in Fig. 4.13), corresponding to a minimum compensation of 85% in the nanowires grown with the highest Si-flux. This means that at least 85% of the Si atoms do not contribute to the carrier concentration. Finally, from these considerations, we can also give an upper bound of the free carrier concentration of 6 x 0^{18} cm^{-3} for the nanowire grown with the highest Si flux.

An inherent assumption of the above described model for Si-Si pair formation is an increased
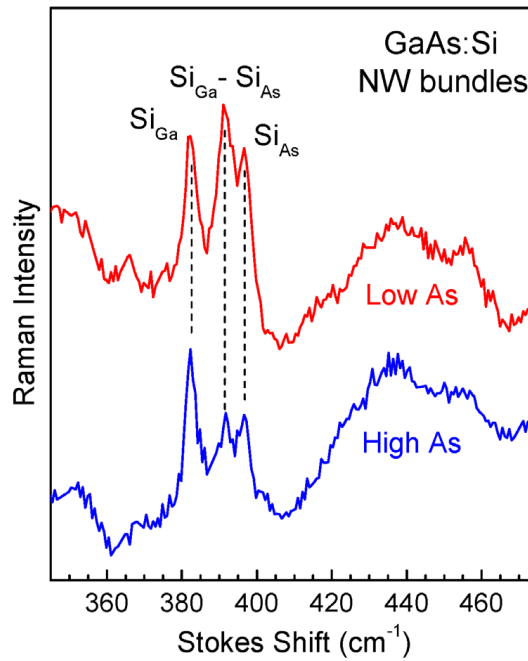
Figure 4.14: LVM of the nanowires grown with low and high As-flux taken with the 413 nm (3.0 eV) line of a Kr^+-ion laser at 77K. Raman scattering by compensating Si_{Ga} donors is resonantly enhanced (the experiment has been performed by Dr. Manfred Ramsteiner at the Paul-Drude Institut Berlin).

incorporation of Si on Ga sites with increasing Si-flux during the growth. As the Raman scattering intensity from local vibrational modes is sensitive to the laser energy used due to resonant enhancement processes, the Si_{Ga}-LVM is not observable with the 488nm laser line. Within a cooperation Raman scattering experiments have been performed using a 413 nm Krypton laser that allows the observation of both Si donors and acceptors. The result is shown in Fig. 4.14. In perfect agreement with the model a high concentration of Si_{Ga} donors compensating the Si_{As} acceptors is observed in the p-type GaAs nanowires with the highest total Si-concentration.

4.4 Assessment of the Carrier Concentration and Mobility in Doped GaAs Nanowires

4.4.1 Introduction

In the following chapter, Raman scattering by coupled LO-phonon-plasmon modes in p-doped and n-doped GaAs nanowires is examined in order to obtain direct information on the concentration and the mobility of the free carriers in the wires. The challenge of this experiment is that Raman scattering from LO phonons is not allowed in backscattering geometry from the {110} side facets of the nanowires. This means that the LO phonon does not appear in the spectrum and therefore also the coupling to the plasma is not observable. However, strong Raman scattering from LO phonons could be obtained by changing the scattering geometry in an unconventional way. Instead of using the classical backscattering geometry, where the scattered light is collected along the same optical path as the incident laser, Raman scattering
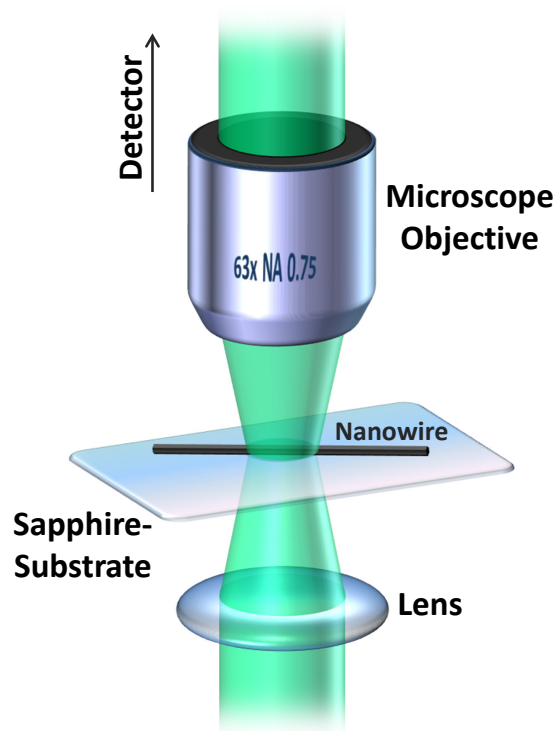

Figure 4.15: Schematic of the forward scattering configuration used for the experiment. The nanowires are dispersed on a transparent sapphire substrate. Laser light is then focused onto the back of the nanowire using a normal lens (f = 5 cm). The transmitted Raman scattered light is then collected by a microscope objective that is collinear aligned with the first lens.

experiments have been performed in a forward scattering or 'transmission' mode. The basic principle of the approach is shown in Fig. 4.15. The incident laser light is focused onto the back of the nanowire with a first achromatic doublet lens. The transmitted Raman scattered light is then collected by a second microscope objective that is aligned collinearly with the first lens.

4.4.2 Experimental

Raman scattering experiments have been performed in forward scattering geometry on p-type and n-type Si-doped GaAs nanowires. The p-type nanowires have been prepared in a Gen II MBE system under the conditions described in the previous chapter. Samples were prepared with an As_4 partial pressure of 8.1 x 10^{-7} mbar and a silicon flux of 5.6 x 10^9, 2.2 x 10^{10}, 5.6 x 10^{10}, and 1.6 x 10^{11} at Si/(cm^2 s). With this a total silicon concentration of 1.4 x 10^{18}, 5.5 x 10^{18}, 1.4 x 10^{19}, and 4 x 10^{19} cm^{-3} is expected. The n-type samples have been grown using a DCA P600 MBE machine. Undoped Si (111) wafers have been used as substrates. The growth has been performed in two steps. First, an undoped GaAs core with a diameter of about 50 nm has been grown using a gallium partial pressure of 7.59 x 10^{-8} Torr, an arsenic partial pressure of 4.1 x 10^{-6} Torr, and a substrate temperature of 640 °C. Then, the growth was continued by overgrowing a 50 nm thick n-doped shell. To do this, the gallium partial pressure has been decreased to 2.24 x 10^{-7} Torr and the substrate temperature was reduced to 465 °C. During the doping, the Si effusion cell was heated with a current between 25 A and 47.5 A.

4.4.3 Results and Discussion

The forward scattering geometry implies severe modifications of the scattering process. This is indicated in Fig. 4.16 where the hexagonal cross section of the nanowire is shown together with the momentum of the incident ($\vec{k}_i$) and scattered ($\vec{k}_s$) light and the momentum $\vec{q}$ that is transfered to the phonon during the scattering process. One can see that the absolute value of the phonon wave vector is maximum for backscattering and minimum in the case of forward scattering. This can be expressed by the following equations [39]:

$$|q_{max}^{backward}| = 2\pi n \times [\frac{1}{\lambda_i} + \frac{1}{\lambda_s}] \qquad |q_{min}^{forward}| = 2\pi n \times [\frac{1}{\lambda_i} - \frac{1}{\lambda_s}] \qquad (4.8)$$
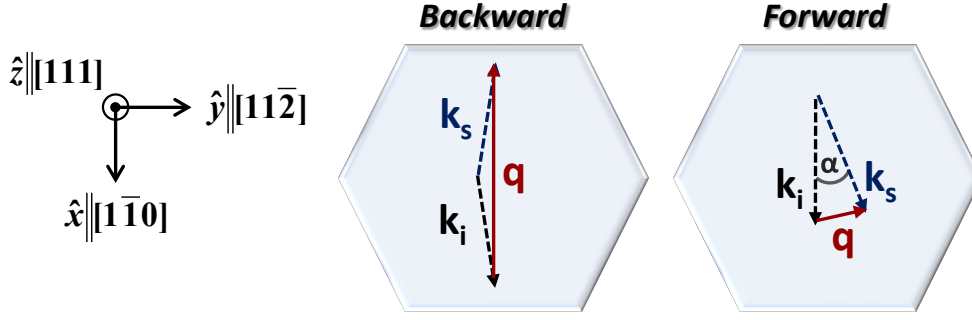
Figure 4.16: Vector diagrams of the momentum transfer in Raman scattering in forward and backward geometry. The hexagonal cross section of the nanowire is indicated in the picture. The orientation of the nanowire is well described using the coordinate system that is specified in the figure.

In the case of GaAs with a refractive index of n = 4.1 at 520.8 nm laser wavelength, a minimum LO phonon wave vector of 7.6×10^3 cm^{-1} is obtained in forward scattering, while the maximum value of the LO phonon wave vector in backward scattering is 9.8×10^5 cm^{-1}. The resulting LO phonon wavelength $\lambda_{LO} = 2\pi/q_{phonon}$ is only 64 nm in the case of backward scattering, but 8.3 μm in the forward geometry. Taking into account the diameter of the nanowire that is about 150 nm, lateral confinement of the LO phonon has to be considered in the forward scattering. This limits the minimum wave vector in x and y directions to $q_{x,y} \approx 2\pi/d$, where d is the diameter of the nanowire.

Besides the absolute value of the phonon wave vector, also the direction of the phonon wave vector changes. From Fig. 4.16 it is obvious that already marginally deviations from the perfect forward scattering geometry ($\alpha \neq 0$) result in a large component of the phonon wave vector in the [11$\bar{2}$] direction, while in backward scattering the phonon propagates in the direction of the incident light. Taking further into account that the phonon is confined in the x and y direction, while it propagates free in the z direction (along the nanowire axis), one can estimate from

Table 4.2: Raman selection rules in GaAs for a phonon wave vector in [11$\bar{2}$] direction for different incident (e_i) and scattered (e_s) polarizations parallel (∥) and perpendicular (⊥) to the nanowire axis.

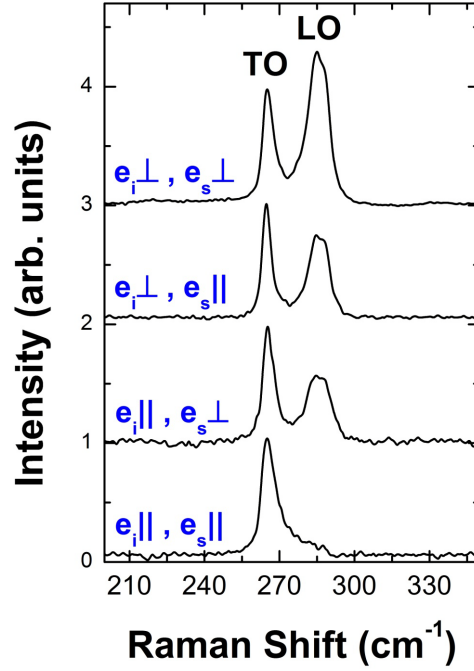| Wave Vector	e_i/e_s	TO	LO
[11$\bar{2}$]	⊥ / ⊥	1/3	2/3
	⊥ / ∥	0	1/3
	∥ / ⊥	0	1/3
	∥ / ∥	4/3	0

Figure 4.17: Raman spectra in forward scattering geometry for different incident (e_i) and scattered (e_s) polarizations parallel ($\parallel$) and perpendicular ($\perp$) to the nanowire axis.

$q_z^2/(q_x^2 + q_y^2 + q_z^2) \approx 0$ that the component of the wave vector transfered into the NW [111] direction is negligible. Consequently, the wave vector transfered to the LO phonon (that is to say the propagation direction of the LO phonon) in forward scattering geometry in the nanowire has components in both the [1$\bar{1}$0] and [11$\bar{2}$] directions. To confirm this, the Raman selection rules have been determined for a phonon wave vector in [11$\bar{2}$] using equation 2.4. The results are shown in table 4.2. Raman scattering from LO phonons is allowed except if both the polarization of the incident and scattered light are chosen parallel to the nanowire axis. The experimental Raman spectra taken in forward scattering geometry from a GaAs nanowire dispersed on a sapphire substrate are shown in Fig. 4.17. The relative intensities of the LO modes are well described by the calculated selection rules for phonon wave vectors in [11$\bar{2}$] directions. The nonzero scattering from TO scattering originates from the contribution of a wave vector component in [1$\bar{1}$0] direction. A slight asymmetry of the TO and LO phonon mode as well as a broadening of the LO phonon mode is observed in Fig. 4.17. This may be related to a certain relaxation of the momentum conservation due to the effect of phonon confinement. The broadening of the LO mode may also be due to a residual intrinsic doping from native defects in the nominal undoped wires.
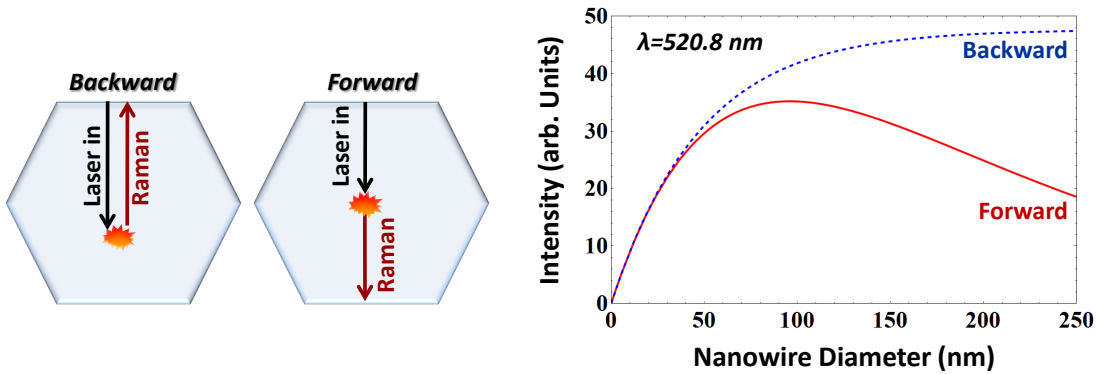
Figure 4.18: Scattering intensity calculated for Raman scattering in forward and backward geometry using a 520.8 nm laser for excitation.

The penetration depth of light with 520.8 nm into GaAs is around 100 nm [87]. Therefore, the question arises why it is possible to detect Raman scattered light in the transmission mode when the nanowire diameter is about 150 nm. Here, both the pathways of the incident laser light and the Raman scattered light through the material have to be considered. The incident light first travels to the point where the Raman scattering event happens, and afterwards the Raman scattered light has to exit the material. These pathways are indicated in Fig. 4.18. In both cases, the intensity of the light is exponentially attenuated along its pathway. The expected Raman scattering intensities for forward and backward scattering assuming a laser wavelength of 520.8 nm are compared in Fig. 4.18. It is interesting to see that even for 150 nm thick nanowires the difference in the scattering intensities is rather small.

In the following, the effect of doping on the LO-phonon scattering will be discussed. The Raman spectra of a series of p-type Si-doped GaAs nanowires taken in forward scattering configuration are shown in Fig. 4.19 a. With increasing free hole concentration a decrease in the LO intensity is observed. Furthermore, the LO mode broadens at higher carrier concentration. Both are unambiguous signs for a plasmon-phonon coupling in the doped nanowire samples. Exemplarily, the spectra of the nanowires with a nominal Si concentration of 5.5×10^{18} cm^{-3} and 1.4×10^{19} cm^{-3} have been fitted to the model described in equation 4.4. The result is shown in Fig. 4.19 b. Here, confinement effects have not been considered. In both cases the fit matches the best for a plasma damping constant Γ_p of 680 cm^{-1} which corresponds to a hole mobility of 36 cm^2/Vs according to equation 4.5 (the phonon damping constant γ was fixed to a value of 5.5 cm^{-1}). This is a low, but reasonable value for the hole mobility in p-type GaAs at room temperature [78]. For the plasma frequencies ω_p, values of 145 cm^{-1} and 270 cm^{-1} are
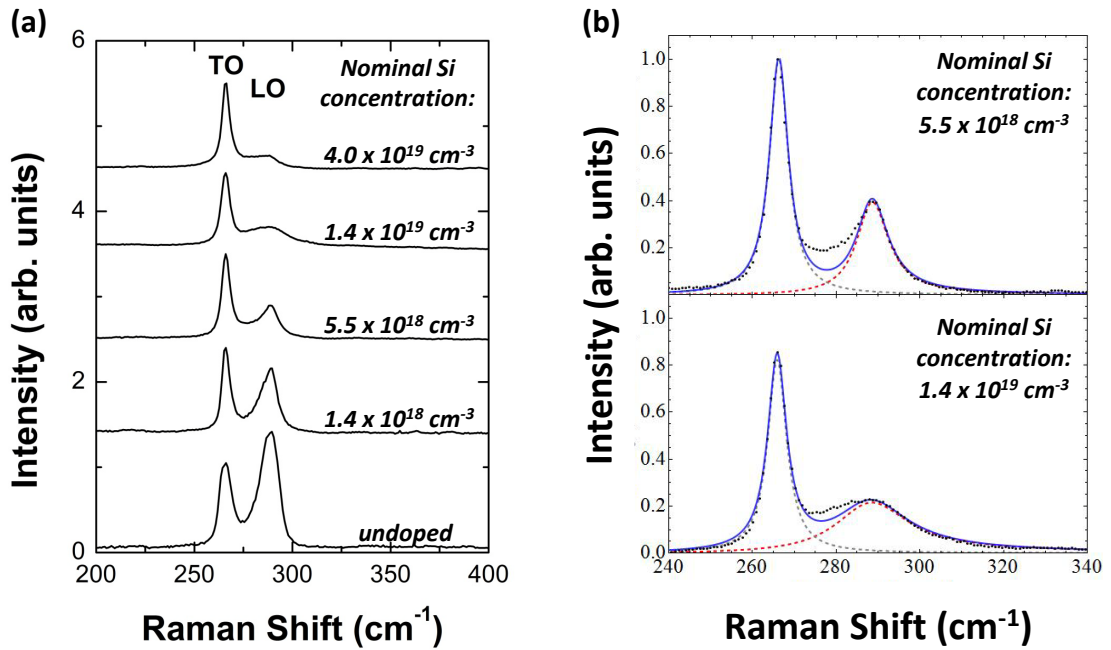
Figure 4.19: (a) Room temperature Raman spectra of p-type GaAs nanowires taken in forward scattering configuration with a 520.8 nm laser. The polarization of the incident laser light was chosen perpendicular to the nanowire axis, the polarizations of the Raman scattered light was not analyzed. Within the different samples the nominal Si concentration varied between 1.4 x 10^{18} cm^{-3} and 4.0 x 10^{19} cm^{-3}. A spectrum of an undoped nanowire is shown as a reference. (b) Fit of the theoretical model to the experimental spectra.

obtained from the fit. They correspond to free hole concentrations of 1.0 x 10^{18} cm^{-3} and 3.6 x 10^{18} cm^{-3} in the sample with a nominal Si concentration 5.5 x 10^{18} cm^{-3} and 1.4 x 10^{19} cm $^{-3}$, respectively. This large deviation of the nominal Si concentration from the actual free carrier concentration is a further proof of the high degree of compensation in these samples that has already been discussed in the previous chapter.

Now, the effect of n-doping on the Raman spectra of the GaAs nanowires will be examined. As explained above, the appearance of two coupled LO-phonon-plasmon modes called ω^+ and ω^- is expected in n-type polar III-V semiconductors with sufficient high mobility. The Raman spectra of the n-type Si-doped GaAs nanowires with various Si concentrations are shown in Fig. 4.20 a. Interestingly, a behavior very similar to the p-type samples is observed. Again, the LO mode intensity decreases and the LO mode broadens with increasing Si dopant concentration. In none of the samples the expected two coupled ω^+ and ω^- modes could be identified. In order to confirm that the doping of the samples is actually n-type, the local vibrational modes have been analyzed. In Fig. 4.20 b the spectrum of the highest doped
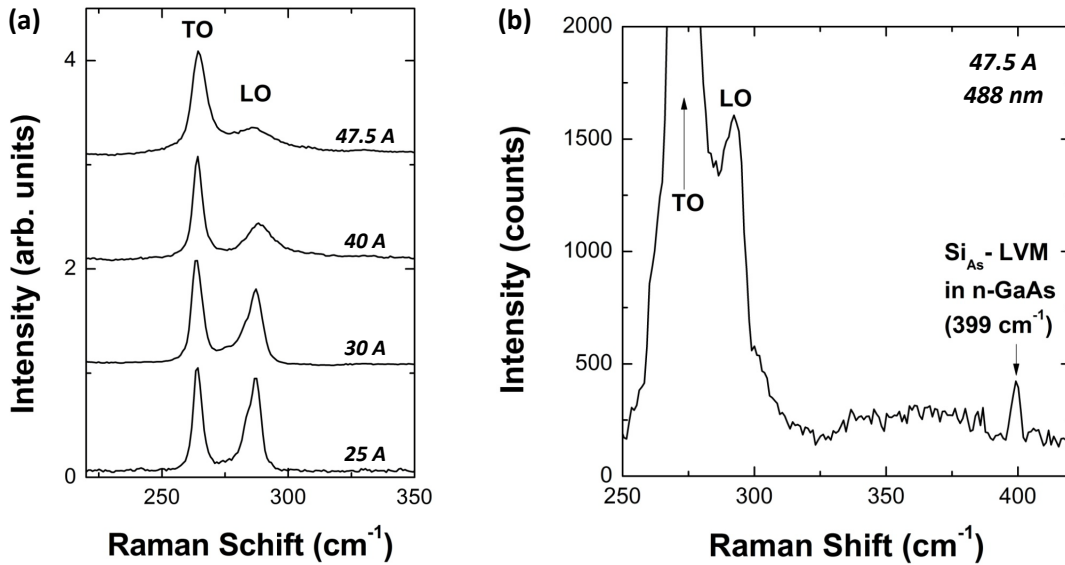
Figure 4.20: (a) Forward scattering Raman spectra of n-type GaAs nanowires with different Si doping for the incident light polarized perpendicular to the nanowire axis and without analysis of the Raman scattered light. A 520.8 nm laser was used. (b) Local vibrational mode spectrum of the 47.5 A sample using a 488 nm laser at 77 K.

sample taken at 77K with a 488 nm laser is shown. A LVM is observed at 399 cm^{-1}, which is the characteristic position of the Si$_{As}$ LVM in n-type GaAs (in the p-type samples shown in the previous chapter, this mode was downshifted to 396 cm^{-1} due to the Fano resonance effect that is characteristic for p-doped GaAs). Based on the fact that the nanowires are actually n-doped, a serious reduction of the electron mobility in the nanowire samples has to be considered in order to explain the experimental spectra. At low electron mobilities, plasma damping has to be taken into account as in the case of p-type samples. This effect has been studied earlier in low-mobility semiconductors such as GaP [97, 98, 99] or GaN [100]. Here it was found that a low mobility electron plasma gives raise to spectral features similar to the ones observed in p-type samples. As shown for example in Fig. 4.21 a, only a rather broad high frequency coupled phonon-plasmon mode at the position of the LO mode is observed in low-mobility n-type GaP samples, while the low-frequency ω^- mode is not detectable in the spectra. In such overdamped electron plasmas, the shape of the coupled LO-phonon-plasma mode is again described by equation 4.4 [97]. Exemplarily, the spectra of the n-type GaAs nanowire grown by heating the Si effusion cell with 40 A has been fitted to the theoretical model. This is shown in Fig. 4.21 b. From the fit a plasma frequency of 156 cm^{-1} and a plasma damping constant of 323 cm^{-1} is obtained. This corresponds to a free electron concentration
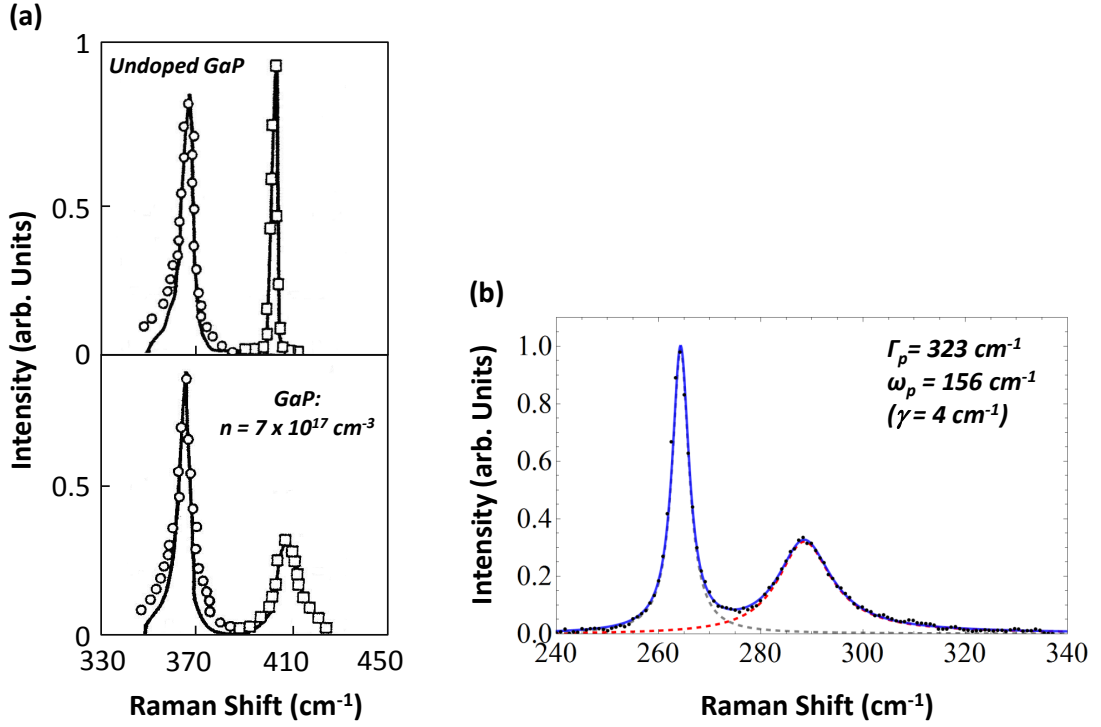
Figure 4.21: (a) Raman spectrum of undoped GaP and low-mobility n-type GaP (adapted from Ref. [97]). (b) Fit to the coupled phonon-plasmon mode observed in a n-type GaAs nanowire grown with 40 A heating current of the Si effusion cell.

of 2×10^{17} cm^3 and a mobility of 432 cm^2/Vs. Here one has to note that the determination of the mobility using Raman spectroscopy usually underestimates the actual Hall mobility by a factor of up to two [80].

There may be several reasons for the relatively low room temperature mobility in the n-type GaAs nanowires. In order to explain the observed behavior, the underlying mechanisms contributing to the phenomenological plasmon damping parameter Γ_p have to be considered in more detail [101]. The first plasmon damping mechanism is related to a collision-less process that is also known as Landau damping. This is a typical bulk phenomenon and cannot explain the low mobility in the case of nanowires. The second category of damping mechanisms consists of collisional or momentum damping that originates from phonon scattering, ionized impurity scattering, and scattering from surfaces. Certainly, scattering from ionized impurities makes an important contribution in materials with a high degree of compensation. However, even in highly compensated epitaxial layers room temperature mobilities of more than 1000 cm^2/Vs are typically reported in the literature [102, 103]. Therefore, one has to assume that scattering at the surface of the nanowires plays a critical role in the degradation of the electron

mobility. The effect of surface scattering in nanowires has been examined earlier by means of magneto-transport measurements. In InAs nanowires for example, it was found that surface scattering contribution may considerably reduce the electron mobility [104].

4.5   Conclusions

The important questions to answer in this chapter were (i) if intentional doping in MBE grown nanowires is possible, (ii) how to tune the growth conditions to control the doping characteristics, (iii) what are the basic mechanisms behind the dopant incorporation, and (iv) which are the limiting factors for the silicon doping in GaAs nanowires. In a first approach, the question of the dopant incorporation pathway has been addressed by combining Raman scattering experiments with electric transport measurements. Two competing doping mechanisms have been outlined: incorporation from the side facets and from the gallium droplet. It was found that the p-doping is governed by the incorporation of Si atoms from the side facets during the radial growth of the nanowire. However, evidence for an incorporation through the liquid gallium droplet was found, even though the doping through this pathway is limited by the relatively low number of Si atoms impinging on the catalyst droplet during the growth.

Based on the knowledge gained on the incorporation process, the efficiency and the fundamental limitations of the doping process have been studied in detail in a second step. By analyzing the local vibrational modes of silicon dopants in the GaAs host lattice, dopant compensation was found as an important factor that can dramatically limit the Si doping efficiency in p-type GaAs nanowires. It could be shown that increasing the Si-flux during the growth only results in a sub-linear increase in the Si_{As} accepter concentration. At the same time the number of neutral Si_{Ga}-Si_{As} pairs strongly increases. It was found that it is the reduced Coulomb screening in the highly compensated nanowire that drives the formation of the Si-pairs. This results in an electrical deactivation of at least 85% of the silicon dopants in the highest doped nanowires. These findings will have to be taken into consideration in the future for the fabrication of optical and electronic devices with Si-doped GaAs nanowires.

Measuring the doping characteristics such as the carrier concentration and the mobility of a single nanowire is a challenging task. Using Raman scattering in forward scattering geometry these important characteristics have been successfully determined. For it, the coupled LO-phonon-plasmon modes have been analyzed. In p-type GaAs nanowires carrier concentrations in the order of 10^{18} cm^{-3} and mobilities of around 40 cm^2/Vs have been

detected. Interestingly, signatures of an overdamped electron plasma have been found in n-type Si doped GaAs nanowires. The corresponding low electron mobilities indicate that surface scattering effects and doping compensation are crucial factors for the performance of future electro-optic nanowire devices.

5 Resonant Raman Scattering in Wurtzite GaAs Nanowires

GaAs nanowires can be grown with segments of the wurtzite and the zinc-blende crystal phase. As the difference in the electronic band structure of these polytypes leads to charge confinement, the engineering of the electronic structure within a single material becomes possible. However, this presupposes an exact knowledge of the band structure in the wurtzite phase. It is demonstrated that resonant Raman scattering is the ideal tool to probe the electronic structure of novel materials. Exemplarily, this technique is used to elucidate the band structure of wurtzite GaAs at the Γ point. Within the experimental uncertainty it is found that the free excitons at the edge of the wurtzite and the zinc-blende band gap exhibit equal energies. For the first time it is shown show that the conduction band minimum in wurtzite GaAs is of Γ_7 symmetry, meaning a small effective mass. Furthermore, evidence for a light-hole−heavy-hole splitting of 103 meV at 10K is found. By fitting the temperature dependence of the crystal-field split-off band of hexagonal wurtzite GaAs to the Varshni equation, a value of is 1.982 eV is extracted for the crystal-field split-off to conduction band transition at 0K.

5.1 Background

5.1.1 Wurtzite/Zincblende Polytypism in GaAs nanowires

Many III-V compounds that have the cubic zinc-blende (ZB) structure in the bulk may adopt the hexagonal wurtzite (WZ) structure when they are grown in the nanowire form. Besides GaAs, other important semiconductors such as GaP, InAs, InP, AlAs, AlP, GaSb, InSb or Si that are stable in the ZB structure may crystallize in the WZ lattice when they are grown in the nanowire form [23, 24]. Typically, this WZ/ZB polytypism is observed in segments that contain a larger density of stacking faults at the tip or the bottom of the nanowire.
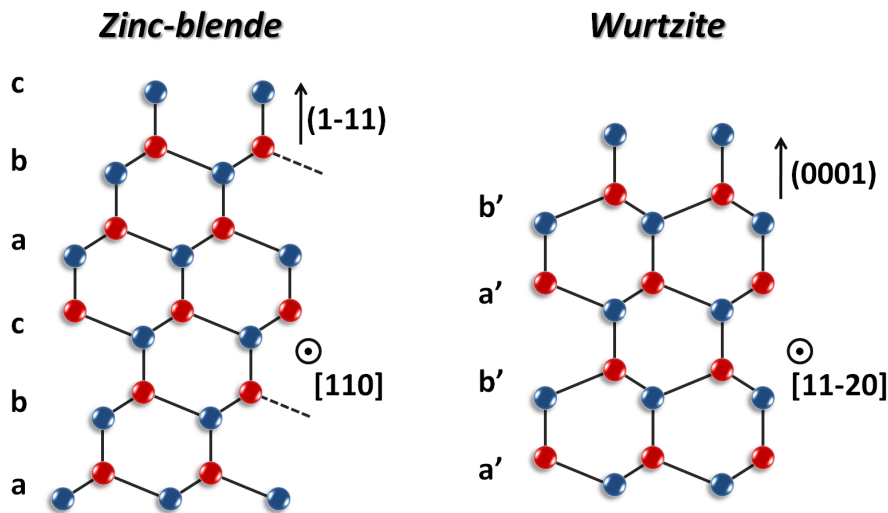
Figure 5.1: Schematic of the crystal structure of GaAs with an ABCABC stacking in the ZB phase and a ABAB stacking of close packing plasnes in the WZ phase.

The crystal structures of ZB and WZ GaAs are very similar. In both the WZ and the ZB lattice the As atoms are tetrahedrally surroundes by four Ga atoms and vice versa. They differ only in the geometry of bonding of their third-nearest neighbours (assuming an ideal c/a ratio of $c/a = \sqrt{8/3} \approx 1.633$ in the WZ structure). Looking along the nanowire axis, the structure is made up of a stacking of (111) close packing planes in the case of ZB, or by stacked (0001) close packing planes in the WZ phase. The relationship between ZB and WZ is a change in stacking sequence of the atomic planes. As shown in Fig. 5.1, ZB is a stacking of ABCABC parallel to the close packing plane (along the ZB <111> direction), while WZ corresponds to a stacking of ABABAB along the [0001] c-axis. Therefore, a rotational twin (a 180° rotation around the growth axis) in ZB can be interpreted as a monolayer thick wurtzite segment. Two

consecutive twins create an atomic stacking corresponding to two wurtzite unit cells and so on. Structural parameters of the GaAs wurtzite phase obtained by powder diffracion are $a = 3.989$Å, $c = 6.564$Å, corresponding to a c/a ratio of 1.6455 [105]. These values slightly deviate from the corresponding ZB lattice parameter, which are $c_{(111)} = 6.528$Å, $a_{(110)} = 3.997$Å, resulting in strain in WZ/ZB heterostructures [37].

The occurrence of the WZ structure in GaAs nanowires has not been explained satisfactorily in a manner that can be applied to all growth methods and conditions. It was found that the abundance of the WZ phase strongly depends on the growth conditions like the growth temperature, the nanowire diameter, or the doping level [106, 107, 108]. For example, the WZ phase is more likely to be observed in case of small nanowire diameters. The smaller surface energy in WZ compared to the ZB structure may explain this diameter dependence [109, 110]. Furthermore, the supply of Ga and As atoms during the growth is critical for the WZ formation. In gold catalyzed GaAs nanowires, a high supersaturation of arsenic or gallium in the liquid catalyst droplet triggers the formation of the WZ phase [111, 112]. In Ga-catalyzed GaAs nanowires, the V/III ratio during the growth playes an important role [31]. For example, when reducing the As-flux with respect to the Ga-flux, a preferential formation of the WZ phase is typically observed. Recently, it has been pointed out theoretically that the effective V/III ratio and also the exact values of the fluxes are important parameters for the WZ growth. They determines the morphology of the liquid catalyst droplet (shape, volume, wetting conditions), which in turn plays a critical role in the formation of the WZ structure [113].

5.1.2 Electronic Band Structure in the Wurtzite and Zincblende Phase

With the possibility of a controlled growth of nanowires in the ZB and the WZ structures, a new degree of freedom in the formation of heterostructures has appeared. Instead of changing the material composition, the crystal phase is varied along the nanowire in this new type of heterostructure [114, 115, 116]. The degree of control over the crystal phase can be astonishingly accurate depending on the growth method [107, 106, 117], so that perspectives for new device concepts are exciting the nano-science and nanotechnology community. However, the change in the crystal symmetry from cubic to hexagonal implies several modifications of the electronic band structure of the material that are mostly unexplored until now.

As a consequence of the hexagonal symmetry, it has been shown that the band structure of WZ semiconductors exhibits important differences compared to the band structure of the
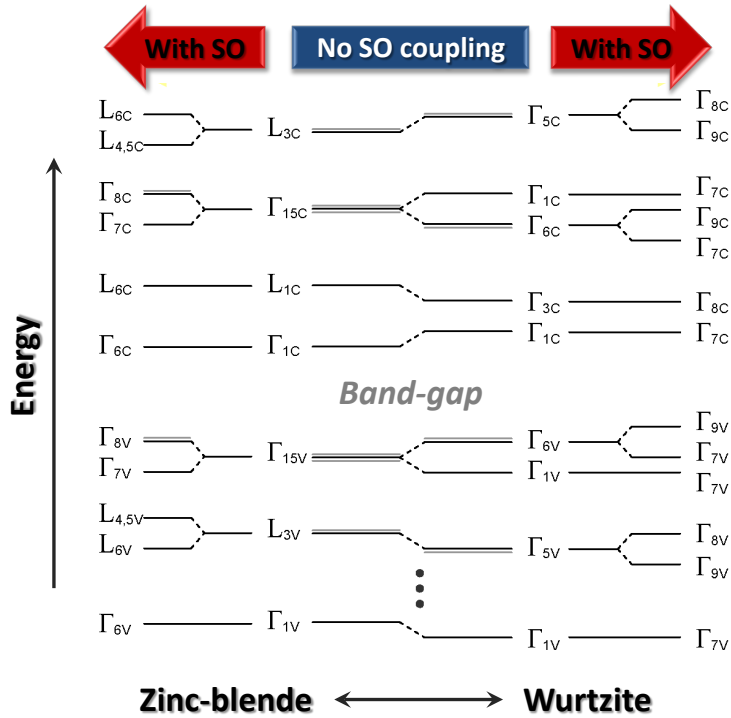
Figure 5.2: Relationships among the zone-center states in the WZ phase and the corresponding Γ and L points in ZB, both with and without spin-orbit coupling (adapted from Ref. [118]).

respective ZB (cubic) counterparts [118]. The general relationship between the zone-center states in the WZ and the ZB structure is shown in Fig. 5.2 [118]. The WZ structure exhibits a unit cell along the (0001) direction double as long as the one of ZB along the equivalent (111) direction. As a consequence, the L point in ZB is zone-folded to the Γ point in WZ. This leads to the existence of a supplementary conduction band in WZ with Γ_8 symmetry close to the ZB-like conduction band with Γ_7 symmetry. In contrast to other III-V semiconductors the energy separation Δ_{CB} between these two conduction bands is expected to be the smallest for the case of wurtzite GaAs. The theoretical predicted values of $\Delta_{CB} = -23$ meV [119], $\Delta_{CB} = +85$ meV [118], or $\Delta_{CB} = +87$ meV [120] are even smaller than the predicted splitting of the two uppermost valence bands.

At the top of the valence band, the hexagonal crystal field in WZ splits the p-like Γ_{15} state of the cubic ZB structure into a doubly degenerate Γ_1 and a fourfold degenerate Γ_6 state. Including also the sin-orbit coupling, the Γ_6 valence band splits into the Γ_9 heavy-hole and the Γ_7 light-hole bands. Further down in energy, the crystal-split-off hole band appears with Γ_7 symmmetry. Consequently, all zone-center valence bands in WZ belong to either Γ_7, Γ_8, or
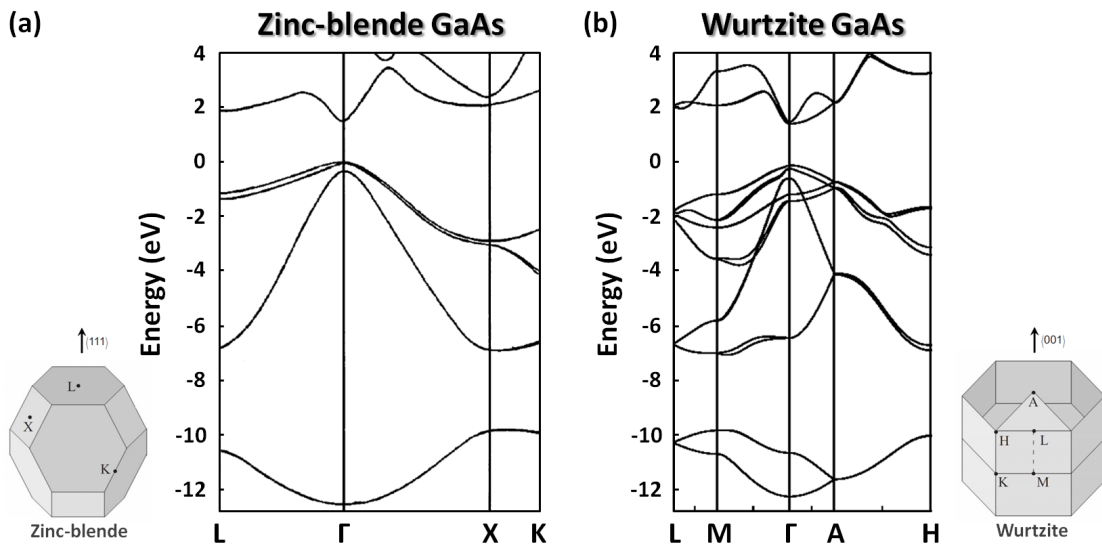
Figure 5.3: Band structure near the Γ point of zinc-blende GaAs (adapted from Ref. [122]). (b) Calculated band structure close to the Γ point of WZ GaAs (adapted from Ref. [118]). The Brillouin zones of the ZB and WZ structure are shown for clarity.

Γ_9 symmetry [118, 121].

The first theoretical studies of the electronic band structure in WZ and ZB date back to 1959 when Birman used a simplified Linear Combination of Atomic Orbitals (LCAO) method to qualitatively study the relationship between the energy bands of compounds in the ZB and WZ structures[123]. Further theoretical work has been performed by Murayama $et\,al.$ [119]. Using a pseudopotential method within the local-density approximation they calculated the band structure of several compounds in the ZB and the WZ phase. For GaAs a slightly larger band gap in the WZ phase than in the ZB structure was calculated. Calculations by Yeh $et\,al.$ and Zanolli $et\,al.$ also showed a larger value for the band gap of WZ GaAs [124, 125]. Recently, De and Pryor determined the WZ GaAs band structure by applying an empirical pseudopotential method including spin-orbit coupling into their calculations. In this case, the result showed a smaller band gap in the WZ GaAs phase with respect to the ZB structure. The band structure of WZ GaAs calculated by De and Pryor is plotted in Fig. 5.3 next to the experimental band structure of ZB GaAs [118, 122]. The predicted values for the band energy and the effective masses parallel and perpendicular to the c-axis are given in table 5.1.

Table 5.1: Zone-center states, calculated energies, and effective masses of WZ GaAs (from Ref. [118])

Band symmetry	Energy (eV)	$m_\perp$	$m_\parallel$
Γ_7 (conduction band)	1.588	0.090	0.082
Γ_8 (conduction band)	1.503	1.050	0.125
Γ_9 (heavy-hole band)	0.000	1.026	0.134
Γ_7 (light-hole band)	-0.120	0.200	0.197
Γ_7 (crystal-field split-off band)	-0.475	0.118	0.434

5.1.3   Resonant Raman Scattering from Longitudinal-Optic Modes in Polar Semiconductors

As already discussed, the Raman effect is usually described as the absorption and subsequent emission of a Raman scattered photon via a virtual intermediate electronic state. However, when the energy of the incident light approaches an interband transition of a semiconductor, real electronic states may mediate the thereby enhanced scattering process. As a consequence, direct information on the electronic band structure can be obtained by finding the conditions leading to resonant enhancement. In polar semiconductors the resonance is particularly important for the exciton-mediated scattering from longitudinal optical (LO) phonons. Here, not only the one-LO-phonon mode is strongly enhanced, but also the higher order multiphonon modes exhibit large enhancements [33]. A prominent example of the multi-phonon scattering from up to nine LO phonons in CdS is shown in Fig. 5.4.
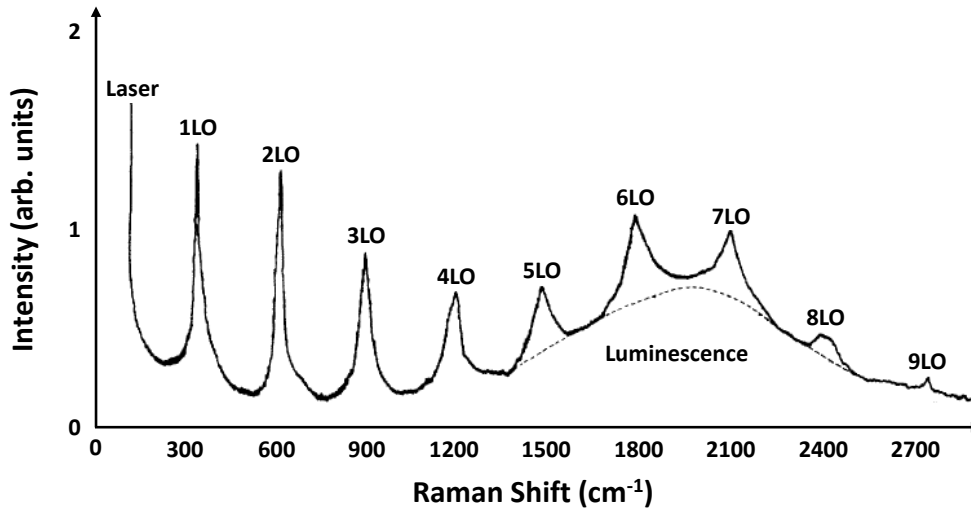

Figure 5.4: (a) Multi-LO phonon Raman spectrum in CdS excited at room temperature with 457 nm laser radiation near resonance with the exciton (adapted from Ref. [126]).
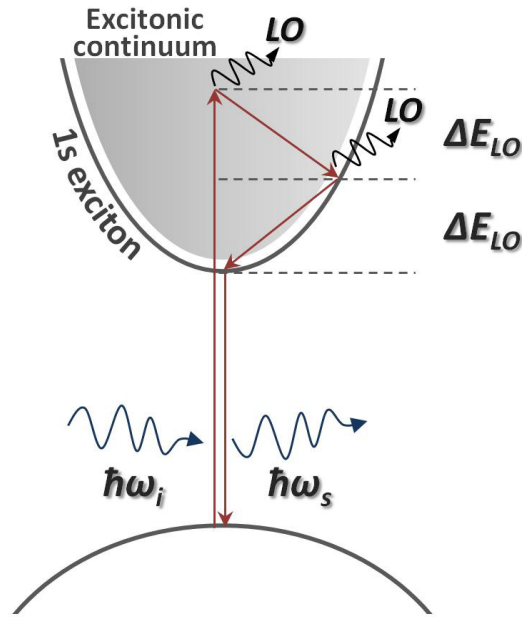
Figure 5.5: Schematic diagram of the resonant Raman scattering from two LO phonons with the 1s exciton as the resonant intermediate state by (i) absorption of a photon and formation of an exciton, (ii) subsequent emission of two LO phonons causes the exciton to change its state, and (iii) return into the ground state of the electronic system by emission of a Raman scattered photon (from Ref. [127]).

In the following, the scattering from 2LO phonons will be discussed in detail. The cascaded LO phonon scattering implies excitonic transitions that are mediated by multiple phonons. Indeed, the second order RRS by two LO phonons due to an iteration of the forbidden inter-band Fröhlich interaction between a phonon and an exciton. A two-LO phonon excitonic scattering model has been proposed by García-Cristóbal $et\,al.$. As shown in Fig. 5.5, the basic idea behind this theory can be described in the following way: when a photon (wave vector $\vec{k}_l$, frequency ω_l) impinges on the crystal, a virtual exciton with a center-of-mass wave-vector $\vec{K} = \vec{k}_l$ is created in the internal state α. In rapid succession, the exciton is relaxed via two intermediate state β and γ, emitting a LO phonon of energy $\hbar\omega_{LO}$ and wave vector $\vec{q}$ at each step. Finally, the exciton recombines under emission of the scattered photon (wave vector $\vec{k}_s$, frequency ω_s). Energy conservation within the global process requires that the energy of the incident photon exactly matches the energy of the edge exciton plus the energy of the two scattered LO phonons:

$$E_{Laser} = E_{Exciton} + E_{2LO} \tag{5.1}$$

The described scattering process is treated in fourth-order perturbation theory (two orders in the crystal-radiation interaction and one additional order in the Fröhlich exciton-lattice interaction for each phonon). In the theoretical model, hydrogenic Wannier excitons are considered as intermediate states in the scattering event. Within the dipole approximation, the quantum mechanical scattering probability amplitude associated with this process is given by:

$$
\begin{aligned}
W_{FI} = \sum_{\alpha\beta\gamma} & \frac{\langle F|\hat{H}_{E-R}|\gamma, \vec{K}=0\rangle \langle \gamma, \vec{K}=0|\hat{H}_{E-L-}|\beta, \vec{K}=-\vec{q}\rangle}{[\hbar\omega_l - \hbar\omega_{2LO} - E_\gamma + i\Gamma_\gamma]} \\
& \times \frac{\langle \beta, \vec{K}=-\vec{q}|\hat{H}_{E-L}|\alpha, \vec{K}=0\rangle \langle \alpha, \vec{K}=0|\hat{H}_{E-R}|I\rangle}{[\hbar\omega_l - \hbar\omega_{LO} - E_\beta + i\Gamma_\beta][\hbar\omega_l - E_\alpha + i\Gamma_\alpha]}
\end{aligned}
\tag{5.2}
$$

Here $E_{\alpha,\beta,\gamma}$ and $\Gamma_{\alpha,\beta,\gamma}$ are the energy and the width of the corresponding states, and $\hbar\omega_l$ is the laser energy. The exciton-radiation and exciton-lattice interaction Hamiltonians are denoted with $\hat{H}_{E-R}$ and $\hat{H}_{E-L}$, respectively. The denominator in equation 5.2 vanishes when the incident or scattered light matches the energy of the real band gap exciton. One can distinguish the following cases: $\hbar\omega_l = E_{Exciton}$ "incoming" resonance, $\hbar\omega_s = \hbar\omega_l - \hbar\omega_{1LO}$ "intermediate" resonance , and $\hbar\omega_s = \hbar\omega_l - \hbar\omega_{2LO}$ "outgoing" resonance. The Raman scattering intensity by 2LO phonons and the scattering amplitude W_{FI} are then related through the equation:

$$I_{2LO} \propto \sum_F |W_{FI}|^2 \tag{5.3}$$

Exemplarily, the scattering efficiency for resonant Raman scattering from 2LO phonons at the $E_0 + \Delta_0$ band gap in ZB GaAs at 100K is shown in Fig. 5.6. The experimental data are very well described by the above explained theory considering excitonic intermediate states. In contrast, when neglecting excitonic effects, the calculated curves do not accord with experimental observations.
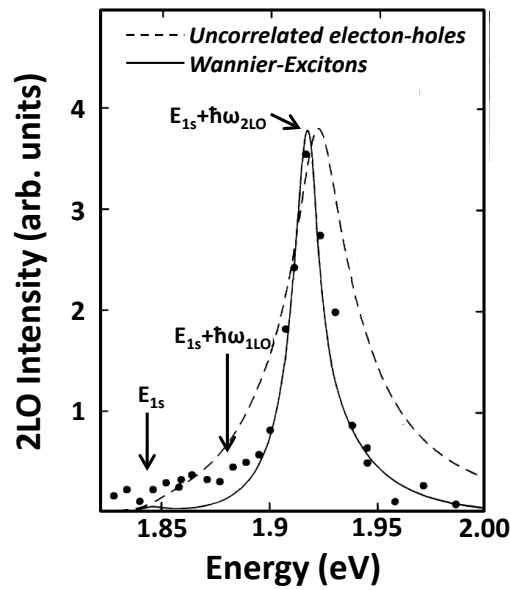
Figure 5.6: Scattering efficiency for 2LO phonon scattering at the $E_0 + \Delta_0$ band gap in ZB GaAs. The solid line is the calculated 2LO resonance profile taking into account excitonic effects. The dashed curve corresponds to theoretical calculations using free electron-hole pairs as intermediate states (adapted from Ref. [127]).

Finally, by tuning the excitation energy, we can use the 2LO resonance profile to find the critical points of the band structure using equation 5.1. Additionally, by measuring the polarization dependence of the resonance, information on the symmetry of the concerned bands can be obtained. Overall, RRS is the ideal technique for revealing the band structure of novel materials or structures, often synthesized in nanoscale sizes.

5.2 Examination of the Electronic Band Structure of Wurtzite GaAs

5.2.1 Introduction

As it has been explained above, the WZ/ZB polytypism observed in the growth of semiconductor nanowires and the change in the electronic band structures that is involved with the variation of the crystal structure gives raise to a multitude of unresolved questions for solid state scientists. Until now, only little experimental work has focused on the details of the electronic band structure of WZ arsenides, phosphides and antimonides. Indeed, several groups reported microphotoluminescence measurements on the direct band gap of the WZ phase of InP [115], InAs [128], and GaAs [120]. But in the presence of stacking faults, the interpretation of the spectra is often hindered by the simultaneous contribution of multiple confined WZ or ZB segments to the PL spectrum, and consequently the experimental results often diverged. For example, for the band gap of WZ GaAs values of 1.54 eV[129], 1.522 eV[130], 1.50 eV[120, 131], and 1.519 eV[132] have been reported. A particularity of the WZ band structure is that a conduction band with Γ_8 symmetry appears close to the ZB-like conduction band with Γ_7 symmetry. Interestingly, the Γ_8 band should exhibit a much larger electron mass than the Γ_7 conduction band [118]. In the case WZ semiconductors would exhibit a Γ_8 conduction band minimum, one would expect the mobility of the material to be reduced significantly. This would have detrimental consequences for the transport properties and its device applicability. The symmetry of the lowest conduction band in WZ GaAs has been discussed controversially in the past few years. Both Γ_8 and Γ_7 minima have been theoretically predicted [118, 119]. Moreover, an experimental proof of the real nature of the conduction band minimum in WZ GaAs is still missing.

The examination of the lower lying valence bands and higher conduction bands using photoluminescence techniques is even more challenging. Here, photoluminescence excitation spectroscopy could shed light on the valence band structure of InP [133, 134], and most recently evidence for the second Γ_8 conduction band in heavily doped InP nanowires could be found in photoluminescence experiments [135]. However, the WZ GaAs the position of the light hole valence band remains unexplored to date. Near the spin-orbit splitting gap $(E_0 + \Delta_0)$ in ZB semiconductors (which corresponds to the gap between the second highest valence band and the lowest conduction band at the Γ point) the theory of resonant Raman scattering has been well established and successfully applied to explore the gap energy, the broadening of the gap, and the electron-phonon interaction in materials like GaAs [40], InP [136], or GaSb

[137]. In semiconductors with the ZB structure, the $E_0 + \Delta_0$ gap arises from the spitting of the degenerate p-like Γ_{15} states of the cubic structure due to the spin-orbit coupling. In the WZ phase both the splin-orbit coupling and the hexagonal crystal-field contribute to the splitting of the degenerate Γ_{15} states. As shown in Fig. 5.7, this results in a crystal-field split-off gap with an energy that is different from the energy of the ZB $E_0 + \Delta_0$ critical point.
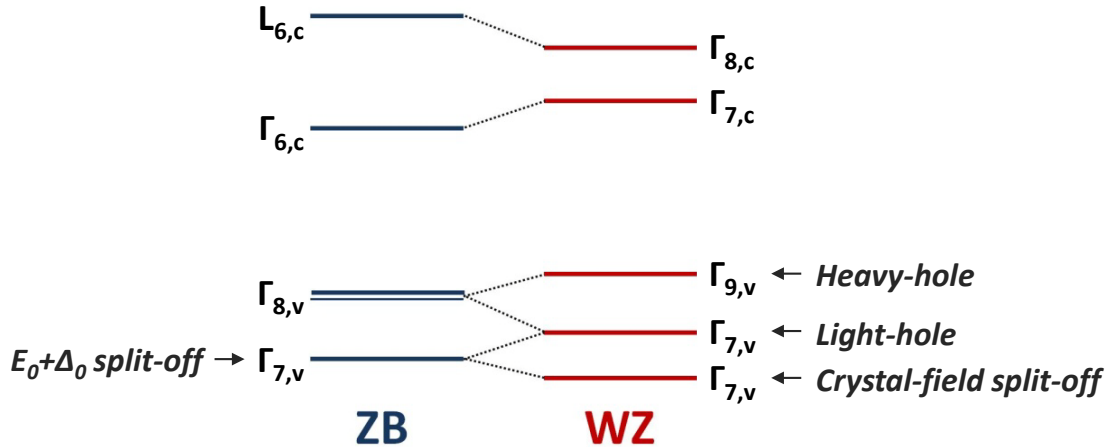

Figure 5.7: Schematic band diagram for ZB and WZ GaAs near the Brillouin zone indicating the $E_0 + \Delta_0$ split-off gap in the ZB structure and the crystal-field split-off critical point in the WZ phase.

In the following, resonant Raman scattering is used order to provide a clear picture of the band structure of WZ GaAs at the Γ point. First, information is gained on the light-hole valence band in WZ GaAs . Then, light is shed on the ordering of the conductions bands and the nature of the lowest conduction band in WZ GaAs. These results will be used in the future for band gap engineering using GaAs polytypes . Finally, the temperature dependence of the transition between the Γ_7 crystal-field split-off valence band and the Γ_7 conduction band is studied and fundamental material parameters like the crystal-field and spin-orbit splitting energies are extraxted

5.2.2 Experimental

For the experiments two different kinds of WZ GaAs nanowires have been used. The first studies of the temperature dependence of the crystal field split-off gap have been performed using gold-catalyzed nanowires. Here, WZ GaAs nanowires were grown by the Au-catalyzed Vapor-liquid-solid method on GaAs $(1\bar{1}1)$B substrates at a growth temperature of $540\,^{\circ}$C under

a As_4 Beam flux of $1.27 \cdot 10^{-6}$ Torr at a Ga rate equivalent to a planar growth of 0.4 Å/s. The growth time was 4 hours. The nucleation and growth followed the gold-catalyzed vapor-liquid-solid mechanism [21]. Details on the growth procedure are described in [138]. After the axial growth of the nanowires the growth parameters were changed to conditions suitable for planar growth and the nanowires were passivated by an epitaxial prismatic shell of AlGaAs/GaAs material [29]. The 2D equivalent amount grown during capping was 60 nm AlGaAs followed by 30 nm GaAs. The total diameter of the nanowires is approximately 85 nm. The high resolution transmission electron microscopy (HRTEM) pictures in Fig. 5.8 demonstate that the structure is 100% wurtzite with a few twin planes at the uppermost tip of the nanowire [120].
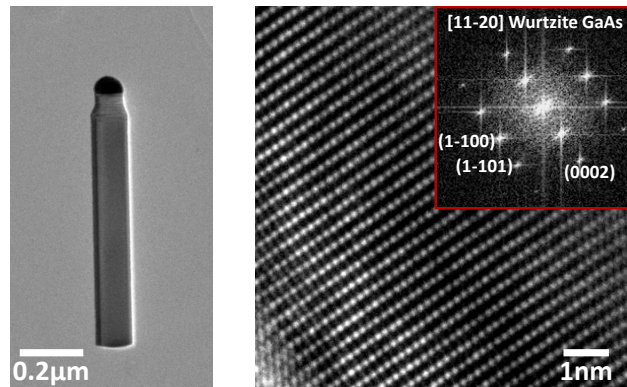

Figure 5.8: HRTEM micrograph of a typical nanowire exhibiting pure WZ GaAs structure. These nanowires have been grown using the gold-catalyzed vapor-liquid-solid mechanism. The power spectrum shown in the inset can be indexed with WZ crystal structure.

For further studies on the fundamental gap and the light-hole band of WZ GaAs nanowires have been grown that contain extended regions of WZ and ZB phases. This allows a direct comparison of the band parameters of the WZ and ZB phases within the same nanowire. The nanowires were grown on the native oxide of an undoped Si (111) wafer in a gallium-assisted process by molecular beam epitaxy using a DCA P600 MBE machine [139, 28]. In order to obtain the sequence of ZB and WZ, we varied the As_4 flux during growth. We first started the growth for one hour under our standard conditions that lead to stacking-fault free ZB GaAs nanowires, that is to say a gallium partial pressure of 6.17×10^{-8} Torr, an arsenic partial pressure of 2×10^{-6} Torr, and a temperature of 630 °C. Then, we consecutively decreased the V/III ratio from 32.4 to 6.9. for 1, 5, and 30 minutes. In between, the growth was continued each time for 30 minutes at the initial V/III ratio. As a result, we obtained a preferential growth of WZ GaAs at the tip of the nanowires [31].
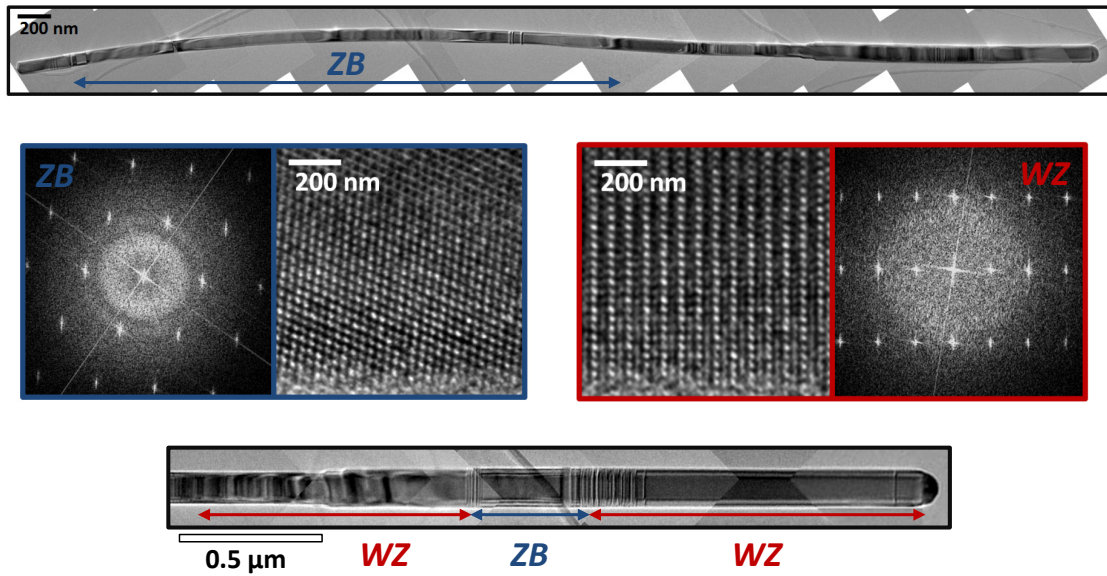
Figure 5.9: HRTEM micrographs of the nanowires grown by the Ga-catalyzed vapor-liquid-solid mechanism. The wires show extended ZB GaAs parts at the base of the wire and long WZ segments at the nanowire tip.

The high resolution transmission electron microscopy (HRTEM) analysis of the nanowires is shown in Fig. 5.9. The first part of the nanowires presents long extensions of ZB structure with low periodicity of twins ($< 1\ \mu\text{m}^{-1}$). Interestingly, the abrupt change in the growth conditions also induces a cascaded increase in the nanowire diameter from 90 nm to 120 nm. This might be due to the increase in the Ga droplet size each time the V/III ratio is decreased. The tip of a nanowire is constituted by stacking fault free segments of pure WZ GaAs with a length of > 1 μm. The WZ structure can be better appreciated and distinguished from the ZB in the detailed HRTEM micrograph insets in Fig. 5.9.

Single nanowire spectroscopy was realized in backscattering geometry on nanowires dispersed on a marked silicon substrate. In the Raman spectroscopy experiments on the crystal-field split-off gap, the nanowires were photoexcited by Ar^+Kr^+ or HeNe lasers with wavelengths respectively 647.1 nm and 632.8 nm. The measurements were realized at a temperature between 10 and 360 K in a liquid helium flow cryostat. Raman scattering experiments on the fundamtnel gap and the light-hole valence band in WZ GaAs were performed as well on single nanowires at 10 K using a tunable titanium-sapphire laser as excitation source. The light was focused on the sample by a diffraction limited spot of < 1 μm with an objective of N.A. = 0.75.

5.2.3 Results and Discussion

A typical Raman spectrum of WZ GaAs taken near the resonance with the polarization of the incident light perpendicular to the hexagonal c-axis (parallel to the nanowire axis) is shown in Fig. 5.10. According to the Raman selection rules, scattering from the E_1 transverse optical (TO) mode, as well as from the non-polar E_2^h mode occurs [37]. Resonant enhancement in the first-order scattering from LO phonons, as well as second-order scattering from two LO phonons is observed as well in the spectrum.
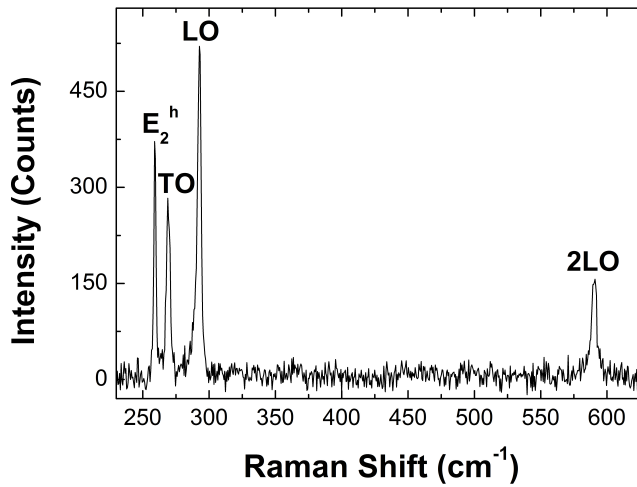
Figure 5.10: Near-resonant micro-Raman spectrum from the WZ part of the gallium-catalyzed GaAs nanowires exhibiting the characteristic E_2^h mode of the WZ structure.

The experiments were performed as follows. Raman spectra were collected as a function of the excitation energy between 1.72 and 1.57 eV for different incident polarizations. The intensity ratio between the LO or 2LO and the TO modes was then obtained as a function of the excitation conditions. Then, the resonant conditions were related to the critical points in the band structure. In the following, the enhancement of the LO and 2LO modes for the different configurations are presented.

The resonance profiles for first and second order scattering from LO phonons in the range of 1.67 to 1.72 eV are shown in Fig. 5.11 a. For both polarizations, parallel and perpendicular to the nanowire axis, a strong outgoing resonance ($E_{Laser} = E_{Exciton} + E_{2LO}$) is observed in the second order scattering from LO phonons with a maximum at 1.6932 eV and a width γ of 14 meV. The outgoing resonance in the first order scattering ($E_{Laser} = E_{Exciton} + E_{LO}$) occurs subsequently with an energy difference of one LO phonon. From the 2LO resonance condition
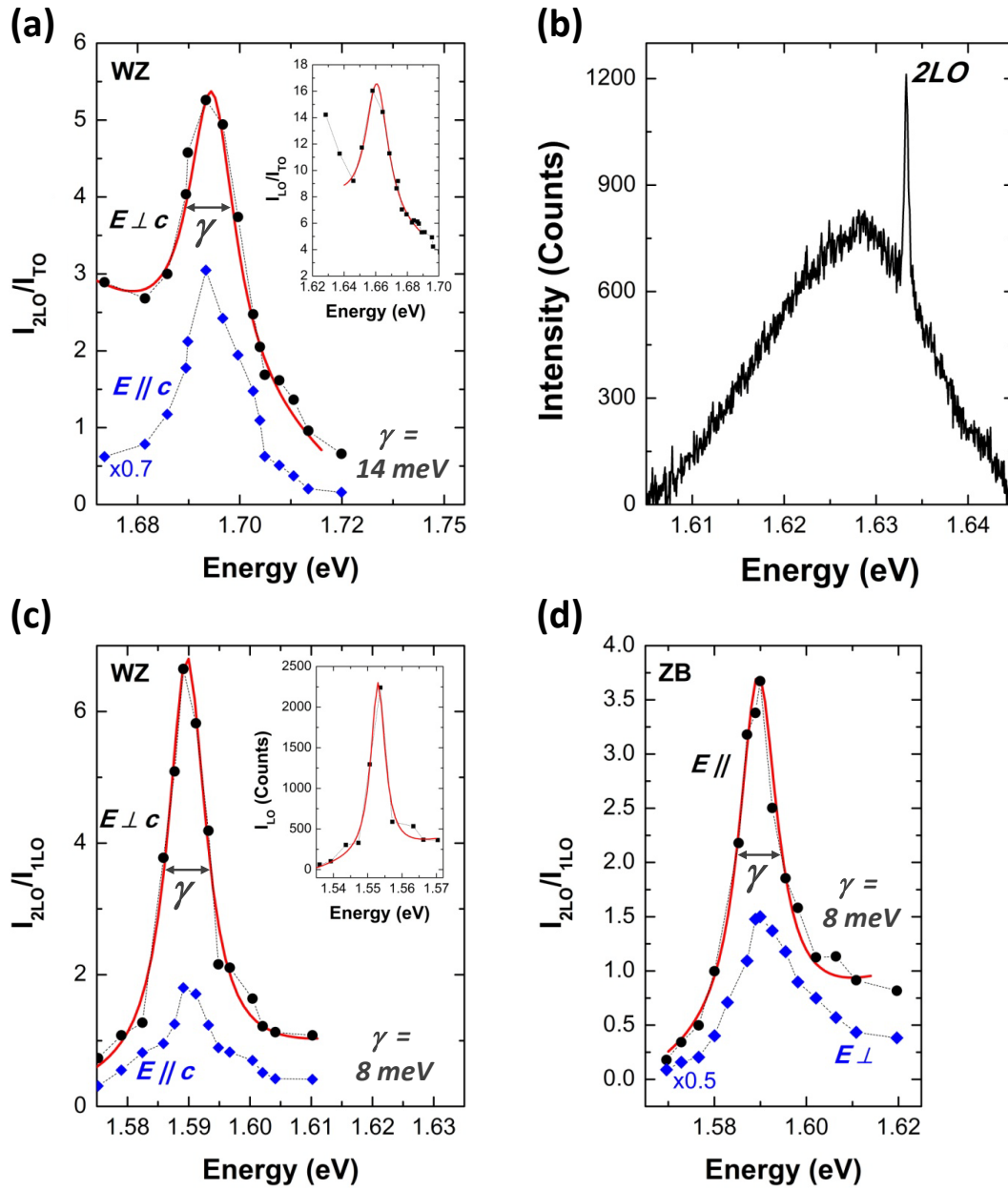
Figure 5.11: (a) 2LO resonance profiles at the light-hole to Γ_7 conduction band transition in WZ GaAs as well as at the band gap of WZ GaAs (c) and ZB GaAs (d) for incident polarizations parallel and perpendicular to the nanowire axis. The photoluminescence at the light-hole to Γ_7 conduction band transition in WZ GaAs is shown in (b). The insets in (a) and (c) show the one LO resonances at the corresponding WZ gaps. The profiles in (a) and (c) in have been scaled for clarity. The spectra have been taken at a temperature of 10 K.

(a)   **(b)**   **(c)**

WZ-light hole   *WZ-band gap*   *ZB-band gap*

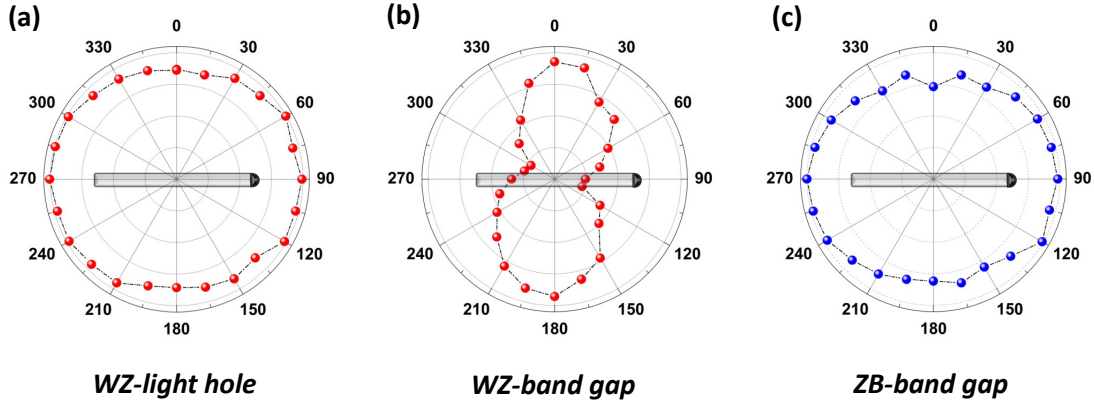Figure 5.12: Dependence of the 2LO resonances on the incident polarization of the light-hole to Γ_7 conduction band transition in WZ GaAs (a) and at the band gap of WZ (b) and ZB (c) GaAs. The orientation of the nanowire with respect to the polarization direction is shown schematically.

$E_{Exciton} = E_{Laser} - E_{2LO}$ we calculate an energy $E_{Exciton}$ of the observed free edge exciton in the WZ GaAs band structure of 1.620 eV at 10K. The photoluminescence at this gap is shown in Fig. 5.11 b.

In the following the band gaps of WZ and ZB GaAs will be discussed. The resonance profiles at the direct gap of WZ GaAs are shown in in Fig. 5.11 c. From a Lorentzian fit the resonance maximum in the second order LO scattering at 1.5897 ± 0.0002 eV is obtained with a width of 8 meV. Subsequently, the resonance in the first order LO scattering occurs with the energy difference of one LO phonon. From equation 5.1 an energy of 1.5165 eV is calculated for the edge exciton at the band gap in WZ GaAs. The 2LO resonance measured in a stacking fault free ZB part of the GaAs nanowire is shown in Fig. 5.11 d. Interestingly, almost exactly the same energy is obtained as for the 2LO resonance in ZB GaAs. A Lorentzian fit results in a maximum at 1.5894 ± 0.0002 eV with a width of 8 meV for ZB GaAs, corresponding to an band edge exciton energy of 1.5162 eV. It is an astonishing result that within the experimental uncertainty the numbers for WZ and ZB GaAs are equal. However, there is an important difference between the resonances observed in WZ and ZB GaAs. In Fig. 5.11 c and d it is clearly seen that the 2LO resonance at the band gap of WZ GaAs predominantly occurs for incident light polarized perpendicular to the hexagonal c-axis, whereas the 2LO resonance in ZB GaAs only weakly depends on the polarization of the incident laser light.

Now, the nature of the interband critical points will be discussed based on the polarization dependence of the Raman resonances. Fig. 5.12 a demonstrates the weak dependence of
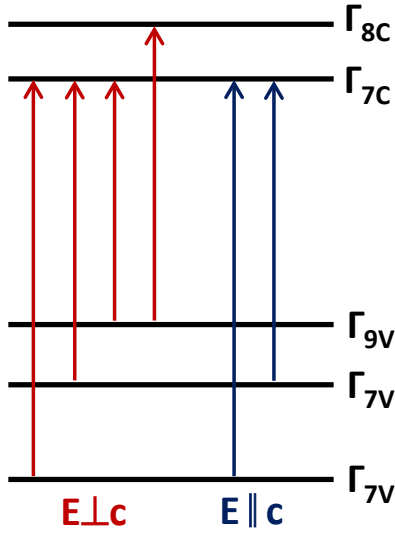
Figure 5.13: Dipole allowed transitions in WZ from Ref. [140].

Table 5.2: Optical selection rules in wurtzite semiconductors adopted from Ref. [39, 140, 141]

Selection rules	Mode	Coupling of states
$E \parallel c$	A_1 (LO)	$\Gamma_7 \to \Gamma_7$
		$\Gamma_7 \to \Gamma_7$
$E \perp x, y$	E_1 (LO)	$\Gamma_9 \to \Gamma_7$
		$\Gamma_9 \to \Gamma_8$

the first 2LO resonance in WZ GaAs at $E_{Exciton}$ = 1.620 eV on the incident polarization. This behavior can be understood from the optical selection rules for WZ crystals [141, 142]. In Fig. 5.13 a the schematic of the band structure at the Γ point of a WZ crystal is shown together with the dipole allowed optical transitions for incident light polarized parallel or perpendicular to the hexagonal c-axis that are also given in table 5.2. For $E \perp c$, scattering from E_1 LO phonons allows coupling of states with symmetry $\Gamma_7 \to \Gamma_7$, $\Gamma_9 \to \Gamma_7$, and $\Gamma_9 \to \Gamma_8$, while for $E \parallel c$ the scattering from A_1 LO phonons only couples states with symmetry $\Gamma_7 \to \Gamma_7$ [39]. Consequently, the unpolarized resonance at 1.620 eV can be unambiguously assigned with a transition from the Γ_7 light-hole valence band to the Γ_7 conduction band. The observed width of 14 meV, which is much greater than the corresponding width at the direct gap, is attributed to lifetime broadening due to the fast $\Gamma_7 \to \Gamma_9$ hole conversion by spontaneous phonon emission. As it can be seen in the measurement shown in Fig. 5.12 c, the resonance at the fundamental gap of ZB GaAs is unpolarized as expected for an optical transition from the degenerate Γ_8 valence band to the Γ_6 conduction band in crystals with ZB symmetry [116]. In contrast, the resonance at the band gap in WZ GaAs is clearly polarized perpendicular to the hexagonal c-axis in Fig. 5.12 b. In this case, both the allowed $\Gamma_9 \to \Gamma_7$ and the $\Gamma_9 \to \Gamma_8$ transitions from the topmost heavy-hole valence band to the Γ_7 or Γ_8 conduction band have to be considered. In the following we will explain why only one of these two allowed transitions-can be observed in the RRS experiment, and how we can identify the nature of the observed transition.
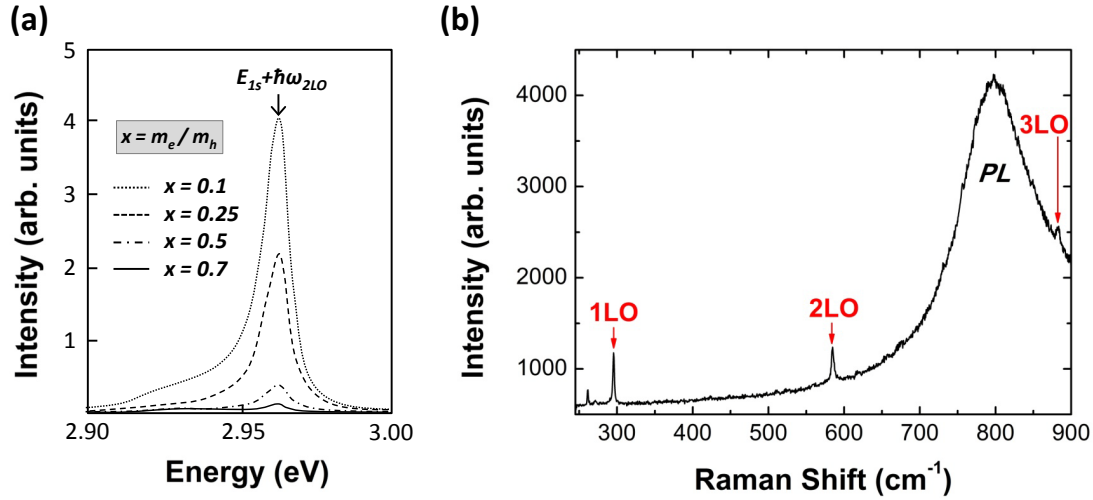
(a)

(b)

Figure 5.14: (a) Theoretical dependence of the 2LO scattering intensity on the ratio of the effective electron to hole mass $x = m_e/m_h$ calculated exemplarily for GaP (from Ref. [127]). (b) Multi-LO phonon Raman spectrum of the WZ GaAs nanowires taken near resonance at 10K showing a monotonic decreases in scattering intensity with increasing LO-phonon order. The spectrum also shows the photoluminescence at the band gap of WZ GaAs.

The most important question concerning the band structure of WZ GaAs is the symmetry of the lowest conduction band, as this will determine if the effective mass is extremely large or not. Based on symmetry considerations, the lowest conduction band should have Γ_8 symmetry provided that the band gap of the WZ phase is smaller than the ZB gap [124, 118]. Our measurements are consistent with an equal or marginally higher band gap. Now, two questions remain to be answered: (i) considering that both transitions from the topmost heavy-hole valence band to the Γ_7 or Γ_8 conduction bands are optically allowed, why do we observe a unique transition, and (ii) what transition do the experiments correspond to? Several experimental and theoretical arguments are consistent with the picture of a Γ_7 conduction band minimum. First, strong resonances with transitions to the Γ_7 conduction band have been demonstrated experimentally for both the crystal-field split-off and the light-hole valence bands. Then, there is theoretical evidence that the interaction between the Γ states of WZ which do correspond to original ZB Γ points and those which do not is rather small [143]. Following this model, one would expect a rather weak resonance. Additionally, one should take into account the value of the expected effective mass of the bands. The effective mass of the contributing bands is crucial for the intensity of the resonant 2LO scattering. When the electrons and holes have similar masses, the theoretically predicted 2LO scattering efficiency decreases in an important manner [127]. This dramatic decrease of the 2LO scattering efficiency as a

function of the effective electron/hole mass ratio $x = m_e/m_h$ is exemplarily shown in Fig. 5.14 a for GaP. Furthermore, the multiphonon resonant Raman spectra of semiconductors with $m_e \approx m_h$ exhibit a characteristic intensity alternation in which the even numbered LO lines are stronger than the odd-numbered lines. This phenomenon has been observed in InI and InBr, both exhibiting similar effective hole and electron mass [144, 145]. On the contrary, for polar semiconductors with $m_e \ll m_h$ the intensity of the multi-LO-phonon scattered light decreases monotonically with increasing order, according to what we observed for WZ GaAs in 5.14 b [146]. In the case of WZ GaAs, the effective mass of the electrons in the Γ_7 conductions band is much lower than the effective hole mass in the heavy-hole valence band. However, the electron and hole effective masses are extremely similar in the case of a heavy-hole band to Γ_8 conduction band transition [118]. As a consequence, we have to assign the strong 2LO resonance at the band gap of WZ GaAs to the transition from the heavy-hole valence band to a conduction band minimum with low effective electron mass, which is the conduction band with Γ_7 symmetry.

In the second part of the work on the electronic band structure in WZ GaAs, resonant Raman scattering experiments have been performed in order to determine the energy of the transition between the split-off valence and the conduction band. Unfortunately, the energy of the crystal-field split-off critical point of WZ GaAs is out of the tuning-range of the Ti-Sapphire laser. Therefore, an alternative approach is used where the energy gap is tuned with respect to fixed laser lines by varying the temperature. Another method to tune the band gap would be the application of pressure [40]. The excitation wavelengths used were 632.8 and 647.1 nm. The temperature was varied between 10 and 360 K.

Raman spectra of the WZ GaAs obtained in polarized configuration with the incident and detected polarization parallel to the c-axis (corresponding to $x(z,z)\bar{x}$ in Porto notation), which lies along the nanowire axis, are shown in Fig. 5.15. The spectra are plotted under non-resonant and resonant conditions, the difference being the intensity of the LO and 2LO peaks. Under non-resonant conditions, only the allowed A_1(TO) mode at ~270 cm^{-1} is observed. Under resonant conditions, not only the intensity of the dipole-forbidden A_1(LO) mode at ~290 cm^{-1} increases significantly but also the second order Raman scattering by two A_1(LO) phonons at ~580 cm^{-1} is strongly enhanced [147].

The intensity of the LO and 2LO peaks normalized to the intensity of the TO mode as a function of temperature for the excitation at 632.8 and 647.1 nm are shown respectively in Fig. 5.18 a and b. The resonance profile of the LO phonon scattering shows a single maximum under outgoing
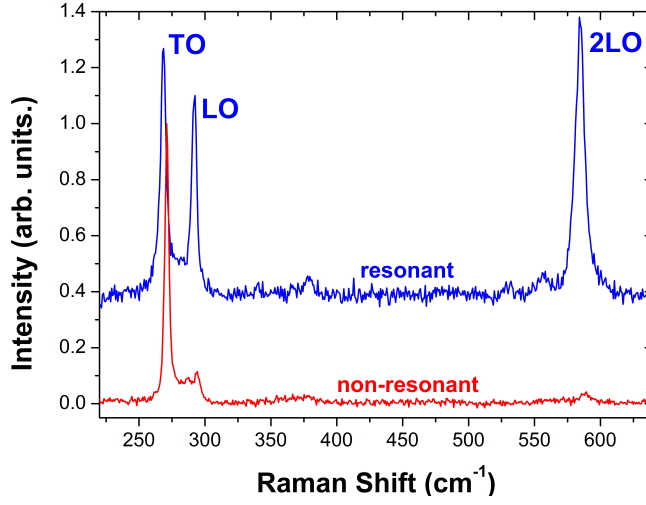
Figure 5.15: Raman spectra of individual gold-catalyzed wurtzite GaAs nanowires taken with the incident light polarization parallel to the hexagonal c-axis at LO/2LO resonance and out of resonance.

resonance, where the scattered light exactly matches a gap of the electronic band structure. The 2LO phonon scattering reveals a strong outgoing resonance ($E_{Laser} = E_c + \hbar\omega_{2LO}$) as well as a weaker intermediate resonance ($E_{Laser} = E_c + \hbar\omega_{LO}$). No incoming resonance is observed neither for the LO nor the 2LO scattering. This behavior has also been observed for zinc-blende GaAs [40]. For the excitation at 632.8 nm, the strongest resonance of the LO and 2LO peaks respectively is observed at 197 and 255 K. For the excitation at 647.1 nm, it occurs at 282 and 327 K. For these temperatures, the energy of the critical point E_c is then calculated:

$$E_c + \hbar\omega_{Ph} = hc/\lambda \tag{5.4}$$

where ω_{Ph} corresponds to the frequency of the phonons (LO or 2LO) and λ is the excitation wavelength. For the temperatures of 197, 255, 282, and 327 K, under which the resonances occur, critical energies of 1.925, 1.889, 1.882, and 1.846 eV are obtained respectively. These points are reported in Fig. 5.15 d. Limitations in the available laser wavelengths do not allow to obtain the energy of this transition at lower temperatures. Nevertheless, the direct luminescence from the recombination between the two resonant levels could be observed at low temperatures. Due to the very few non occupied states in the CH split-off band, such a transition is extremely weak. Luminescence of this transition has been obtained for an incident polarization parallel to the hexagonal c-axis at temperatures between 10 and 40 K by exciting with 568.2 nm and a power of 50 μW. The acquisition time was 30 min, which is between
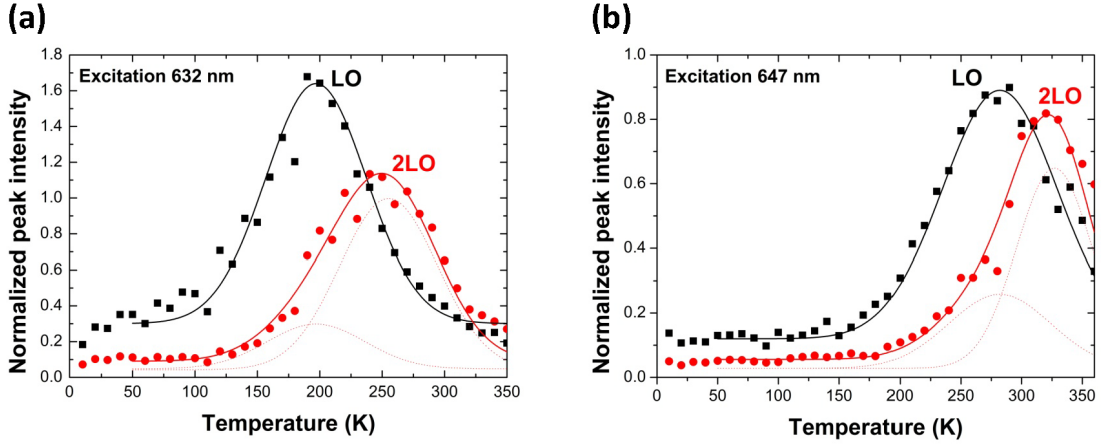
Figure 5.16: (a) and (b) show LO and 2LO resonance profiles for 632.8 nm and 647.1 nm excitation. The LO phonon scattering exhibits a single maximum under outgoing resonance. The 2LO resonance profile consists of a strong outgoing resonance ($E_{Laser} = E_c + \hbar\omega_{2LO}$) and a weaker intermediate resonance ($E_{Laser} = E_c + \hbar\omega_{LO}$).

three and four orders of magnitude longer than our typical luminescence experiments in our nanowires for equivalent excitation powers. The spectra are shown in the inset of Fig. 5.15 d. At temperatures of 10, 20 and 40 K we observe respectively PL centered at 1.982, 1.981, and 1.976 eV. With this, the curve of the temperature dependence can be completed at low temperatures.

The temperature dependent variation of the band gap energy can be commonly given in terms of the α and β coefficients of the Varshni equation:[148]

$$E_c(T) = E_c(0) - \frac{\alpha T^2}{T + \beta} \tag{5.5}$$

Least-squares fitting to the experimental data, the result is shown in Fig. 5.15d, gives the fitting parameters α and β as $6.9 \cdot 10^{-4}$ eV/K and 245.8 K, respectively. For $T = 0$ K we find a gap energy of $E_c(0) = 1.982$ eV.

The nature of the extrapolated interband critical point $E_c(T = 0) = 1.982$ eV in wurtzite GaAs is discussed in the following. One should point out that the direct values are reported and that quantum confinement is not considered. The quantum confinement for the fundamental transition in these nanowires should be in the order of ~15 meV [120]. In zinc-blende GaAs, the interband transition from the spin-orbit-split valence band to the lowest conduction band at the Γ point $E_0 + \Delta_0$ is found at 1.851 eV [149] for $T = 0$ K. Likewise, the observed
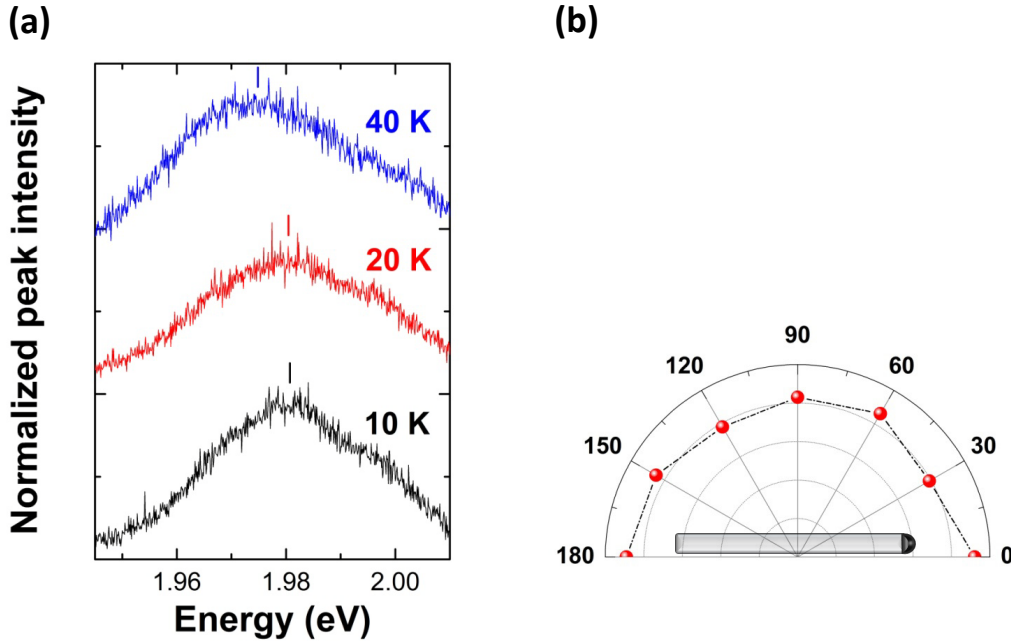
(a)

(b)

Figure 5.17: Photoluminescence spectra showing the weak emission at the crystal-field split-off gap in WZ GaAs at temperatures of 10K, 20K, and 40K. The polarization of the incident light was chosen parallel to the hexagonal c-axis.

energy gap in wurtzite GaAs is attributed to a transition from the crystal-field split-off valence band to one of the lowest energy conduction bands at the Γ point of the Brillouin zone. For the discussion, we need to come back to Fig. 5.7. The crystal-field split-off valence band has a Γ_7 symmetry. In the conduction band there is an important difference with respect to zinc-blende. There is one first minimum labeled Γ_8, which originates from the zone-folded L-valleys of zinc-blende GaAs. This band is separated by a small energy fraction Δ_{CB} from a close lying conduction band with Γ_7 symmetry. According to the selection rules in materials with hexagonal wurtzite structure, optical transitions from the Γ_{7v} valence band to the Γ_{7c} conduction band are dipole allowed. Transitions from the Γ_{7v} valence band to the Γ_{8c} conduction band are dipole forbidden [141]. Generally, these selection rules may be softened in resonant Raman exciting conditions [141], meaning that resonant Raman scattering from an optically forbidden transition cannot be completely excluded. However, the fact that photoluminescence is observed from this energy gap leads to the conclusion that the transition should be the dipole allowed Γ_{7v} to Γ_{7c}. Consequently,the observed critical point with energy of 1.982 eV in wurtzite GaAs is assigned to the interband transition from the crystal-field split-off valence band to the Γ_{7c} conduction band. Finally, the experimental findings are compared with theoretical predictions. Based on an empirical pseudopotential
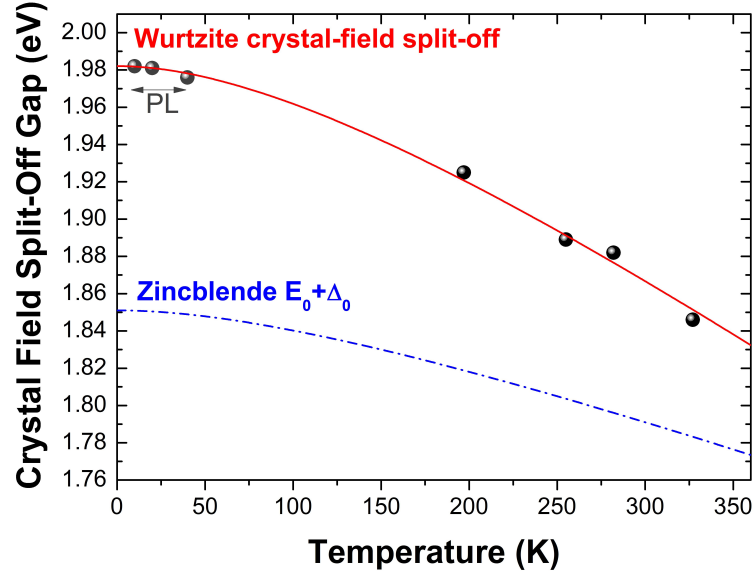
Figure 5.18: Temperature dependent variation of the crystal field split-off gap in wurtzite GaAs with a fit to the Varshni equation. The temperature dependence of the zincblende $E_0 + \Delta_0$ gap from Ref. [149] is shown for comparison.

method including spin-orbit coupling, De und Pryor calculated values of respectively 1.978 eV and 2.063eV for the Γ_{7v} to Γ_{8c} and Γ_{7v} to Γ_{7c} interband transitions. This means that the experiment agrees within 4% (81 meV) with this theory.

Finally, with the energies of the free exciton at the heavy-hole , light-hole , and crystal-field split-off) valence band that are 1.517 eV, 1.620 eV, and 1.982 eV, the spin-orbit splitting Δ_{so} and crystal-field-splitting Δ_{cr} can been extracted using the quasicubic approximation [121]:

$$E_1 - E_{2,3} = \frac{1}{2} \left(\Delta_{cr} + \Delta_{so} \mp \sqrt{(\Delta_{cr} + \Delta_{so})^2 - \frac{8}{3} \Delta_{cr} \Delta_{so}} \right) \tag{5.6}$$

By applying equation 5.6 to the experimental results values of $\Delta_{so} = 0.379$ eV and $\Delta_{cr} = 0.189$ eV are obtained. The value of the spin-orbit splitting is in very good agreement with the predictions of De and Pryor ($\Delta_{so} = 0.351$ eV). However, the crystal field spitting is smaller than the value they predicted ($\Delta_{cr} = 0.244$ eV) [118]. Meanwhile the experimental value for the crystal field splitting is larger than the value of $\Delta_{cr} = 0.122$ eV predicted in the pioneering theoretical work of Murayama and Nakayama [119]. The deviations might be due to the fact that they assume an ideal WZ structure in their calculations. The experimental value could be altered due to quantum confinement effects or the presence of strain, though small for

this type of nanowires [37]. In contrast, the experimental value is in excellent agreement with most recent calculations of Cheiwchanchamnangij and Lambrecht [150]. Within the GW approximation they obtained values of $\Delta_{cr} = 0.186$ eV using the LDA lattice constants and $\Delta_{cr} = 0.180$ eV using experimental data for the lattice volume.

5.3   Conclusions

It has been shown that resonant Raman spectroscopy is a powerful tool to determine the electronic band structure in novel semiconductor materials which may only exist on the nanoscale. By applying this technique to wurtzite GaAs nanowires, the position of the light-hole bands and the fundamental band gap have been measured. Equal energies for the free exciton at the wurtzite and the zinc-blende band gap are found within the experimental error. The experiments also indicate that the conduction band minimum in wurtzite GaAs is of Γ_7 symmetry. Furthermore, the position of the crystal-field split-off band of wurtzite GaAs by resonant Raman and photoluminescence spectroscopy has been determined. The temperature dependence was fit with the Varshni equation and the corresponding parameters were extracted.
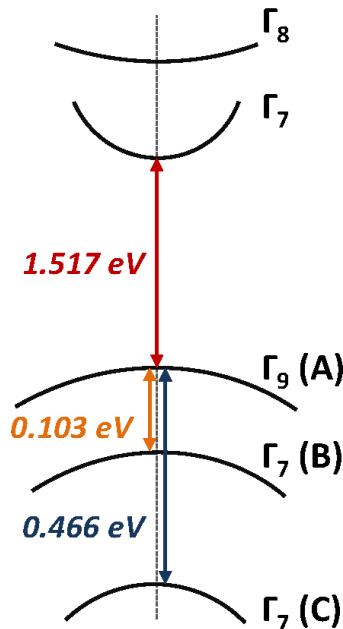
Figure 5.19: Band structure at the Γ point of WZ GaAs deduced from resonant Raman spectroscopy.

To summarize, the following picture of the electronic band structure at the Γ point in WZ GaAs

has been obtained by resonant Raman scattering from 2LO phonons. As depicted in Fig. 5.19, the energies of the free exciton at the heavy-hole ("A exciton"), light-hole ("B exciton"), and crystal-field split-off ("C exciton") valence band are found to be 1.517 eV, 1.620 eV, and 1.982 eV, respectively. The lowest conduction band exhibits Γ_7 symmetry.

6 Nanowire Heterostructures

Resonant Raman spectroscopy is realized on closely spaced nanowire based multi-quantum-wells. A quantization of the optical phonons consistent with 2.4 nm thick quantum wells is observed. This finding agrees well with photoluminescence experiments and cross-section transmission electron microscopy measurements. Within the quantized structure a high density photoexcited plasma forms which is demonstrated by the observation of coupled plasmon-LO-phonon modes in the Raman spectra. By varying the exctiation power, the density of the plasma and thereby the position of the coupled plasmon-phonon modes is controlled. This work is an important first step towards a deeper understanding of free charge systems in nanowire heterostructures.

6.1 Phonon Confinement and Plasmon-Phonon Interaction in Nanowire Quantum Wells

6.1.1 Introduction

Semiconductor nanowires provide a unique platform for the creation of novel types of nano-scale heterostructures. Remarkable features of these non-planar heterostructures compared to the conventional planar geometry include (i) an improved coupling with light, which makes them better absorbers or emitters in solar cells or light emitting diodes[151], (ii) the possibility of realizing both axial and radial heterostructures, (iii) the chance of combining mismatched materials in axial heterostructures, thanks to an effective radial strain release[152] and (iv) the possibility of obtaining two dimensional electron gases around the nanowire core [153].

In semiconductor materials, free carriers can be generated by intentional doping, thermal- or photoexcitation. In heterostructures such as quantum wells (QWs), wires or dots, these carriers are spatially confined [154, 155]. For example, in QWs carriers can propagate freely in two directions, while confined in the third one. Collective oscillations of charges or plasmons can be generated in QWs, as the small size and the confinement renders easier the generation of a high density plasma [156]. For the observation, it is also an important condition that the plasma remains in the confined structure. It is for this reason that collective carrier excitations in the core of nanowires have only been observed in indirect bandgap semiconductor nanowires before [157]. As it has been explained above, plasmons can interact with longitudinal optical phonons through their macroscopic electric field, giving rise to coupled phonon-plasmon modes [67]. The frequency of the coupled modes depends on the total concentration of free carriers and on the dimensionality, and therefore it is a measure of the carrier density in the system. Indeed, this type of measurements will be of great importance in the characterization of nanowires incorporating more complex structures such as a two (one) dimensional electron gas on the facets, achieved by modulation doping [153, 158].

In the following, resonant Raman experiments performed on individual undoped nanowires with a shell consisting of a sequence of narrow AlAs/GaAs/AlAs quantum wells will be presented.

6.1.2 Experimental

The synthesis of the MQW GaAs nanowires was carried out in the high mobility Gen-II MBE system, which allows to grow quantum heterostructures on the nanowire facets with very high crystalline quality and atomically sharp interfaces [29, 30]. (001) GaAs wafers have been used as substrates for the growth. The nanowire growth was carried out at a nominal GaAs growth rate of $0.45 \, \text{Ås}^{-1}$, an As_4 partial pressure of 3.5×10^{-6} mbar (Ga-rich conditions), a temperature of $630 \, °C$, and with a rotation of 4 rpm. An analysis of the ensemble revealed that the diameter was 85 ± 10 nm and uniform along the entire length.

(a)   **(b)**
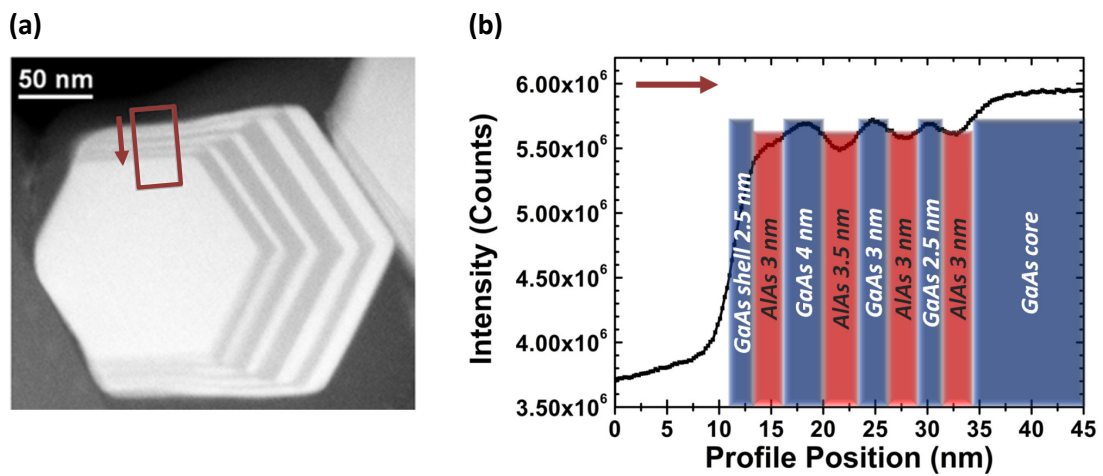
Figure 6.1: (a) Cross-section TEM micrograph of a GaAs nanowire presenting the AlAs/GaAs MQWs. (b) Analysis of the thickness of the MQWs grown on the lateral facets of the nanowire. The intensity contrast is proportional to the Z number and gives information about the composition. The intensity in the region marked in (a) has been integrated. The intensity profile is shown following the arrow.

The GaAs nanowires were used as the core for growing a series of multi-quantum wells of AlAs/GaAs with nominal thicknesses of (20/8/25/12/30/18/20 nm) on the facets. The nominal thickness corresponds to the thickness that would be obtained under such conditions on a planar substrate. As the nanowires grow along the [111] direction, the nanowires appear at an angle of 35° with the (001) GaAs substrates. This results in prismatic quantum wells where, intentionally, the quantum well thickness changes stepwise between different side facets. This is different from typical prismatic or core-shell heterostructures where the quantum well thickness is constant around the nanowire core [159, 28, 29]. Growth of the radial heterostructures on the nanowire facets was achieved by increasing the As_4 pressure to 5×10^{-5} mbar. A cross-section TEM image of the nanowire that enables the visualization of the
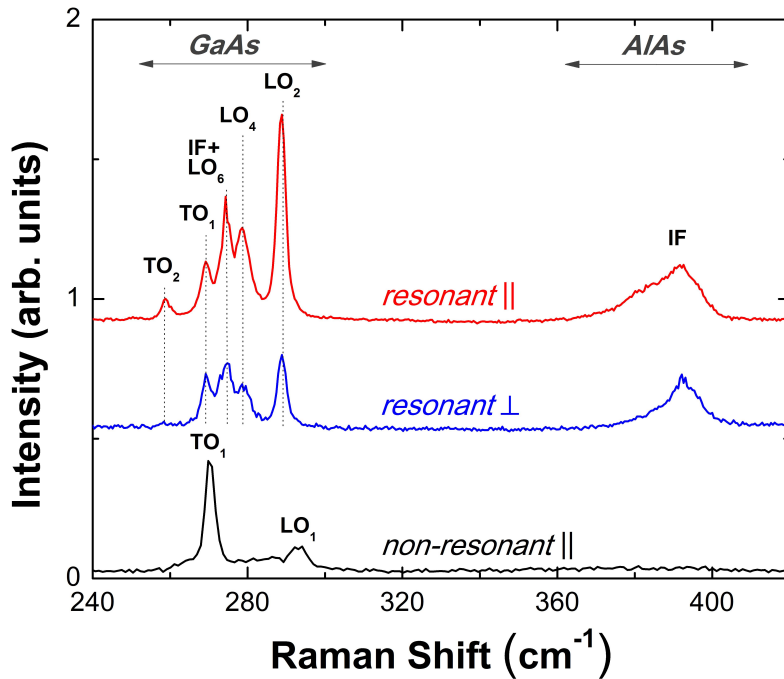
Figure 6.2: Polarized and depolarized spectra taken under resonant excitation with 647.1 nm radiation at very low laser power. For comparison, the spectrum of a the same nanowire under non-resonant excitation with 488 nm radiation is also shown (the intensities have been normalized).

QWs is shown in Fig. 6.1(b). The thickest quantum wells were obtained for the facets facing the molecular beam flux and the thinnest for the backside facets. For the lateral facets, it has been shown that there is a factor of about 3.5-4 between the nominal and measured thickness (Fig. 6.1 b) [29, 30]. In the following a nanowire with such kind of MQWs on the facets will be labeled as a MQW nanowire.

Raman scattering experiments were performed in backscattering geometry on single nanowires at 10 K. The 488 nm and 647.1 nm lines of an Ar^+Kr^+ laser and the 632.8 nm line of a HeNe laser were used for excitation. The power of the incident light was varied between 25 and 500 μW, corresponding to a change in the laser intensity from 2.9 kW cm^{-2} to 57.5 kW cm^{-2}.

6.1.3 Results and Discussion

Stokes Raman spectra taken on one of our nanowires are shown in Fig. 6.2. The measurements taken under parallel and perpendicular polarizations, which correspond to configurations where the polarization of the incident and scattered light are respectively parallel and per-
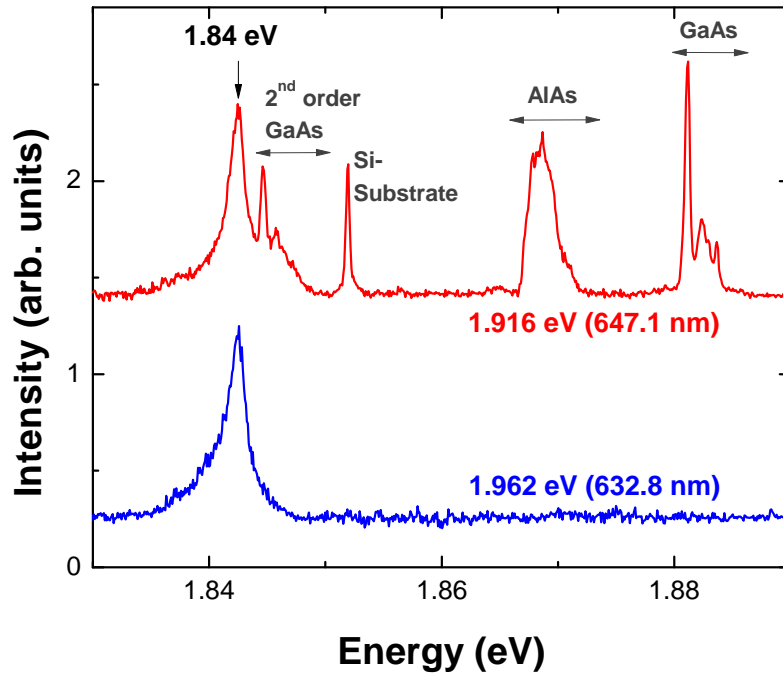
Figure 6.3: Spectra of a MQW nanowire taken at 10K with 1.916 eV (647.1 nm) and 1.962 eV (632.8 nm) radiation showing the Raman scattering peaks and the presence of a photoluminescence peak at 1.84 eV.

pendicular are included in the figure. These configurations are also known as polarized and depolarized. In both cases the incident polarization is parallel to the nanowire axis. For comparison, the polarized spectrum of the same MQW-nanowire taken under non-resonant conditions with 488 nm radiation at the same temperature is also plotted. The lines between 250 and 300 cm^{-1} correspond to the optical phonon modes of GaAs, i.e. TO, LO, and interface (IF) modes. In the AlAs optical phonon region, the broad peak at 380 cm^{-1} is attributed to in-plane interface modes. In the 250-300 cm^{-1} spectral range, the resonant Raman spectrum of the MQW nanowire is clearly richer than the spectrum taken under non-resonant conditions. The multiple lines appearing close to the TO and LO modes of GaAs can be attributed to quantized optical phonons in the MQWs [160]. Indeed, the large difference between the atomic masses of Ga and Al separates the optical phonon bands of the two compounds by more than 100 cm^{-1}. Hence, a phonon in one material is heavily damped in the other. As a consequence, the optical phonons with wave vectors normal to the layer planes are confined to the individual MQW layers, which in this way act also as phononic QWs. The quantized wavevectors q allowed in such structures can be calculated in an analogous way to those of a

vibrating string with fixed ends [161]:

$$q_m = \frac{m\pi}{d + \delta} \tag{6.1}$$

where m = 1,2,.. is an integer called the mode order, d is the GaAs quantum well thickness, and δ is the penetration depth of the phonon mode into the barrier (typically $\delta \sim 1$ monolayer). According to this, each of the modes appearing in the spectra of Fig. 6.3 has been labeled. One should note that only confined longitudinal modes LO_m with even symmetry appear in both the polarized and depolarized spectra. This is a consequence of the symmetry properties of the Fröhlich electron-LO-phonon interaction [162], which is the dominant scattering mechanism when the photon energy is near resonant electronic excitations. In Fig. 6.3 the photoluminescence spectra collected for excitations at 647.1 and 632.8 nm are shown. In both cases a peak at 1.84 eV is observed. Under the excitation of 647.1 nm additional peaks corresponding to Raman scattering from the MQW nanowire and the underlying Si-substrate appear. Under non-resonant conditions Raman scattering is several orders of magnitude weaker than luminescence. The enhancement of the Raman signal for the excitation at 647.1 nm (1.916 eV) is a clear indication of resonance excitation. Now, to understand the origin of the resonance, one should consider the electronic structure of the MQWs. Due to the small thickness of the GaAs MQWs and the AlAs barriers, minibands form in the conduction and light and heavy hole valence bands. Using the Kronig-Penney model one can calculate the energy position of such minibands. For QW and barrier thickness between 2 and 3 nm, a transition energies between the conduction and heavy hole miniband of about 1.8 eV is estimated. This is in good agreement with the observation of luminescence at 1.84 eV. One should add that inherently to the small thickness of the QWs and barriers, the resonance scattering profile should be relatively broad [162]. As shown in the work by Cardona et al [162], the resonance profile can be broader than 100 meV. This means that the excitation at 1.916 eV is in strong resonance with the transition between the first conduction and the heavy-hole subband. One should also mention that this luminescence peak exhibits a high degree of polarization, as expected from the antenna geometry of the nanowire. It is important to note that, as for the thick MQWs on the other facet of the nanowire and for the nanowire core the resonance conditions do not apply, one can exclusively see Raman scattering from the resonantly enhanced thin MQWs. To obtain measurable Raman signal from the thick quantum wells or from the nanowire core, a significant increase of the excitation power or the integration times is necessary.
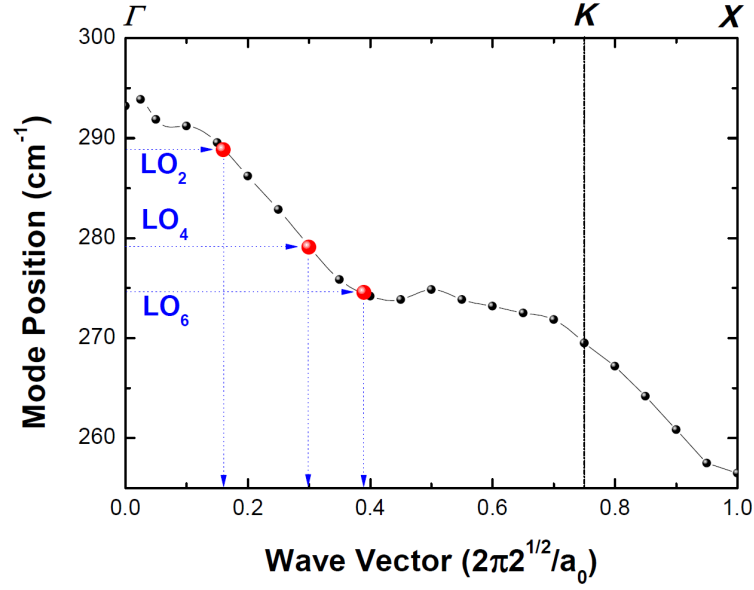
Figure 6.4: Experimental confined LO frequencies as a function of the confinement wave vector together with the experimental LO-phonon dispersion curve of bulk GaAs at 10K (adapted from Ref. [34]).

To further proof that the scattering from the narrow MQWs dominates the Raman spectra, the quantum well thickness is estimated from the position of the confined optical modes using equation 1. For this, the phonon wave vectors are related to relevant phonon frequencies via the phonon dispersion of GaAs [34]. In Fig. 6.4 the measured frequencies LO_m are shown versus the phonon wave vector q_m. Using equation 6.1 a quantum well thickness of 12 ± 1 GaAs monolayers is obtained. This corresponds to 24 ± 2 Å assuming a monolayer thickness of $d_{ml} = a_0\sqrt{2}/4 \approx 2$Å for (110) GaAs. The cross-section TEM micrograph of one of the MQW nanowires is shown in Figure 6.1 a. As mentioned above, the thickness of the QWs on the facets should depend on the angle of facets with the molecular beam [30]. The thickness of the GaAs QWs on the lateral facets ranges between 2.5 and 3.5 nm, while the AlAs layers have a thickness between 3 and 3.5 nm. The GaAs thickness corresponds quite well with the thickness of the QWs obtained from the LO quantized modes. As a consequence, this measurement allows to identify which facet of the nanowire is is probed in the Raman spectroscopy experiment. This is important for the discussion where the high density plasma is generated in the nanowires.

Now, the electronic excitations will be examined. In isolated quantum wells, carriers can propagate freely in the two in-plane directions and remain confined in the third one, i.e., perpendicular to the plane. The situation can change in closely spaced multi-quantum-well structures. If the barrier layers are thin enough, the overlapping of the electronic wave
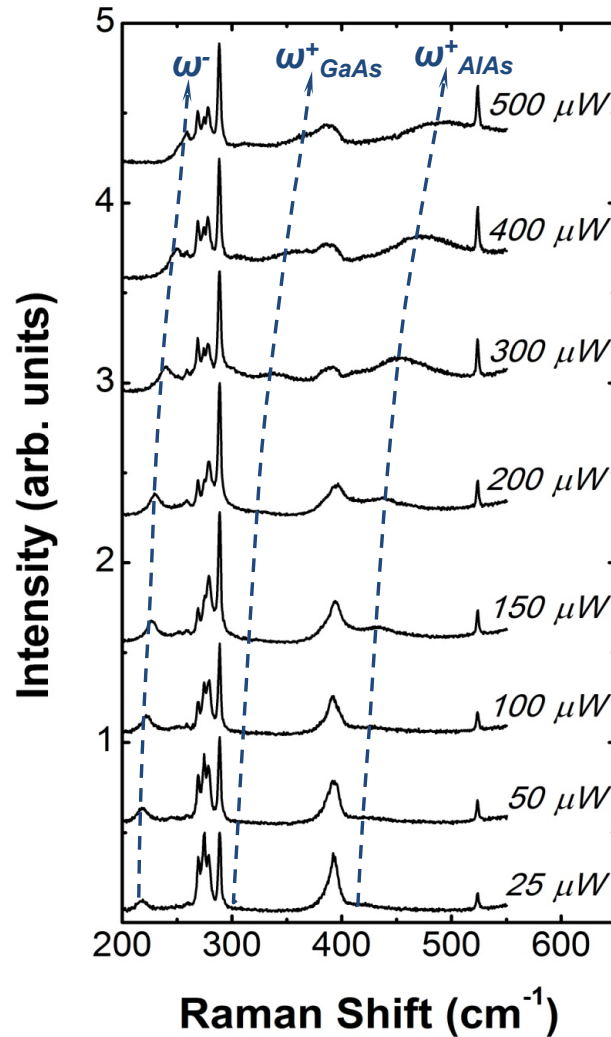
Figure 6.5: Raman spectroscopy on a single MQW nanowire. The laser intensity is tuned from $2.9\,\mathrm{kW\,cm^{-2}}$ (bottom curve) to $57.5\,\mathrm{kW\,cm^{-2}}$ (top curve). The spectra are offset for clarity.

functions in neighboring wells results in the formation of sub-bands [163]. Then, if plasmons are excited in such structures they stop to be purely two-dimensional and propagate both in the in-plane and perpendicular directions of the quantum wells [164]. Under sufficient continuous illumination power, a photo-excited steady state plasma can be generated within the quantum wells. Raman spectra taken on a single MQW nanowire for an increasing excitation power are shown in Fig. 6.5. In addition to the spectral features presented above, three other peaks are observed that shift to higher energies as the excitation power is increased. These lines are attributed to the phonon-plasmon interaction. Indeed, the interaction of the plasmons with the optical phonon modes of the MQW should result in the creation of three coupled
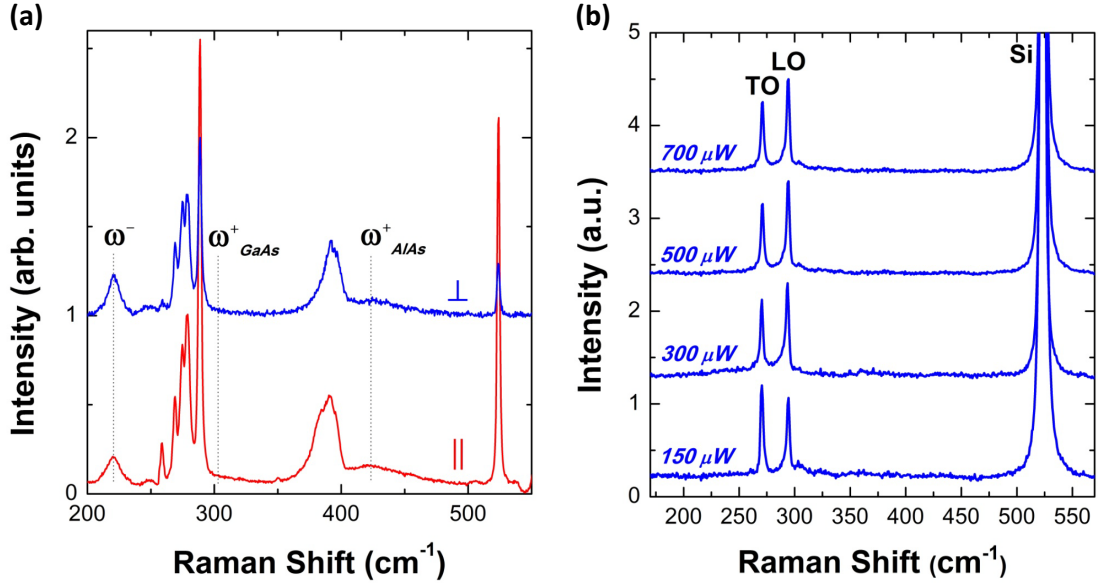
Figure 6.6: (a) Raman spectra of the coupled phonon-plasmon modes in polarized and depolarized configuration. The excitation power is 100 μW. (b) Raman spectra of an undoped GaAs nanowire without the MQW structure resonantly excited using a 647.1 nm laser with different laser power. A photoexcited cannot be established in this case.

phonon-plasmon modes. One low-frequency ω^- coupled mode and two high-frequency ω^+_{GaAs} (GaAs-like) and ω^+_{AlAs} (AlAs-like) coupled modes are expected in the Raman spectra [165]. The modes shift in frequency for an increasing excitation power as a consequence of the increase in free carrier concentration in the QWs. Here, the free carrier concentration and with it the frequency of the coupled modes can be dynamically tuned in the experiment by changing the laser power. It is important to note that in a pure GaAs nanowire without the MQW structure the generation of a stable electron-hole plasma is not observable, even if the nanowire surface is passivated by an AlGaAs shell. This is shown in Fig. 6.6 b.It demonstrates that the carriers have to be enclosed within the heterostructure in order to create a stable plasma.

The coupled phonon-plasmon modes are observed in both the polarized and the depolarized Raman spectra in Fig.6.6 a. In the photoexcited MQWs the phonon and electron-hole excitations are renormalized into mixed phonon-plasmon modes. Consequently, the coupled modes can be excited either by the charge-density mechanism or by the forbidden intraband Fröhlich interaction [166]. Both mechanisms imply polarized scattering with parallel incident and scattered light. However, under strong resonance conditions Fröhlich induced LO phonons

have been observed in both the polarized and depolarized configuration. To explain this unexpected behavior, an impurity-induced Fröhlich interaction was suggested to explain the presence of depolarized scattering [162]. Therefore, this mechanism may also contribute to the Raman scattering from the coupled phonon-plasmon modes in the depolarized configuration.
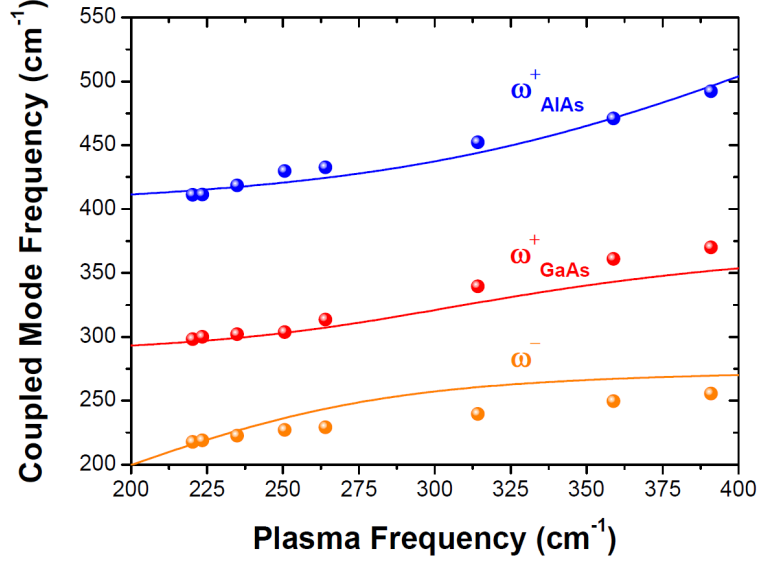
Figure 6.7: Calculated (lines) and experimental frequencies (points) of the coupled plasmon-phonon modes with the electric polarization directed normal to the layers.

One can calculate the frequencies of the plasmon-phonon coupled modes propagating along the MQW axis as a function of the excitation power within the framework of the effective medium theory that has been successfully applied in semiconductor superlattice (SL) structures[165, 167]. The basic assumption behind this theory is that in the long-wavelength limit, where the thickness of the MQW or SL layers is much smaller than the phonon wavelength, the AlAs/GaAs multilayer structure behaves as an 'effective' medium with averaged dielectric functions:

$$\epsilon_x(\omega) = \frac{\epsilon_1 d_1 + \epsilon_2 d_2}{d_1 + d_2} \qquad\qquad \epsilon_z(\omega) = \frac{d_1 + d_2}{d_1/\epsilon_1 + d_2/\epsilon_2} \qquad (6.2)$$

Here, the z-axis is normal to the MQW layers and the x- and y-axes define the MWQ plane. ϵ_1 and ϵ_2 are the dielectric functions of the individual materials, in our case GaAs and AlAs, and d_1 and d_2 denote the thickness of the layers (in the following $d_1 = d_2$ is assumed). If the barriers are thin enough so that a miniband structure is established, quasi-three-dimensional

(a)

(b)
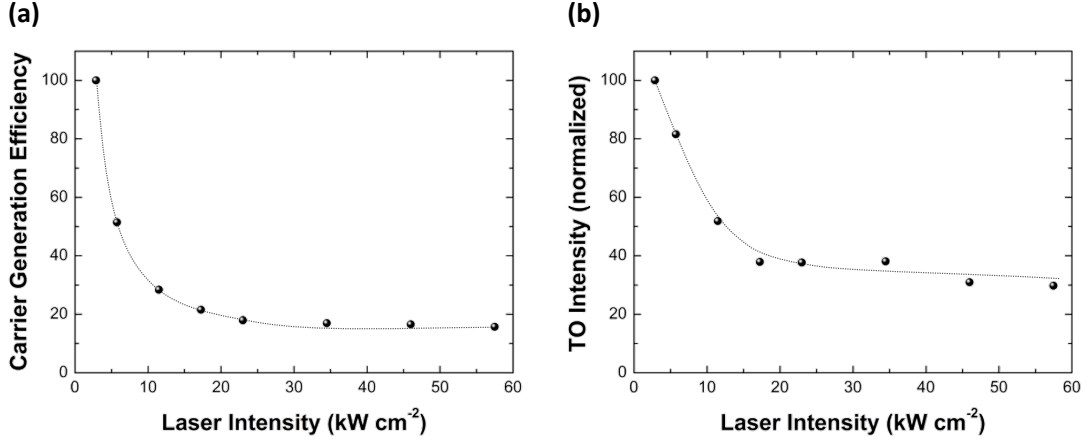
Figure 6.8: (a) Carrier generation efficiency (%) and (b) normalized TO intensity (%)

intrasubband plasmon oscillations along the MQW axis can exist. Then, including the Drude dielectric function for free carriers, the z-component of the dielectric function can be written as:

$$\epsilon_z(\omega) = \frac{d_1 + d_2}{d_1/\epsilon_1 + d_2/\epsilon_2} - \frac{\omega_p^2}{\omega^2} \tag{6.3}$$

where ω_p is the plasma frequency. Finally, the frequencies of the coupled longitudinal optical phonon-plasmon modes of the MQW or SL are obtained from the zeros of the dielectric function. The results are shown in Fig. 6.8 a. By fitting the experimental data and the theoretical curves the three dimensional plasma frequency $\omega_p = \sqrt{4\pi e^2 n/m^*}$ for the intrasubband plasmon vibrations along the MQW axis can be determined. One has to note that the contribution of photogenerated holes to the plasma frequency and the overall behavior of the coupled modes can be neglected due to the high effective hole mass [168]. The plasma frequency increases from 220.3 cm^{-1} to 391 cm^{-1} when the laser intensity is tuned from 2.9 kW cm^{-2} to 57.5 kW cm^{-2}. This corresponds to an increase of the carrier density n from 4.2 to 13.0 x 10^{17} cm^{-3} (with the effective mass $m^* = 0.0665\ m_0$ of bulk GaAs). Interestingly, there is only a threefold increase in the carrier density for an increase of excitation power of a factor of nearly 20.

In order to understand this, the efficiency in the carrier generation as a function of the excitation power has been extracted from the experimental data. In Fig. 6.8 a the carrier generation
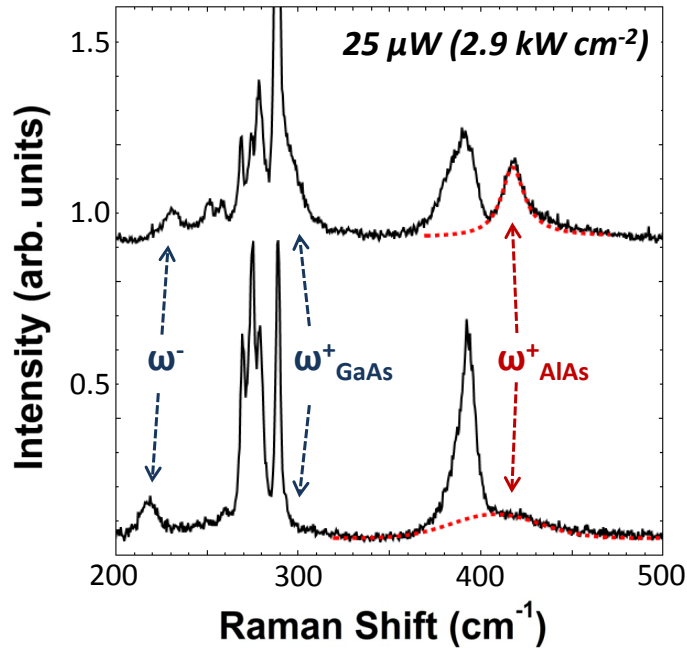
Figure 6.9: Raman spectra showing the coupled LO-phonon-plasmon modes at two different positions of the same nanowire. Both spectra have been taken under otherwise same conditions with a laser power of 25 μW.

efficiency is plotted by normalizing it to the efficiency at lowest laser intensity in the experiment. The efficiency decreases with increasing laser intensity and levels off at about 15%. This decrease is attributed to the activation of non-radiative recombination channels, especially Auger processes, that can significantly decrease the carrier generation efficiency at high carrier densities [169]. One should point out, that the same effect is found in the Raman scattering efficiency. The relative intensity of the TO mode normalized to the corresponding laser intensity is shown in Fig. 6.8 b. It decreases nonlinear with increasing excitation power. The behavior is similar to the decreasing efficiency for photoexcited carrier generation with increasing laser intensity. Accordingly, the probability of a Raman scattering event decreases when other non-radiative recombination paths start to compete with the Raman scattering process.

Finally, the mobility of the free carriers in the MQW structures will be addressed. In the fourth chapter of this work an overdamping of the free electron plasma was observed in the case of n-doped GaAs nanowires. This was assigned with a decrease in the mobility due to surface scattering in the nanowire samples. The characteristic of an overdamped system is the pinning of the coupled LO phonon-plasmon modes at the TO phonon frequency [98]. Such a behavior

is not observed in case of the MQW nanowire samples. Here, the three coupled modes and their dependency on the plasma frequency are well described by the model given in equation 6.3 where damping effects are completely neglected. This implies long lifetimes of the free carriers enclosed in the MQW structure, and it suggests the possibility to achieve high mobility electron gases in future modulation-doped nanowire heterostructures. However, inhomogeneous lifetime broadening effects have been observed during the measurements. In Fig. 6.9 Raman spectra taken at two different positions of the same nanowire under otherwise identical conditions are shown. A remarkable change in the linewidth of coupled modes is observed. Especially, the width of the coupled ω^+_{AlAs} mode increases from about 15 cm^{-1} to about 40 cm^{-1}, indicating a notable decrease in the plasmon lifetime. This effect may be assigned with variations in the local environment due to inhomogeneities such as defects or quantum well thickness fluctuations. Understanding these effects is of fundamental importance because inhomogeneities along the nanowire axis may strongly affect the electrical transport properties of future devices based on nanowire heterostructures.

6.2 Conclusions

Resonant Raman spectroscopy has been applied to study the structural quality of nanowire based multi-quantum-wells and the behavior of photoexcited carriers in the heterostructure. Important information on the quality of the structure has been obtained by scattering from confined transverse and longitudinal optical phonons and interface modes. From the position of the well defined confined modes the thickness of the MQW layers could be analyzed with high accuracy. Furthermore, the creation of a photogenerated electron-hole plasma within the closely spaced MQWs grown on the facets of a GaAs nanowire has been demonstrated. The excitation power can be used to control the plasma density, as shown by the position of the modes of the plasmon-phonon interaction. By contrast, the formation of a stable photoexcited plasma is not observable in the bare GaAs nanowire core. A decrease in the efficiency in the carrier generation is observed at high excitation due to the increasing influence of non-radiate recombination channels such as Auger-processes.

Efficient doping and the experimental determination of the resulting carrier concentration represent major challenges in current nanowire research. It has been demonstrated that resonant Raman scattering can be used as a meaningful probe to characterize the electronic system in nanowire based heterostructures. This is an important step towards the understanding of the free carrier behavior in doped nanowires incorporating QWs or other heterojunctions.

7 Summary

The main results and major accomplishments of the thesis are summarized in this last chapter. The key features are the implementation of an optical laboratory for low temperature Raman spectroscopy and the successful application of Raman scattering techniques to diverse open problems in nanowire research. Among these are the challenge of doping in nanowires, the investigation of the electronic band structure in novel semiconductor polytypes, and the study of free carrier systems in nanowire heterostructures.

A wide spectrum of Raman techniques has been applied in this work to answer various open questions in the field of nanowire research. For that purpose, a home-made setup for low temperature micro-Raman spectroscopy has been built at the beginning of the thesis work. In the subsequent experimental part of the thesis, focus was put on the understanding and the control of the doping mechanism in semiconductor nanowires, the investigation of the electronic band structure in the wurtzite phase of GaAs, and the examination of the structural and electronic properties of semiconductor nanowire based heterostructures. The following highlights the important results of this work:

Doping mechanisms in GaAs nanowires

In a first approach the incorporation pathways of silicon dopants during the MBE growth of GaAs nanowires have been studied. It was shown that the doping process of p-type GaAs is governed by an incorporation of dopants into the side facets of the nanowire, resulting in a highly doped shell around a lower doped nanowire core. By studying the local vibrational modes of the Si dopants in the GaAs host lattice, evidence of strong doping compensation was found in the highest doped samples. The underlying mechanisms that drive the electrical deactivation of the dopants have been analyzed and explained in detail. From an analysis of the coupled LO-phonon-plasmon modes in the Raman spectra taken in forward scattering geometry, the free carrier concentration and the mobility could be determined in individual nanowires. Evidence for the existence of an overdamped electron plasma was found in n-type nanowires. This is attributed to the low mobility of the samples due to the influence of doping compensation and the scattering at the nanowire surface.

Untangling the electronic band structure of wurtzite GaAs

Resonant Raman spectroscopy has been successfully applied to determine the electronic band structure of the wurtzite phase of GaAs that only exists in the nanowire form. The position of the three valence bands and the fundamental band gap has been measured. Interestingly, equal energies for the free exciton at the wurtzite and the zinc-blende band gap are found within the experimental error. The experiments also indicate that the conduction band minimum in wurtzite GaAs is of Γ_7 symmetry.

Phonons and plamons in nanowire heterostructures

The structural quality of closely spaced multi-quantum-wells grown on the facets of a GaAs nanowire and the behavior of photoexcited carriers within the heterostructure have been investigated by resonant Raman spectroscopy. The clear and distinct Raman spectra of the confined optical modes not only reflect the high quality of the structure, but they also allow

an accurate analysis of the thickness of the MWQ layers. The formation of a photoexcited electron-hole plasma that can be controlled with the laser excitation power was demonstrated. It was shown that a stable plasma can only be established when the free carriers are enclosed within the heterostructure.

Besides these key aspects of the thesis, various other subjects have been addressed in collaborative projects. For instance, the crystal structure and composition of InGaAs, $LiNbO_3$, and $KNbO_3$ nanowires has been examined by Raman spectroscopy. Moreover, photoluminescence and Raman experiments have been performed to study the electro-optic properties of mono- and multilayers of $MoSe_2$. Most recently, the constitution of carbonous thin films prepared from molecular precursors has been examined using these two spectroscopy techniques.

In conclusion, in this work Raman spectroscopy has been applied as a powerful tool to study the structural, electrical, and optical properties of semiconductors on the nanoscale. The knowledge gained on the doping mechanisms will be implemented into the design of future nanowire devices in our group. Strong implications for the use of wurtzite GaAs nanowires for optoelectronic applications are expected from the detailed information on the band structure of this novel material that has been obtained in this thesis. Finally, with the work on nanowire multi-quantum-well structures an important step towards the understanding of low dimensional free carrier systems in nanowire based heterostructures has been achieved.

Bibliography

[1] Y. Cui and C. M. Lieber, "Functional nanoscale electronic devices assembled using silicon nanowire building blocks," *Science*, vol. 291, p. 851, 2001.

[2] M. S. Gudiksen, L. J. Lauhon, J. Wang, D. C. Smith, and C. M. Lieber, "Growth of nanowire superlattice structures for nanoscale photonics and electronics," *Nature*, vol. 415, p. 617, 2002.

[3] J. Johansson, L. S. Karlsson, C. P. T. Svensson, T. Mårtensson, B. A. Wacaser, K. Deppert, L. Samuelson, and W. Seifert, "Structural properties of (111)B -oriented iii-v nanowires," *Nature Mater.*, vol. 5, p. 574, 2006.

[4] F. Qian, S. Gradečak, Y. Li, H.-G. Park, Y. Dong, Y. Ding, Z. L. Wang, and C. M. Lieber, "Multi-quantum-well nanowire heterostructures for wavelength-controlled lasers," *Nat. Mater.*, vol. 7, p. 701, 2008.

[5] S. Nadj-Perge, S. M. Frolov, E. P. A. M. Bakkers, and L. P. Kouwenhoven, "Spin-orbit qubit in a semiconductor nanowire," *Nature*, vol. 468, p. 1084, 2010.

[6] Z. Cui, Y.and Zhong, D. Wang, W. U. Wang, and C. M. Lieber, "High performance silicon nanowire field effect transistors," *Nano Lett.*, vol. 3, p. 149, 2003.

[7] G. Zheng, F. Patolsky, Y. Cui, W. U. Wang, and C. M. Lieber, "Multiplexed electrical detection of cancer markers with nanowire sensor arrays," *Nat. Biotechnol.*, vol. 23, p. 1294, 2005.

[8] C. K. Chan, H. L. Peng, G. Liu, K. McIlwrath, X. F. Zhang, R. A. Huggins, and Y. Cui, "High-performance lithium battery anodes using silicon nanowires," *Nature Nanotechnol.*, vol. 3, p. 31, 2008.

[9] C. Colombo, M. Heiss, M. Gratzel, and A. Fontcuberta i Morral, "Gallium arsenide p-i-n radial structures for photovoltaic applications," *Appl. Phys. Lett.*, vol. 94, p. 173108, 2009.

Bibliography

[10] A. I. Hochbaum, R. K. Chen, R. D. Delgado, W. J. Liang, E. C. Garnett, M. Najarian, A. Majumdar, and P. D. Yang, "Enhanced thermoelectric performance of rough silicon nanowires," *Nature*, vol. 451, p. 163, 2008.

[11] M. T. Bjoerk, C. Thelander, A. E. Hansen, L. E. Jensen, M. W. Larsson, L. R. Wallenberg, and L. Samuelson, "Few-electron quantum dots in nanowires," *Nano Lett.*, vol. 4, p. 1621, 2004.

[12] F. Giazotto, P. Spathis, S. Roddaro, S. Biswas, F. Taddei, M. Governale, and L. Sorba, "A josephson quantum electron pump," *Nature Phys.*, vol. Article ASAP, 2011.

[13] A. P. Alivisatos, "Semiconductor clusters, nanocrystals, and quantum dots," *Science*, vol. 271, p. 933, 1996.

[14] C. M. Lieber, "One-dimensional nanostructures: Chemistry, physics & applications," *Solid State Commun.*, vol. 107, p. 607, 1998.

[15] X. Peng, L. Manna, W. Yang, J. Wickham, E. Scher, A. Kadavanich, and A. P. Alivisatos, "Shape control of CdSe nanocrystals," *Nature*, vol. 404, p. 59, 2000.

[16] T. Mårtensson, C. P. T. Svensson, B. A. Wacaser, M. W. Larsson, W. Seifert, K. Deppert, A. Gustafsson, L. R. Wallenberg, and L. Samuelson, "Epitaxial iii-v nanowires on silicon," *Nano Lett.*, vol. 4, p. 1987, 2004.

[17] P. Yang, R. Yan, and M. Fardy, "Semiconductor nanowire: What's next?," *Nano Lett.*, vol. 10, p. 1529, 2010.

[18] A. Cho and J. Arthur, "Molecular beam epitaxy," *Prog. Solid State Chem.*, vol. 10, p. 157, 1975.

[19] D. T. J. Hurle, "A comprehensive thermodynamic analysis of native point defect and dopant solubilities in gallium arsenide," *J. Appl. Phys.*, vol. 85, p. 6957, 1999.

[20] P. V. Radovanovic, "Nanowires: Keeping track of dopants," *Nat. Nano.*, vol. 4, p. 282, 2009.

[21] R. S. Wagner and W. C. Ellis, "Vapor-liquid-solid mechanism of single crystal growth," *Appl. Phys. Lett.*, vol. 4, p. 89, 1964.

[22] M. Law, J. Goldberger, and P. Yang, "Semiconductor nanowires and nanotubes," *Annu. Rev. Mater. Res.*, vol. 34, p. 83, 2004.

[23] F. J. Lopez, E. R. Hemesath, and L. J. Lauhon, "Ordered stacking fault arrays in silicon nanowires," *Nano Lett.*, vol. 9, p. 2774, 2009. PMID: 19527044.

[24] A. Fontcuberta i Morral, J. Arbiol, J. D. Prades, A. Cirera, and J. R. Morante, "Synthesis of silicon nanowires with wurtzite crystalline structure by using standard chemical vapor deposition," *Adv. Mater.*, vol. 19, p. 1347, 2007.

[25] N. Akopian, G. Patriarche, L. Liu, J.-C. Harmand, and V. Zwiller, "Crystal phase quantum dots," *Nano Lett.*, vol. 10, p. 1198, 2010. PMID: 20205446.

[26] Z. Ikonic, G. P. Srivastava, and J. C. Inkson, "Optical properties of twinning superlattices in diamond-type and zinc-blende-type semiconductors," *Phys. Rev. B*, vol. 52, p. 14078, 1995.

[27] K. v. Klitzing, G. Dorda, and M. Pepper, "New method for high-accuracy determination of the fine-structure constant based on quantized Hall resistance," *Phys. Rev. Lett.*, vol. 45, p. 494, 1980.

[28] C. Colombo, D. Spirkoska, M. Frimmer, G. Abstreiter, and A. Fontcuberta i Morral, "Ga-assisted catalyst-free growth mechanism of GaAs nanowires by molecular beam epitaxy," *Phys. Rev. B*, vol. 77, p. 155326, 2008.

[29] A. Fontcuberta i Morral, D. Spirkoska, J. Arbiol, M. Heigoldt, J. R. Morante, and G. Abstreiter, "Prismatic quantum heterostructures synthesized on molecular-beam epitaxy GaAs nanowires," *Small*, vol. 4, p. 899, 2008.

[30] M. Heigoldt, J. Arbiol, D. Spirkoska, J. M. Rebled, S. Conesa-Boj, G. Abstreiter, F. Peiró, J. R. Morante, and A. Fontcuberta i Morral, "Long range epitaxial growth of prismatic heterostructures on the facets of catalyst-free GaAs nanowires," *J. Mater. Chem.*, vol. 19, p. 840, 2009.

[31] D. Spirkoska, J. Arbiol, A. Gustafsson, S. Conesa-Boj, F. Glas, I. Zardo, M. Heigoldt, M. H. Gass, A. L. Bleloch, S. Estrade, M. Kaniber, J. Rossler, F. Peiro, J. R. Morante, G. Abstreiter, L. Samuelson, and A. Fontcuberta i Morral, "Structural and optical properties of high quality zinc-blende/wurtzite GaAs nanowire heterostructures," *Phys. Rev. B*, vol. 80, p. 245325, 2009.

[32] B. Prévot and J. Wagner, "Raman characterization of semiconducting materials and related structures," *Prog. Cryst. Growth Charact. Mater.*, vol. 22, p. 245, 1991.

[33] P. Y. Yu and M. Cardona, *Fundamentals of Semiconductors.* Springer Berlin / Heidelberg, 2010.

[34] D. Strauch and B. Dorner, "Phonon dispersion in GaAs," *J. Phys.: Condens. Matter.*, vol. 2, p. 1457, 1990.

[35] C. A. Arguello, D. L. Rousseau, and S. P. S. Porto, "First-order raman effect in wurtzite-type crystals," *Phys. Rev.*, vol. 181, p. 1351, 1969.

[36] S. Crankshaw, L. C. Chuang, M. Moewe, and C. Chang-Hasnain, "Polarized zone-center phonon modes of wurtzite GaAs," *Phys. Rev. B*, vol. 81, p. 233303, 2010.

[37] I. Zardo, S. Conesa-Boj, F. Peiro, J. R. Morante, J. Arbiol, E. Uccelli, G. Abstreiter, and A. Fontcuberta i Morral, "Raman spectroscopy of wurtzite and zinc-blende GaAs nanowires - polarization dependence, selection rules, and strain effects," *Phys. Rev. B*, vol. 80, p. 245324, 2009.

[38] R. Loudon, "The Raman effect in crystals," *Adv. in Phys.*, vol. 50, p. 813, 2001.

[39] W. Richter, "Resonant Raman scattering in semiconductors," in *Solid-State Physics*, vol. 78 of *Springer Tracts in Modern Physics*, pp. 121–272, Springer Berlin / Heidelberg, 1976. 10.1007/BFb0121253.

[40] R. Trommer and M. Cardona, "Resonant Raman scattering in GaAs," *Phys. Rev. B*, vol. 17, p. 1865, 1978.

[41] W. Kauschke and M. Cardona, "Resonant Raman scattering in semiconductors," *Phys. Scr.*, vol. 1989, p. 201, 1989.

[42] A. A. Gogolin and E. I. Rashba, "Mechanism of strong resonant 1LO Raman scattering," *Solid State Commun.*, vol. 19, p. 1177, 1976.

[43] C. Trallero-Giner, A. Cantarero, M. Cardona, and M. Mora, "Impurity-induced resonant Raman scattering," *Phys. Rev. B*, vol. 45, p. 6601, 1992.

[44] *www.ramanscattering.eu/raman/texts/032_text_22.php*.

[45] G. D. Pitt, D. N. Batchelder, R. Bennett, R. W. Bormett, I. P. Hayward, B. J. E. Smith, K. P. J. Williams, Y. Y. Yang, K. J. Baldwin, and S. Webster, "Engineering aspects and applications of the new Raman instrumentation," *IEE P-Sci. Meas. Tech.*, vol. 152, p. 241, 2005.

[46] K. Hiruma, M. Yazawa, T. Katsuyama, K. Ogawa, K. Haraguchi, M. Koguchi, and H. Kakibayashi, "Growth and optical properties of nanometer-scale GaAs and InAs whiskers," *J. Appl. Phys.*, vol. 77, p. 447, 1995.

[47] P. V. Radovanovic, C. J. Barrelet, S. Gradečak, F. Qian, and C. M. Lieber, "General synthesis of manganese-doped ii-vi and iii-v semiconductor nanowires," *Nano Lett.*, vol. 5, p. 1407, 2005. PMID: 16178248.

[48] C. Gutsche, I. Regolin, K. Blekker, A. Lysov, W. Prost, and F. J. Tegude, "Controllable p-type doping of GaAs nanowires during vapor-liquid-solid growth," *J. Appl. Phys.*, vol. 105, p. 024305, 2009.

[49] M. Hilse, M. Ramsteiner, S. Breuer, L. Geelhaar, and H. Riechert, "Incorporation of the dopants Si and Be into GaAs nanowires," *Appl. Phys. Lett.*, vol. 96, p. 193104, 2010.

[50] D. E. Perea, E. R. Hemesath, E. J. Schwalbach, J. L. Lensch-Falk, P. W. Voorhees, and L. J. Lauhon, "Direct measurement of dopant distribution in an individual vapour-liquid-solid nanowire," *Nat. Nanotechnol.*, vol. 4, p. 315, 2009.

[51] E. C. Garnett, J. C. Tseng, D. R. Khanal, J. Wu, J. Bokor, and P. Yang, "Dopant profiling and surface analysis of silicon nanowires using capacitance-voltage measurements," *Nat. Nanotechnol.*, vol. 4, p. 311, 2009.

[52] E. Tutuc, J. Appenzeller, M. C. Reuter, and S. Guha, "Realization of a linear germanium nanowire p-n junction," *Nano Lett.*, vol. 6, p. 2070, 2006. PMID: 16968027.

[53] G. Imamura, T. Kawashima, M. Fujii, C. Nishimura, T. Saitoh, and S. Hayashi, "Distribution of active impurities in single silicon nanowires," *Nano Lett.*, vol. 8, p. 2620, 2008. PMID: 18700807.

[54] E. Koren, J. K. Hyun, U. Givan, E. R. Hemesath, L. J. Lauhon, and Y. Rosenwaks, "Obtaining uniform dopant distributions in VLS-grown Si nanowires," *Nano Lett.*, vol. 11, p. 183, 2011.

[55] J. Y. Tsao, *Materials Fundamentals of Molecular Beam Epitaxy.* Academic Press Inc.: San Diego, CA, 1993.

[56] G. B. Stringfellow, *Organometallic Vapor-Phase Epitaxy: Theory and Practice.* Academic Press Inc.: San Diego, CA, 1999.

[57] F. E. Rosztoczy and K. B. Wolfstirn, "Distribution coefficient of germanium in gallium arsenide crystals grown from gallium solutions," *J. Appl. Phys.*, vol. 42, p. 426, 1971.

[58] M. J. Ashwin, R. Addinall, M. R. Fahy, R. Newman, I. Silier, and E. Bauser, "Si acceptors and their passivation by hydrogen in p-type liquid phase epitaxial and molecular beam epitaxial GaAs," *Mater. Sci. Forum*, vol. 17, p. 265, 1993.

[59] P. F. Fewster and A. F. W. Willoughby, "The effect of silicon doping on the lattice parameter of gallium arsenide grown by liquid-phase epitaxy, vapour-phase epitaxy and gradient-freeze techniques," *J. Cryst. Growth*, vol. 50, p. 648, 1980.

[60] R. C. Newman, "The lattice locations of silicon impurities in GaAs: effects due to sto-ichiometry, the Fermi energy, the solubility limit and DX behaviour," *Semicond. Sci. Technol.*, vol. 9, p. 1749, 1994.

[61] R. C. Newman, "The upper limits of useful n- and p-type doping in GaAs and AlAs," *Mater. Sci. Eng., B*, vol. 66, p. 39, 1999.

[62] J. M. Ballingall and C. E. C. Wood, "Crystal orientation dependence of silicon autocompensation in molecular beam epitaxial gallium arsenide," *Appl. Phys. Lett.*, vol. 41, p. 947, 1982.

[63] J. Wagner and M. Ramsteiner, "Raman spectroscopic assessment of Si and Be local vibrational modes in GaAs layers grown by molecular beam epitaxy," *IEEE J. Quantum Elect.*, vol. 25, p. 993, 1989.

[64] M. Ramsteiner, J. Wagner, H. Ennen, and M. Maier, "Resonance Raman scattering of Si local vibrational modes in GaAs," *Phys. Rev. B*, vol. 38, p. 10669, 1988.

[65] G. Abstreiter, M. Cardona, and A. Pinczuk, "Light scattering by free carrier excitations in semiconductors," in *Light Scattering in Solids IV* (M. Cardona and G. Güntherodt, eds.), vol. 54 of *Topics in Applied Physics*, pp. 5–150, Springer Berlin / Heidelberg, 1984.

[66] A. Mooradian and G. B. Wright, "Observation of the interaction of plasmons with longi-tudinal optical phonons in GaAs," *Phys. Rev. Lett.*, vol. 16, p. 999, 1966.

[67] B. B. Varga, "Coupling of plasmons to polar phonons in degenerate semiconductors," *Phys. Rev.*, vol. 137, p. A1896, 1965.

[68] A. A. Klochikhin, V. Y. Davydov, V. V. Emtsev, A. N. Smirnov, and R. v. Baltz, "A gauge invariant approach to the Raman scattering in heavily doped crystals," *Phys. Status Solidi B*, vol. 242, p. R58, 2005.

[69] R. Fukasawa, M. Wakaki, K. Ohta, and H. Okumura, "Raman scattering determination of free carrier concentration and surface depletion layer in (100) p-GaAs grown by molecular-beam epitaxy," *Jpn. J. Appl. Phys.*, vol. 25, p. 652, 1986.

[70] D. Olego and M. Cardona, "Raman scattering by coupled LO-phonon-plasmon modes and forbidden TO-phonon raman scattering in heavily doped *p*-type GaAs," *Phys. Rev. B*, vol. 24, p. 7217, 1981.

[71] T. Yuasa and M. Ishii, "Raman scattering study of coupled hole-plasmon-LO-phonon modes in p-type GaAs and p-type al_xga_{1-x}as," *Phys. Rev. B*, vol. 35, p. 3962, 1987.

[72] A. Mlayah, R. Carles, G. Landa, E. Bedel, and A. Muñoz Yagüe, "Raman study of longitudinal optical phonon-plasmon coupling and disorder effects in heavily Be-doped GaAs," *J. Appl. Phys.*, vol. 69, p. 4064, 1991.

[73] K. Wan and J. F. Young, "Interaction of longitudinal-optic phonons with free holes as evidenced in Raman spectra from Be-doped p-type GaAs," *Phys. Rev. B*, vol. 41, p. 10772, 1990.

[74] R. Fukasawa and S. Perkowitz, "Raman-scattering spectra of coupled LO-phonon-hole-plasmon modes in p-type GaAs," *Phys. Rev. B*, vol. 50, p. 14119, 1994.

[75] M. Seon, M. Holtz, W. M. Duncan, and T. S. Kim, "Raman studies of heavily carbon doped GaAs," *J. Appl. Phys.*, vol. 85, p. 7224, 1999.

[76] T. Kamijoh, A. Hashimoto, H. Takano, and M. Sakuta, "Inelastic light scattering from heavily doped and highly compensated GaAs:Si," *J. Appl. Phys.*, vol. 59, p. 2382, 1986.

[77] R. Fukasawa, S. Katayama, A. Hasegawa, and K. Ohta, "Analysis of Raman spectra from heavily doped *p*-GaAs," *J. Phys. Soc. Jpn.*, vol. 57, p. 3632, 1988.

[78] G. Irmer, M. Wenzel, and J. Monecke, "Light scattering by a multicomponent plasma coupled with longitudinal-optical phonons: Raman spectra of *p*-type GaAs:Zn," *Phys. Rev. B*, vol. 56, p. 9524, 1997.

[79] J. D. Wiley and M. DiDomenico, "Lattice mobility of holes in iii-v compounds," *Phys. Rev. B*, vol. 2, p. 427, 1970.

Bibliography

[80] G. Irmer, W. Siegel, G. Kuhnel, J. Monecke, F. M. M. Yasuoka, B. H. Bairamov, and V. V. Toporov, "Determination of the hole concentration and mobility of p-GaP by Hall and by Raman measurements," *Semicond. Sci. Technol.*, vol. 6, p. 1072, 1991.

[81] B. D. Gerardot, D. Brunner, P. A. Dalgarno, P. Ohlberg, S. Seidl, M. Kroner, K. Karrai, N. G. Stoltz, P. M. Petroff, and R. J. Warburton, "Optical pumping of a single hole spin in a quantum dot," *Nature*, vol. 451, p. 441, 2008.

[82] Y. Komijani, M. Csontos, T. Ihn, K. Ensslin, D. Reuter, and A. D. Wieck, "Observation of excited states in a p-type GaAs quantum dot," *Europhys. Lett.*, vol. 84, p. 57004, 2008.

[83] W. G. Spitzer and M. B. Panish, "Silicon-doped gallium arsenide grown from gallium solution: Silicon site distribution," *J. Appl. Phys.*, vol. 40, p. 4200, 1969.

[84] M. Grundmann, *The Physics of Semiconductors: An Introduction Including Nanophysics and Applications*. Springer Verlag: Berlin, 2010.

[85] J. Y. Yu, S. W. Chung, and J. R. Heath, "Silicon nanowires - preparation, device fabrication, and transport properties," *J. Phys. Chem. B*, vol. 104, p. 11864, 2000.

[86] M. J. Ashwin, M. R. Fahy, R. C. Newman, J. Wagner, D. A. Robbie, M. J. L. Sangster, I. Silier, E. Bauser, W. Braun, and K. Ploog, "A local vibrational mode investigation of p-type Si-doped GaAs," *J. Appl. Phys.*, vol. 76, p. 7839, 1994.

[87] D. E. Aspnes and A. A. Studna, "Dielectric functions and optical parameters of Si, Ge, GaP, GaAs, GaSb, InP, InAs, and InSb from 1.5 to 6.0 ev," *Phys. Rev. B*, vol. 27, p. 985, 1983.

[88] J. E. Allen, D. E. Perea, E. R. Hemesath, and L. J. Lauhon, "Nonuniform nanowire doping profiles revealed by quantitative scanning photocurrent microscopy," *Adv. Mater.*, vol. 21, p. 3067, 2009.

[89] T. B. Massalki, *Binary Alloy Phase Diagrams*. ASM International: Materials Park, OH, 1990.

[90] S. J. Moss and A. Ledwith, *Chemistry of the Semiconductor Industry*. Chapman and Hall, 1997.

[91] B. H. Ahn, R. R. Shurtz, and C. W. Trussell, "Dependence of growth properties of silicon-doped GaAs epitaxial layers upon orientation," *J. Appl. Phys.*, vol. 42, p. 4512, 1971.

[92] E. S. Tok, J. H. Neave, M. J. Ashwin, B. A. Joyce, and T. S. Jones, "Growth of Si-doped GaAs(110) thin films by molecular beam epitaxy; Si site occupation and the role of arsenic," *J. Appl. Phys.*, vol. 83, p. 4160, 1998.

[93] F. Fischer, D. Schuh, M. Bichler, G. Abstreiter, M. Grayson, and K. Neumaier, "Modulating the growth conditions: Si as an acceptor in (110) GaAs for high mobility p-type heterostructures," *Appl. Phys. Lett.*, vol. 86, p. 192106, 2005.

[94] S. Schuppler, D. L. Adler, L. N. Pfeiffer, K. W. West, E. E. Chaban, and P. H. Citrin, "Can electrical deactivation of highly si-doped gaas be explained by autocompensation?," *Appl. Phys. Lett.*, vol. 63, p. 2357, 1993.

[95] C. Domke, P. Ebert, M. Heinrich, and K. Urban, "Microscopic identification of the compensation mechanisms in Si-doped GaAs," *Phys. Rev. B*, vol. 54, no. 1, p. 10288, 1996.

[96] K. Jain, S. Lai, and M. V. Klein, "Electronic Raman scattering and the metal-insulator transition in doped silicon," *Phys. Rev. B*, vol. 13, p. 5448, 1976.

[97] M. Giehler and E. Jahne, "Effect of damping on the plasmon-phonon coupling in CdS and GaP," *Phys. Status Solidi B*, vol. 73, p. 503, 1976.

[98] D. Hon and W. Faust, "Dielectric parameterization of Raman lineshapes for GaP with a plasma of charge carriers," *Appl. Phys. A: Mater. Sci. Process.*, vol. 1, p. 241, 1973. 10.1007/BF00889771.

[99] S. Nakashima, H. Yugami, A. Fujii, M. Hangyo, and M. Yamanaka, "Raman scattering determination of carrier distribution in GaP diodes," *J. Appl. Phys.*, vol. 64, p. 3067, 1988.

[100] M. Ramsteiner, O. Brandt, and K. H. Ploog, "Overdamped excitations of the free electron gas in GaN layers studied by Raman spectroscopy," *Phys. Rev. B*, vol. 58, p. 1118, 1998.

[101] T. D. Veal, G. R. Bell, and C. F. McConville, "Plasmon damping in molecular beam epitaxial-grown InAs(100)," *J. Vac. Sci. Technol. B*, vol. 20, p. 1766, 2002.

[102] D. A. Anderson, N. Apsley, P. Davies, and P. L. Giles, "Compensation in heavily doped n-type InP and GaAs," *J. Appl. Phys.*, vol. 58, p. 3059, 1985.

[103] E. Veuhoff, H. Bruch, K. Bachem, and P. Balk, "Electron mobility in compensated VPE GaAs films," *Appl. Phys. A: Mater. Sci. Process.*, vol. 23, p. 37, 1980. 10.1007/BF00899568.

[104] S. Dhara, H. S. Solanki, V. Singh, A. Narayanan, P. Chaudhari, M. Gokhale, A. Bhattacharya, and M. M. Deshmukh, "Magnetotransport properties of individual InAs nanowires," *Phys. Rev. B*, vol. 79, p. 121311, 2009.

[105] M. I. McMahon and R. J. Nelmes, "Observation of a wurtzite form of gallium arsenide," *Phys. Rev. Lett.*, vol. 95, p. 215505, 2005.

[106] P. Caroff, K. A. Dick, J. Johansson, M. E. Messing, K. Deppert, and S. L., "Controlled polytypic and twin-plane superlattices in iii-v nanowires," *Nat. Nano.*, vol. 4, p. 50, 2009.

[107] R. E. Algra, M. A. Verheijen, M. T. Borgstrom, L.-F. Feiner, G. Immink, W. J. P. van Enckevort, E. Vlieg, and E. P. A. M. Bakkers, "Twinning superlattices in indium phosphide nanowires," *Nature*, vol. 456, p. 369, 2008.

[108] J. Johansson, K. A. Dick, P. Caroff, M. E. Messing, J. Bolinsson, K. Deppert, and L. Samuelson, "Diameter dependence of the wurtzite-zinc blende transition in InAs nanowires," *J. Phys. Chem. C*, vol. 114, p. 3837, 2010.

[109] T. Akiyama, K. Sano, K. Nakamura, and T. Ito, "An empirical potential approach to wurtzite-zinc-blende polytypism in group iii–v semiconductor nanowires," *Jpn. J. Appl. Phys.*, vol. 45, p. L275, 2006.

[110] V. G. Dubrovskii and N. V. Sibirev, "Growth thermodynamics of nanowires and its application to polytypism of zinc blende iii-v nanowires," *Phys. Rev. B*, vol. 77, p. 035414, 2008.

[111] F. Glas, J. C. Harmand, and G. Patriarche, "Why does wurtzite form in nanowires of iii-v zinc blende semiconductors?," *Phys. Rev. Lett.*, vol. 99, p. 146101, 2007.

[112] J. Johansson, L. S. Karlsson, K. A. Dick, J. Bolinsson, B. A. Wacaser, K. Deppert, and L. Samuelson, "Effects of supersaturation on the crystal structure of gold seeded iii-v nanowires," *Cryst. Growth Des.*, vol. 9, p. 766, 2009.

[113] P. Krogstrup, S. Curiotto, E. Johnson, M. Aagesen, J. Nygård, and D. Chatain, "Impact of the liquid phase shape on the structure of iii-v nanowires," *Phys. Rev. Lett.*, vol. 106, p. 125505, 2011.

[114] M. Mattila, T. Hakkarainen, M. Mulot, and H. Lipsanen, "Crystal-structure-dependent photoluminescence from InP nanowires," *Nanotechnology*, vol. 17, p. 1580, 2006.

[115] A. Mishra, L. V. Titova, T. B. Hoang, H. E. Jackson, L. M. Smith, J. M. Yarrison-Rice, Y. Kim, H. J. Joyce, Q. Gao, H. H. Tan, and C. Jagadish, "Polarization and temperature dependence of photoluminescence from zincblende and wurtzite InP nanowires," *Appl. Phys. Lett.*, vol. 91, p. 263104, 2007.

[116] J. L. Birman, "Polarization of fluorescence in CdS and ZnS single crystals," *Phys. Rev. Lett.*, vol. 2, p. 157, 1959.

[117] K. A. Dick, C. Thelander, L. Samuelson, and P. Caroff, "Crystal phase engineering in single InAs nanowires," *Nano Lett.*, vol. 10, p. 3494, 2010.

[118] A. De and C. E. Pryor, "Predicted band structures of iii-v semiconductors in the wurtzite phase," *Phys. Rev. B*, vol. 81, p. 155210, 2010.

[119] M. Murayama and T. Nakayama, "Chemical trend of band offsets at wurtzite/zinc-blende heterocrystalline semiconductor interfaces," *Phys. Rev. B*, vol. 49, p. 4710, 1994.

[120] M. Heiss, S. Conesa-Boj, J. Ren, H. H. Tseng, A. Gali, A. Rudolph, E. Uccelli, F. Peiró, J. R. Morante, D. Schuh, E. Reiger, E. Kaxiras, J. Arbiol, and A. Fontcuberta i Morral, "Direct correlation of crystal structure and optical properties in wurtzite/zinc-blende GaAs nanowire heterostructures," *Phys. Rev. B*, vol. 83, p. 045303, 2011.

[121] S. L. Chuang and C. S. Chang, "k·p method for strained wurtzite semiconductors," *Phys. Rev. B*, vol. 54, p. 2491, 1996.

[122] I. Vurgaftman, J. R. Meyer, and L. R. Ram-Mohan, "Band parameters for iii-v compound semiconductors and their alloys," *J. Appl. Phys.*, vol. 89, p. 5815, 2001.

[123] J. L. Birman, "Simplified LCAO method for zincblende, wurtzite, and mixed crystal structures," *Phys. Rev.*, vol. 115, p. 1493, 1959.

[124] C. Y. Yeh, S. H. Wei, and A. Zunger, "Relationships between the band gaps of the zinc-blende and wurtzite modifications of semiconductors," *Phys. Rev. B*, vol. 50, p. 2715, 1994.

[125] Z. Zanolli, F. Fuchs, J. Furthmüller, U. von Barth, and F. Bechstedt, "Model GW band structure of InAs and GaAs in the wurtzite phase," *Phys. Rev. B*, vol. 75, p. 245121, 2007.

[126] R. C. C. Leite, J. F. Scott, and T. C. Damen, "Multiple-phonon resonant Raman scattering in Cds," *Phys. Rev. Lett.*, vol. 22, p. 780, 1969.

[127] A. García-Cristóbal, A. Cantarero, C. Trallero-Giner, and M. Cardona, "Excitonic model for second-order resonant Raman scattering," *Phys. Rev. B*, vol. 49, p. 13430, 1994.

[128] M. H. Sun, E. S. P. Leong, A. H. Chin, C. Z. Ning, G. E. Cirlin, Y. B. Samsonenko, V. G. Dubrovskii, L. Chuang, and C. Chang-Hasnain, "Photoluminescence properties of InAs nanowires grown on GaAs and Si substrates," *Nanotechnology*, vol. 21, p. 335705, 2010.

[129] T. B. Hoang, A. F. Moses, H. L. Zhou, D. L. Dheeraj, B. O. Fimland, and H. Weman, "Observation of free exciton photoluminescence emission from single wurtzite GaAs nanowires," *Appl. Phys. Lett.*, vol. 94, p. 133105, 2009.

[130] F. Martelli, M. Piccin, G. Bais, F. Jabeen, S. Ambrosini, S. Rubini, and A. Franciosi, "Photoluminescence of Mn-catalyzed GaAs nanowires grown by molecular beam epitaxy," *Nanotechnology*, vol. 18, p. 125603, 2007.

[131] M. Moewe, L. C. Chuang, S. Crankshaw, C. Chase, and C. Chang-Hasnain, "Atomically sharp catalyst-free wurtzite GaAs/AlGaAs nanoneedles grown on silicon," *Appl. Phys. Lett.*, vol. 93, p. 023116, 2008.

[132] L. C. Chuang, M. Moewe, K. W. Ng, T. T. D. Tran, S. Crankshaw, R. Chen, W. S. Ko, and C. Chang-Hasnain, "GaAs nanoneedles grown on sapphire," *Appl. Phys. Lett.*, vol. 98, p. 123101, 2011.

[133] S. Perera, K. Pemasiri, M. A. Fickenscher, H. E. Jackson, L. M. Smith, J. Yarrison-Rice, S. Paiman, Q. Gao, H. H. Tan, and C. Jagadish, "Probing valence band structure in wurtzite InP nanowires using excitation spectroscopy," *Appl. Phys. Lett.*, vol. 97, p. 023106, 2010.

[134] E. G. Gadret, G. O. Dias, L. C. O. Dacal, M. M. de Lima, C. V. R. S. Ruffo, F. Iikawa, M. J. S. P. Brasil, T. Chiaramonte, M. A. Cotta, L. H. G. Tizei, D. Ugarte, and A. Cantarero, "Valence-band splitting energies in wurtzite InP nanowires: Photoluminescence spectroscopy and ab initio calculations," *Phys. Rev. B*, vol. 82, p. 125327, 2010.

[135] J. Wallentin, K. Mergenthaler, M. Ek, L. R. Wallenberg, L. Samuelson, K. Deppert, M. E. Pistol, and M. T. Borgström, "Probing the wurtzite conduction band structure using state filling in highly doped InP nanowires," *Nano Lett.*, vol. 11, p. 2286, 2011.

[136] W. Kauschke and M. Cardona, "Resonant Raman scattering and interference effects of lo phonons at the $E_0 + \Delta_0$ gap of InP," *Phys. Rev. B*, vol. 33, p. 5473, 1986.

[137] W. Kauschke and M. Cardona, "Resonant Raman scattering by LO phonons near the $E_0+\Delta_0$ gap of GaSb," *Phys. Rev. B*, vol. 35, p. 9619, 1987.

[138] A. Rudolph, M. Soda, M. Kiessling, T. Wojtowicz, D. Schuh, W. Wegscheider, J. Zweck, C. Back, and E. Reiger, "Ferromagnetic Gaas/GaMnAs core-shell nanowires grown by molecular beam epitaxy," *Nano Lett.*, vol. 9, p. 3860, 2009.

[139] D. Spirkoska, C. Colombo, M. Heiss, G. Abstreiter, and A. Fontcuberta i Morral, "The use of molecular beam epitaxy for the synthesis of high purity iii-v nanowires," *J. Phys.: Condens. Matter.*, vol. 20, p. 454225, 2008.

[140] M. A. Mojumder, "Dipole selection rules for wurtzite structure and the reflection spectra of hexagonal CdS," *Solid State Commun.*, vol. 43, p. 13, 1982.

[141] P. Tronc, Y. Kitaev, G. Wang, M. Limonov, A. Panfilov, and G. Neu, "Optical selection rules for hexagonal GaN," *physica status solidi (b)Phys. Status Solidi B*, vol. 216, p. 599, 1999.

[142] D. G. Thomas and J. J. Hopfield, "Optical properties of bound exciton complexes in cadmium sulfide," *Phys. Rev.*, vol. 128, p. 2135, 1962.

[143] M. Cardona and G. Harbeke, "Optical properties and band structure of wurtzite-type crystals and rutile," *Phys. Rev.*, vol. 137, p. A1467, 1965.

[144] N. Ohno, M. Yoshida, K. Nakamura, and Y. Nakai, "Multiple LO scattering in indium iodide," *Solid State Commun.*, vol. 53, p. 569, 1985.

[145] H. Mitsutake, M. Yoshida, K. Nakamura, and Y. Nakai, "Resonant light scattering in InBr: Intensity alternation of multiple LO phonon scattering," *J. Phys. Soc. Jpn.*, vol. 55, p. 1070, 1986.

[146] C. Trallero-Giner and R. Riera, "Multiple LO-phonon Raman scattering and hot excitons," *Phys. Status Solidi B*, vol. 152, p. 357, 1989.

[147] M. Brewster, O. Schimek, S. Reich, and S. Gradečak, "Exciton-phonon coupling in individual GaAs nanowires studied using resonant Raman spectroscopy," *Phys. Rev. B*, vol. 80, p. 201314, 2009.

[148] Y. P. Varshni, "Temperature dependence of the energy gap in semiconductors," *Physica*, vol. 34, p. 149, 1967.

Bibliography

[149] P. Lautenschlager, M. Garriga, S. Logothetidis, and M. Cardona, "Interband critical points of GaAs and their temperature dependence," *Phys. Rev. B*, vol. 35, p. 9174, 1987.

[150] T. Cheiwchanchamnangij and W. R. L. Lambrecht, "Band structure parameters of wurtzite and zinc-blende gaas under strain in the gw approximation," *Phys. Rev. B*, vol. 84, p. 035203, 2011.

[151] K. W. J. Barnham and G. Duggan, "A new approach to high-efficiency multi-band-gap solar cells," *J. Appl. Phys.*, vol. 67, p. 3490, 1990.

[152] F. Glas, "Critical dimensions for the plastic relaxation of strained axial heterostructures in free-standing nanowires," *Phys. Rev. B*, vol. 74, p. 121302, 2006.

[153] G. Ferrari, G. Goldoni, A. Bertoni, G. Cuoghi, and E. Molinari, "Magnetic states in prismatic core multishell nanowires," *Nano Lett.*, vol. 9, p. 1631, 2009.

[154] H. Kroemer, "Heterostructure bipolar transistors and integrated circuits," *P. IEEE*, vol. 70, p. 13, 1982.

[155] N. Ledentsov, V. Ustinov, V. Shchukin, P. Kop'ev, Z. Alferov, and D. Bimberg, "Quantum dot heterostructures: Fabrication, properties, lasers (review)," *Semiconductors*, vol. 32, p. 343, 1998. 10.1134/1.1187396.

[156] G. Fasol, N. Mestres, A. Fischer, and K. Ploog, "Coupled plasmons and single particle excitations in the two-dimensional electron gas," *Phys. Scr.*, vol. 1987, p. 109, 1987.

[157] O. Demichel, F. Oehler, P. Noe, C. V., N. Pauc, P. Gentile, T. Baron, D. Peyrade, and N. Magnea, "Photoluminescence of confined electron-hole plasma in core-shell silicon/silicon oxide nanowires," *Appl. Phys. Lett.*, vol. 93, p. 213104, 2008.

[158] G. Ferrari, A. Bertoni, G. Goldoni, and E. Molinari, "Cylindrical two-dimensional electron gas in a transverse magnetic field," *Phys. Rev. B*, vol. 78, p. 115326, 2008.

[159] L. J. Lauhon, M. S. Gudiksen, D. Wang, and C. M. Lieber, "Epitaxial core-shell and core-multishell nanowire heterostructures," *Nature*, vol. 420, p. 57, 2002.

[160] Z. V. Popović, M. Cardona, E. Richter, D. Strauch, L. Tapfer, and K. Ploog, "Phonon properties of GaAs/AlAs superlattice grown along the [110] direction," *Phys. Rev. B*, vol. 40, p. 3040, 1989.

[161] A. J. Shields, M. P. Chamberlain, M. Cardona, and K. Eberl, "Raman scattering due to interface optical phonons in GaAs/AlAs multiple quantum wells," *Phys. Rev. B*, vol. 51, p. 17728, 1995.

[162] A. K. Sood, J. Menéndez, M. Cardona, and K. Ploog, "Resonance raman scattering by confined LO and TO phonons in GaAs-AlAs superlattices," *Phys. Rev. Lett.*, vol. 54, p. 2111, 1985.

[163] G. Bastard, "Superlattice band structure in the envelope-function approximation," *Phys. Rev. B*, vol. 24, p. 5693, 1981.

[164] D. Kirillov, C. Webb, and J. N. Eckstein, "Raman scattering study of heavily Si-doped GaAs-Ga$_{1-x}$Al$_x$As superlattices grown by molecular beam epitaxy," *J. Cryst. Growth*, vol. 81, p. 91, 1987.

[165] Y. Pusep, A. Milekhin, and A. Poropov, "FTIR-spectroscopy of (GaAs)$_n$/(AlAs)$_m$ superlattices," *Superlattices Microstruct.*, vol. 13, p. 115, 1993.

[166] A. Pinczuk, G. Abstreiter, R. Trommer, and M. Cardona, "Resonance enhancement of Raman scattering by electron-gas excitations of n-GaAs," *Solid State Commun.*, vol. 30, p. 429, 1979.

[167] B. Lou, "Plasmon-phonon coupling in GaAs-AlAs superlattices," *Solid State Commun.*, vol. 84, p. 685, 1992.

[168] C. L. Collins and P. Y. Yu, "Light scattering from nonequilibrium electron-hole plasma excited by picosecond laser pulses in GaAs," *Solid State Commun.*, vol. 51, p. 123, 1984.

[169] U. Strauss, W. W. Rühle, and K. Köhler, "Auger recombination in intrinsic GaAs," *J. Appl. Phys.*, vol. 62, p. 55, 1993.

List of Publications

B. Ketterer, M. Heiss, E. Uccelli, J. Arbiol, and A. Fontcuberta i Morral, "Untangling the Electronic Band Structure of Wurtzite GaAs Nanowires by Resonant Raman Spectroscopy", *ACS Nano*, vol. 5, p. 7585, 2011

B. Ketterer, M.Heiss, M. J. Livrozet, A. Rudolph, E. Reiger, and A. Fontcuberta i Morral, "Determination of the Bandgap and Split-Off Band of Wurtzite GaAs", *Phys. Rev. B*, vol. 83, p. 125307, 2011

B. Ketterer, J. Arbiol, and A. Fontcuberta i Morral, "Phonon Confinement and Plasmon-Phonon Interaction in Nanowire Based Quantum Wells", *Phys. Rev. B*, vol. 83, p. 245327, 2011

M. Heiß, B. Ketterer, E. Uccelli, J. R. Morante, J. Arbiol, and A. Fontcuberta i Morral, "Group-III Assisted Catalyst-Free Growth of InGaAs Nanowires and the Formation of Quantum Dots", *Nanotechnology*, vol. 22, p. 195601, 2011

B. Ketterer, E. Mikheev, E. Uccelli, and A. Fontcuberta i Morral, "Compensation Mechanism in Silicon-Doped Gallium Arsenide Nanowires", *Appl. Phys. Lett.*, vol. 97, p.223103, 2010

J. Dufouleur, C. Colombo, T. Garma, B. Ketterer, E. Uccelli, M. Nicotra, and A. Fontcuberta i Morral, "P-Doping Mechanisms in Catalyst-Free Gallium Arsenide Nanowires", *Nano Lett.*, vol. 10, p. 1734, 2010

B. Ketterer, E. Uccelli, and A. Fontcuberta i Morral, "Mobility and Carrier Density in P-type GaAs Nanowires Measured by Transmission Raman Spectroscopy", *submitted*

Acknowledgements

I would like to take the opportunity to thank all the people who contributed in different ways to this work:

I am deeply grateful to my thesis director, **Prof. Anna Fontcuberta i Morral**, for all her support, encouragement, and advice during all these years. Thank you for your efforts in reading and correcting my articles, reports, and my thesis manuscript.

I am also grateful to **Dr. Heike Riel**, **Prof. Andras Kis**, **Prof. Christian Schüller**, and **Prof. Francesco Stellacci** for accepting to be the members of my thesis jury.

My acknowledgment goes to **Prof. Jordi Arbiol** of the Institució Catalana de Recerca i Estudis Avançats (ICREA) for his transmission electron microscopy investigations.

I want to thank **Andreas Rudolph**, **Dr. Dieter Schuh** and **Dr. Elisabeth Reiger** from the University of Regensburg for the growth of Au-catalyzed GaAs nanowire samples.

During my PhD I have had a chance to visit the group of **Prof. Christian Schüller** at the University of Regensburg. I want to thank him for the fruitful discussions we had there.

I would like to kindly thank **Prof. Gerhard Abstreiter** from the Walter Schottky Institut for making the MBE available in Munich for the synthesis of the nanowire samples I used during the first year of my PhD work. I also want to acknowledge **Max Bichler** for experimental support there.

Acknowledgements

I would like to thank all former and present LMSC colleagues and friends. Thank you all for the stimulating discussions and the nice atmosphere. Many thanks to the 'early nucleus' of the LMSC group **Anna**, **Carlo**, and **Santi** for the great time we spent together. Special thanks to **Martin** for sharing all his great ideas with me. Thanks a lot to **Emanuele** for all his effort in preparing samples for me. Also thanks to all the 'newcomers' **Daniel**, **Eleonora**, **Olivier**, **Pierre**, **Shanna**, and **Yannik** and all the visiting students for the fun we had in and outside the lab. Very special thanks belong to our secretary **Yvonne** as the heart and soul of the LMSC group.

Many thanks to **my parents** for helping and supporting me in any possible way.

Curriculum Vitae

Bernt Ketterer

Email: BerntKetterer@web.de

PERSONAL INFORMATION

- Date of birth: 19th January 1981
- Place of birth: Villingen-Schwenningen, Germany
- Nationality: German

EDUCATION

2009-today: **PhD** in Materials Science and Technology   **EPF Lausanne (EPFL)**

2004-2008:   **Diploma in Physics**   **University of Karlsruhe**

2000-2008:   **Diploma in Industrial Engineering & Management**   **University of Karlsruhe**

COMPETENCES

Research Experience and Technical Skills:
Raman spectroscopy, Photoluminescence spectroscopy (PL), Transmission electron microscopy (TEM/HRTEM), Scanning electron microscopy (SEM), Atomic force microscopy (AFM), Magnetron sputter deposition of thin films, X-ray diffraction (XRD), X-ray reflectometry (XRR)

Informatics:
Mathematica, Origin, LabVIEW, Java

Languages
- English – fluent both written and spoken
- French – fluent spoken, intermediate written
- German – mother tongue

PROJECTS AND PRACTICAL EXPERIENCE

PhD thesis

Raman spectroscopy investigation of the doping and the fundamental properties of GaAs nanowires. Installation of an optical laboratory for low-temperature Raman- and photoluminescence spectroscopy with responsibility for the acquisition of the equipment. Supervisor for semester projects for undergraduate and graduate students.

Diploma thesis (Physics)

Magnetron-sputtering of functional thin films for micro-batteries. Analysis and optimization of morphology, the interfaces, and the properties of the coatings by varying the working gas pressure and the degree of ion bombardment during deposition.

Diploma thesis (Industrial Engineering)

Feasibility study presenting the state of the art of lithium-ion batteries and their potential in the electromobility sector. Detailed cost analysis of the battery components and cost forecasts for the lithium-ion technology.

Internships

- Defining guidelines for the production cost analysis, *Böhringer Ingelheim Pharma KG*, Sales management and controlling department (August–October 2002)
- Validation of operational procedures, *Marquardt GmbH*, Measurement tools department (August–September 2001)